Multiphysics Transport in Heterogeneous Media: from Pore-Scale Modeling to Deep Learning

Haiyi Wu

Dissertation submitted to the faculty of the Virginia Polytechnic Institute and State University in partial fulfillment of the requirements for the degree of

Doctor of Philosophy

In

Mechanical Engineering

Rui Qiao, Chair

Jonathan B Boreyko

Cheng Chen

Reza Mirzaeifar

Danesh K Tafti

May 5th, 2020

Blacksburg, Virginia

Keywords: shale gas recovery, drying of porous materials, deep learning, pore-network models, molecular dynamics simulations

Multiphysics Transport in Heterogeneous Media: from Pore-Scale Modeling to Deep learning

Haiyi Wu

ABSTRACT

Transport phenomena in heterogeneous media play a crucial role in numerous engineering applications such as hydrocarbon recovery from shales and material processing. Understanding and predicting these phenomena is critical for the success of these applications. In this dissertation, nanoscale transport phenomena in porous media are studied through physics-based simulations, and the effective solution of forward and inverse transport phenomena problems in heterogeneous media is tackled using data-driven, deep learning approaches.

For nanoscale transport in porous media, the storage and recovery of gas from ultra-tight shale formations are investigated at the single-pore scale using molecular dynamics simulations. In the single-component gas recovery, a super-diffusive scaling law was found for the gas production due to the strong gas adsorption-desorption effects. For binary gas (methane/ethane) mixtures, surface adsorption contributes greatly to the storage of both gas in nanopores, with ethane enriched compared to methane. Ethane is produced from nanopores as effectively as the lighter methane despite its slower self-diffusion than the methane, and this phenomenon is traced to the strong couplings between the transport of the two species in the nanopore. The dying of solvent-loaded nanoporous filtration cakes by a purge gas flowing through them is next studied. The novelty and challenge of this problem lie in the fact that the drainage and evaporation can occur simultaneously. Using pore-network modeling, three distinct drying stages are identified. While drainage contributes less and less as drying proceeds through the first two stages, it can still contribute considerably to the net drying rate because of the strong coupling between the drainage and evaporation processes in the filtration cake.

For the solution of transport phenomena problems using deep learning, first, convolutional neural networks with various architectures are trained to predict the effective diffusivity of two-dimensional (2D) porous media with complex and realistic structures from their images. Next, the

inverse problem of reconstructing the structure of 2D heterogeneous composites featuring high-conductivity, circular fillers from the composites' temperature field is studied. This problem is challenging because of the high dimensionality of the temperature and conductivity fields. A deep-learning model based on convolutional neural networks with a U-shape architecture and the encoding-decoding processes is developed. The trained model can predict the distribution of fillers with good accuracy even when coarse-grained temperature data (less than 1% of the full data) are used as an input. Incorporating the temperature measurements in regions where the deep learning model has low prediction confidence can improve the model's prediction accuracy.

Multiphysics Transport in Heterogeneous Media: from Pore-Scale Modeling to Deep Learning

Haiyi Wu

GENERAL AUDIENCE ABSTRACT

Multiphysics transport phenomena inside structures with non-uniform pores or properties are common in engineering applications, e.g., gas recovery from shale reservoirs and drying of porous materials. Research on these transport phenomena can help improve related applications. In this dissertation, multiphysics transport in several types of structures is studied using physics-based simulations and data-driven deep learning models.

In physics-based simulations, the multicomponent and multiphase transport phenomena in porous media are solved at the pore scale. The recovery of methane and methane-ethane mixtures from nanopores is studied using simulations to track motions and interactions of methane and ethane molecules inside the nanopores. The strong gas-pore wall interactions lead to significant adsorption of gas near the pore wall and contribute greatly to the gas storage in these pores. Because of strong gas adsorption and couplings between the transport of different gas species, several interesting and practically important observations have been found during the gas recovery process. For example, lighter methane and heavier ethane are recovered at similar rates. Pore-scale modeling are applied to study the drying of nanoporous filtration cakes, during which drainage and evaporation can occur concurrently. The drying is found to proceed in three distinct stages and the drainage-evaporation coupling greatly affects the drying rate.

In deep learning modeling, convolutional neural networks are trained to predict the diffusivity of two-dimensional porous media by taking the image of their structures as input. The model can predict the diffusivity of the porous media accurately with computational cost orders of magnitude lower than physics-based simulations. A deep learning model is also developed to reconstruct the structure of fillers inside a two-dimensional matrix from its temperature field. The trained model can predict the structure of fillers accurately using full-scale and coarse-grained temperature input data. The predictions of the deep learning model can be improved by adding additional true temperature data in regions where the model has low prediction confidence.

Dedication

For my mother, Mrs. Meiying Lin, my father, Mr. Fulin Wu, and all my sisters and brothers.

Acknowledgments

This dissertation cannot be made without the support and help from many people. First of all, I would express my sincere gratitude and respect to my advisor Professor Rui Qiao for his constant support and encouragement. During my Ph.D. study at Virginia Tech, he has provided a lot of guidance and inspiration for my research work and life. Apart from all the interesting projects we work together, he always taught me how to think about a problem in a physical way, how to capture the main physics behind a complex problem, and how to approach a problem wisely. In the past five years, I have received utmost support from my advisor: he is always very flexible about my research directions and encourages me to work on some frontier research based on my interests; hence I had the chance to explore many interesting research topics including applying machine learning and deep learning into my research domain. Thank you very much, Dr. Qiao, and I hope that you will be a life-long mentor and friend of mine.

I would also like to thank all my advisory committee members: Dr. Danesh Tafti, Dr. Cheng Chen, Dr. Jonathan Boreyko, and Dr. Reza Mirzaeifar, for their valuable time and suggestions on my research and course work.

I am also very grateful to all the research collaborators, especially Dr. Qinjun Kang from Los Alamos National Laboratory and Dr. Wenzhen Fang at Nanyang Technological University for providing the valuable datasets to train the deep learning model for predicting the effective transport properties of porous media. I would also like to thank Professor Guoqing Hu from Zhe Jiang University and Professor Rui Wu from Shanghai Jiao Tong University for their help in my research. The drying work would not exist in this dissertation without the collaboration between Professor Roe-Hoan Yoon at Virginia Tech.

I appreciate the time and training in the TPL group and would like to extend my thanks to all the group members, Dr. Ying Liu, Dr. Yadong He, Dr. Fengchang Yang, Dr. Zhou Yu, Dr. Fei Zhang, Dr. Chao Fang, Mr. David Moh, Mr. Hongwei Zhang, Mr. Seok Gyun Ham, and Mr. Michael Huylo. In particular, I would like to thank Dr. Yadong He for his numerous help when I first started my doctoral research.

Table of Contents

Chapter 1. Introduction

1.1 Multiphysics Transport in Heterogeneous Media

Heterogeneous media are ubiquitous in engineering systems and understanding the transport phenomena inside them is essential for many engineering applications.[1-4] For example, shale gas is typically trapped in ultra-tight porous formations with nanoscale pores. The effective extraction of shale gas thus requires a fundamental understanding of the transport phenomena in the shale formations (Fig. 1-1 a).[4-8] Porous media are common in industrial and groundwater systems (Fig. 1-1 b); drying of these heterogeneous media is often an important operation but it is usually energy-intensive.[9-12] Understanding the transport phenomena involved in the drying (dewatering) process can help to improve drying technologies and enhance drying efficiency.[11-12] Furthermore, porous (heterogeneous) materials are often involved in manufacturing processes.[13] For example, porous constructs must be dipped into resins during the fabrication of ceramic matrix composites. The infusion of resins into the porous structure greatly affects the quality of the finished product. Understanding the transport of resins into porous structures is therefore essential for the rational optimization of the manufacturing process.

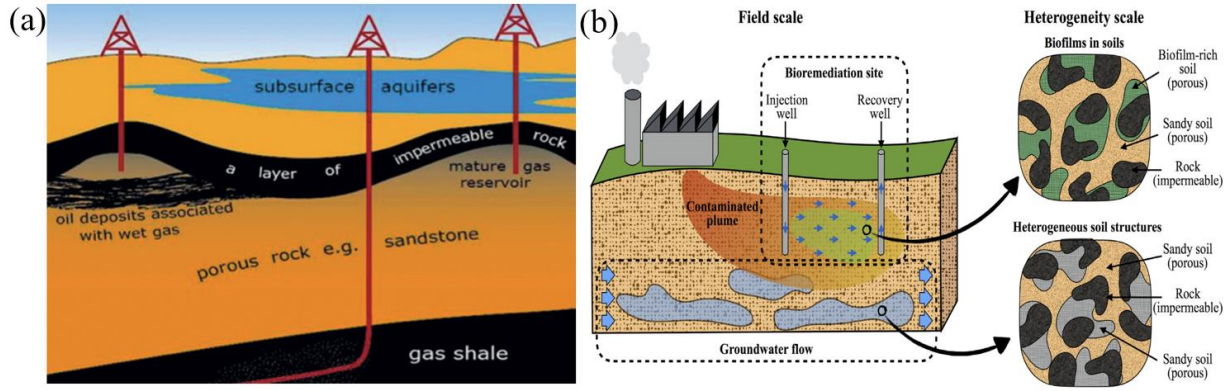

Figure 1-1. Multiphysics transport in heterogeneous media. (**a**) Recovery of shale gas from conventional and unconventional gas reservoirs. The reservoirs are porous media feature a wide range of porosity, pore size, and chemical compositions. (**b**) Removal of pollutants from underground by bioremediation. The soil is essentially a heterogeneous porous medium. Panel (a) is reproduced from Ref. 14 with the permission of EPJ Web of Conferences under the Creative Commons Attribution License. Panel (b) is reproduced from Ref. 15 with the permission of Elsevier.

Due to their importance in engineering applications, transport phenomena in heterogeneous media have been studied extensively. Many mathematical models have been developed including the Navier-Stokes equations for solving single and multiphase fluid transport[16-18] and the Dusty Gas model, which has been widely used in describing the motion of fluid mixtures through porous media, is adopted for solving multicomponent gas transport.[19-21] Many numerical methods have been developed or extended to study these phenomena. For example, molecular dynamics (MD) simulations have been adapted to study the transport processes in nanoporous media.[22-23] Continuum pore-scale modeling based on Lattice Boltzmann methods and pore-network models have also been applied to quantify the flow of fluids in heterogeneous porous media.[16-17]

Despite the significant progress in research on transport phenomena in heterogeneous media, there is a continuing challenge to understand the new transport physics that emerges in unique but practically important systems. For example, as the critical dimension of pores in a porous medium shrinks toward the mean-free path or even the size of fluid molecules, the classical Darcian description of the fluid flow in porous media can breakdown and new models must be developed.[7-8, 24] When the pore size is comparable to the mean-free path length but greatly larger than the molecule diameter, accurate gas transport models are now available, but well-established models for flows in more confined pores are still lacking.

In addition to newly emerged challenges, many long-standing problems remain to be solved. For example, predicting the effective transport properties of porous media from their structure is important in many engineering applications. In principle, these effective transport properties can be obtained by solving the related governing equations in the porous media (e.g., the effective gas diffusivity can be computed by solving the Laplace equation). However, solving these equations in porous media with diverse and realistic topology typically involves significant computational cost, which renders their application difficult, if possible at all. For example, if the topology and structure of porous media evolve as a function of time, then their effective transport properties may need to be computed millions of times, thereby incurring a prohibitive computational cost. Besides, for many engineering optimization, diagnosis, and design applications, inverse problems,

i.e., inferring the structure of the heterogeneous media from the transport phenomena within them, must be solved. Solving these problems has been a long-standing challenge: conventional methods usually require significant computational cost because of the large number of parameters and uncertainties involved. This challenge is especially acute for high-dimensional inverse problems, in which the problems are often ill-posed.

Overall, transport phenomena in heterogeneous media play a critical role in many industrial applications. Despite constant progress in understanding these phenomena, new challenges for the accurate prediction of these transport phenomena continue to emerge at the frontier of engineering practice and the long-standing challenge of accurately and efficiently solving transport phenomena in heterogeneous media (even with well-understood physics) remains. This dissertation seeks to address these challenges in several interesting applications.

1.2 New Physics of Gas and Liquid Transport in Porous Media

In this dissertation, the new physics of gas and liquid transport in porous media arising from nanoscale confinement in two important applications are explored, i.e., the recovery of natural gas from shale formations and the drying of nanoporous filtration cakes by purging gas.

1.2.1 Gas recovery from shale formations

A majority of industrial processes must be powered by energy resources. As a sequence of the rapid industrial development in recent decades, especially in developing countries, the global energy demand continues to increase. According to the report by BP's Energy Outlook, the world's primary energy consumption will increase by 34% between 2014 and 2035.[25] Much of the world's energy demand will continue to be provided by fossil fuels in the near future because of the many limitations of renewable energy sources. Natural gas is one of the most important fossil fuels. In the past decade, shale gas has provided the largest resource of growth in natural gas and it can potentially be a new global energy source in the coming decades.[26]

Shale and shale gas. Shale gas is the natural gas stored in shale formations, which are fine-grained sedimentary rocks and are primarily composed of fine particles made of clay minerals and

quartz.[27] In typical shale samples, both organic matter and inorganic matter are present, and shale gas is trapped in the pores in both of them (see image and schematics in Fig. 1-2).[28] There are many types of shales, e.g., black shales, siliceous shales, and carbonaceous shales. There are large amounts of organic matter in black shale, and the total organic carbon (TOC) is usually 3%-15%.[29]

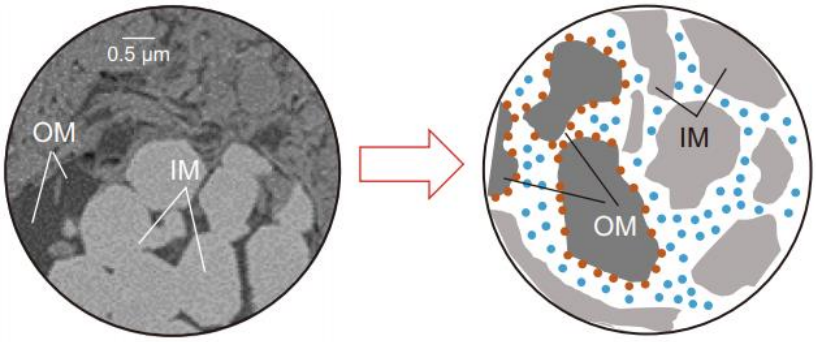

Figure 1-2. An SEM image (left) and a schematic diagram (right) of a shale sample. Nanopores are observed in both organic and inorganic matters. OM and IM mean organic matter and inorganic matter, respectively. This figure is reproduced from Ref. 28 with the permission of Springer Nature under the Creative Commons CC BY license.

The composition of shale gas varies among different shale formations. Methane is always the most abundant component, but hydrocarbons with higher molecular mass (i.e., ethane, propane, *etc*.) are often presented as well. The composition of typical shale gas in the Marcellus formation is illustrated in Fig. 1-3. Ethane is usually the second primary component of shale gas and can account for up to 16 vol% of a shale gas.[30-31] Propane and butane can take up to ~6% vol% of the recovered shale gas. The extraction of these hydrocarbons with higher molecular mass than the methane is of great interest because they are more valuable than methane.

A distinguishing aspect of shales is that they mainly feature nanopores. Shale gas is mainly stored in these nanopores. As illustrated in Fig. 1-4, their pores can have size from subnanometer to several micrometers, but a significant portion of their pores have diameters less than 2 nm.[32] Apart from a substantial amount of pores with nanometer sizes, the connection between the pores is often poor in ultra-tight shales.[33] Therefore, the permeability of shales is extremely low, often on the order of nano-Darcy or even smaller (A Darcy $= 9.87 \times 10^{-13}$ m^2 is a unit of permeability, which is not SI units but has been widely used in geology and petroleum engineering). Because of

this, the conventional techniques for recovering natural gas are ineffective for shale gas extraction. Therefore, although shale gas is abundant, they have not been utilized widely until the early 2000s.

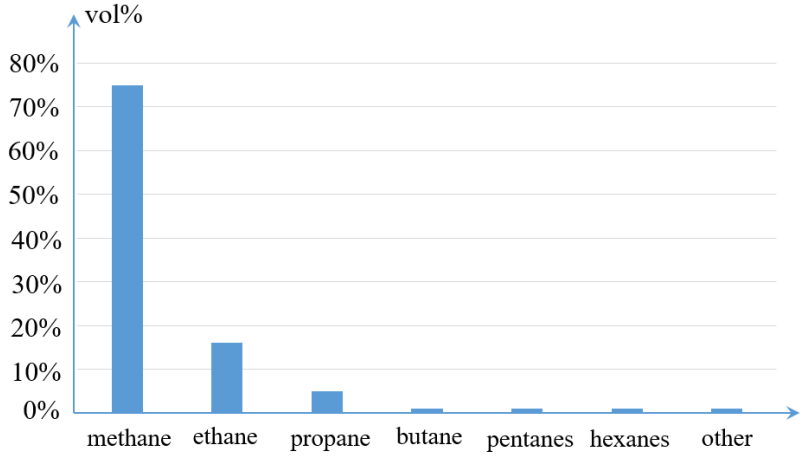

Figure 1-3. The volume fractions of different hydrocarbons in a representative Marcellus shale. The figure is made using data in Ref. 31.

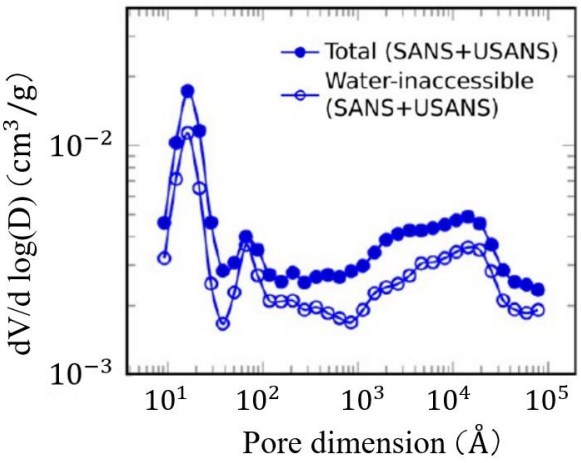

Figure 1-4. Pore size distribution of a representative shale sample. The data were generated by combining ultrasmall-angle neutron scattering (USANS) and small-angle neutron scattering (SANS) techniques. This figure is reproduced from Ref. 32 with the permission of American Chemical Society.

Recently, many advanced technologies have been developed to enable the effective extraction of shale gas. Horizontal drilling and hydraulic fracturing are two of the major techniques that have been widely used to create conductive pathways to enhance the permeability of wellbores and enable the economic extractions of shale gas. In shale gas engineering, vertical wells are typically applied to extract gas from the shale matrix. At the end of a vertical well, a horizontal wellbore is drilled at a similar depth as the shales, which is around 2000 m.[34] Hydraulic fractures are then

generated along the horizontal wellbores, and many fractures will be generated in the shale formation. With these fractures, numerous highly conductive pathways are formed for gas transport, which help to enhance shale gas production. Although the fractures have a much longer length than the nanopores in shales, because their size is much larger than that of the nanopores in the shales, they pose relatively little resistance to shale gas recovery. Instead, with the fracture network generated by horizontal drilling and hydraulic fracturing, the gas transport within the nanopores in the shales usually becomes the limiting factor for gas production.[3, 35] For this reason, understanding the gas storage and transport in nanopores is needed to predict the gas recovery accurately.

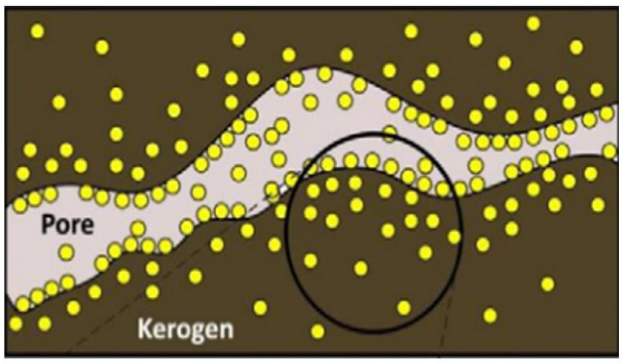

Figure 1-5. A schematic of the distribution of gas molecules in shale's kerogen materials. The filled yellow circles and the gray space denote the gas molecules and pore space, respectively. This figure is reproduced from Ref. 36 with the permission of Elsevier.

Gas storage – current understanding and outstanding issues. To understand the storage of natural gas in shales, one first has to understand their origins. Kerogen is the main component of shale's organic matter. Shale gas is produced in kerogen when it was matured under high pressure and temperature.[37-38] While some produced gas molecules remain trapped (dissolved) in the tight organic phase, some leached into the nanopores in kerogen.[37] Because of the interactions between the gas molecules and the walls of nanopores in the kerogen, some gas molecules will be adsorbed on pore walls.[39] Because of the molecular exchange between the tight organic phase, nanopores in the organic matter, and nanopores in the inorganic matter phase, gas molecules are eventually distributed throughout the entire shale as dissolved gas, free gas in the nanopores (in both organic and inorganic matter), and the adsorbed gas on the walls of the nanopores (see Figure

1-5).[40]

Gas adsorption is important in shales. For instance, the adsorbed methane can account for 60% of its total storage in 2 nm wide pores.[8] Gas adsorption in a shale is affected by factors such as pressure, temperature. The gas adsorption behavior in Devonian shale samples CSW2-3434 is illustrated in Fig. 1-6. The adsorption increases as pressure increase, but decreases as the temperature increase.[41-43] Gas adsorption also depends on the size and compositions of shales' pores, both of which depend on the petrochemistry and petrogeology of the shales. For this reason, the gas adsorption is also affected by the content and depth of the shale samples. A positive correlation between the gas adsorption capacity and the total organic carbon (TOC) of shales has been demonstrated.[42]

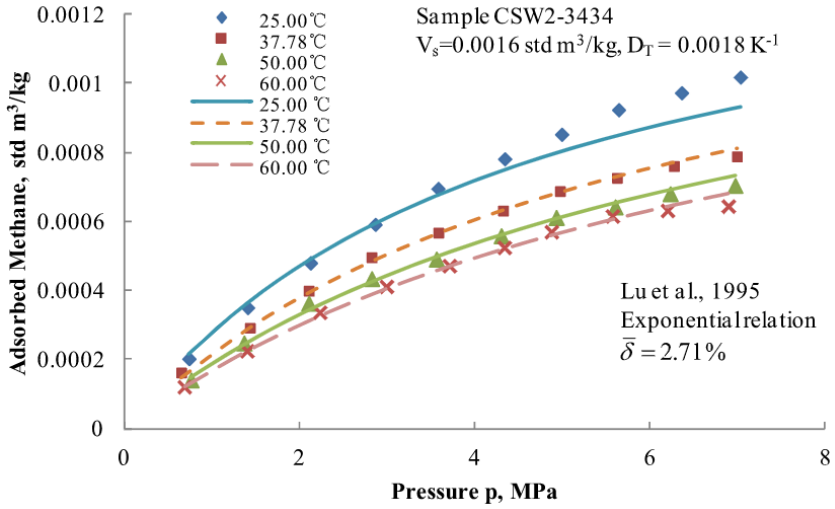

Figure 1-6. Gas adsorption isotherm of Devonian shale samples CSW2-3434. This figure is reproduced from Ref. 43 with permission from Elsevier.

To quantitatively describe the gas adsorption, many models have been proposed. For example, the Langmuir models, Freundlich models, and mixed Langmuir-Freundlich models have been used in the literature.[44-46] The Langmuir model is often effective and is the most widely used model. In this model, the gas adsorption C_g of a surface in equilibrium with a gas phae hold at a pressure p is expressed as

$$C_g = \frac{C_e p}{p + p_e} \tag{1-1}$$

where C_e is Langmuir concentration constant, and p_e is the Langmuir pressure constant.

Research on the adsorption of shale gas has focused mostly on single-component adsorption of methane on the surface of shale's nanopores. However, as shown in Figure 1-3, shale gas contains a sizable fraction of hydrocarbons with longer chains, with ethane being the most abundant species. The research on the surface adsorption of multicomponent gas mixtures is relatively limited (available work mostly focused on the competitive adsorption of $CH_4/N_2/CO_2$ gas species in shales, which plays an important role in enhancing shale gas recovery).[47-52] At a fundamental level, the current understanding of such adsorption relies on the adsorption models developed in other fields. For instance, the extend Langmuir isotherm model is an extension of the classical Langmuir model by considering the interactions between the adsorption of different species.[49, 53-55] For gas adsorption from a binary gasmixture, the adsorption capacity of each component on a surface can be expressed as

$$C_{g,1} = \frac{C_{m,1}K_{L,1}p_{e,1}}{1+K_{L,1}p_{e,1}+K_{L,2}p_{e,2}} \quad (1\text{-}2a)$$

$$C_{g,2} = \frac{C_{m,2}K_{L,2}p_{e,2}}{1+K_{L,1}p_{e,1}+K_{L,2}p_{e,2}} \quad (1\text{-}2b)$$

where $C_{g,i}$ is the equilibrium adsorption capacity for species i. $C_{m,i}$ and $p_{e,i}$ is are monolayer capacity and gas partial pressure for species *I*, respectively. $K_{L,i}$ is the adsorption coefficient that is fitted from experiments.

While significant progress has been made to understand the adsorption of gas on shale's pore walls, some outstanding issues exist, especially on the surface adsorption of multicomponent gas mixtures. In particular, *a critical issue is that the understanding of the competitive adsorption behaviors of shale gas inside nanopores under realistic reservoir conditions is limited*:

Research on the adsorption of shale gas mixtures is scarce at present, but some insights can be gleaned from the extensive work on the thermodynamics of multicomponent gas in other industrial applications.[52, 54-60] For example, theoretical modeling based on the extended Langmuir model[55] and the Ideal Adsorbed Solution (IAS) model, as well as numerical simulations,[52, 56, 58] indicated that there exits complex competition between the adsorbed species, and such competition affects the net adsorption of each gas species. Therefore, it is safe to expect such competition to exist for shale gas as well. However, details of such competition are unclear and many questions

are unanswered. For example, what is the nature of such competition for the dominating gases (CH_4 and C_2H_6)? How such competition affects the adsorption of each species? How such competition is affected by the size of the nanopores and the gas pressure? Can the existing surface adsorption models predict the adsorption of different gas species accurately?

Gas transport – current understanding. Gas transport is the most essential process underlying shale gas recovery. Research on gas transport for shale gas recovery can be divided into two major thrusts. The first research thrust focuses on the effective transport properties of gas (e.g., the permeability) through individual nanopores and in the shales. The second research thrust focuses on the recovery of gas from nanopores or shales.

The transport properties of gas in nanopores and nanoporous media have been investigated extensively. It is well established that, as fluid-wall interactions become comparable or even more important than fluid-fluid interactions, which can occur as the pore size approaches molecular size, the fluid transport inside the pore can no longer be described using the Navier-Stokes (NS) equations.[6-7, 61] The Knudsen number is commonly used to characterize the relative importance of fluid-fluid and fluid-wall interactions: $\mathrm{Kn} = \lambda/d$, where λ is the gas mean free path and d is the dimension of pores. As shown in Fig. 1-7, the fluid flow inside a pore can be classified into four regimes, i.e., the viscous flow (or continuum flow regime; $\mathrm{Kn} < 0.01$), the slip flow regime ($0.01 < \mathrm{Kn} < 0.1$), the transition flow regime ($0.1 < \mathrm{Kn} < 10$), and the free molecular flow regime ($10 < \mathrm{Kn}$).[62-64] The NS equations with no-slip boundary conditions are only valid in the viscous flow regime. In the slip flow regime, the NS equations are still valid, but slip boundary conditions must be applied. In the transition flow and free molecular flow regimes, the NS equations are not strictly valid even with modified boundary conditions.

A host of processes have been identified to affect the gas transport behavior in nanopores. For example, gas slippage and Knudsen diffusion have been shown to be important for the flow with modest Kn numbers. Furthermore, surface diffusion is throught to play a key role in nanopores when the adsorption of gas on pore surface becomes strong.[21, 65] Specifically, surface diffusion is regarded as a process that involves the motion of molecules adsorbed on the pore surface and it is

affected by temperature, pressure, surface roughness, the interactions between gas and wall, among others.[66-68] A variety of physical models, including hopping model, long jumps model, rebound jumps model[69] have been used to describe surface diffusion. The hopping model is the simplest model, in which surface diffusion is regarded as an activated process with molecules hopping between nearby adsorption sites. The capacity of the adsorption sites is determined by the equilibrium between the gas adsorption and desorption process, which can be approximated using the Langmuir isotherm.[70]

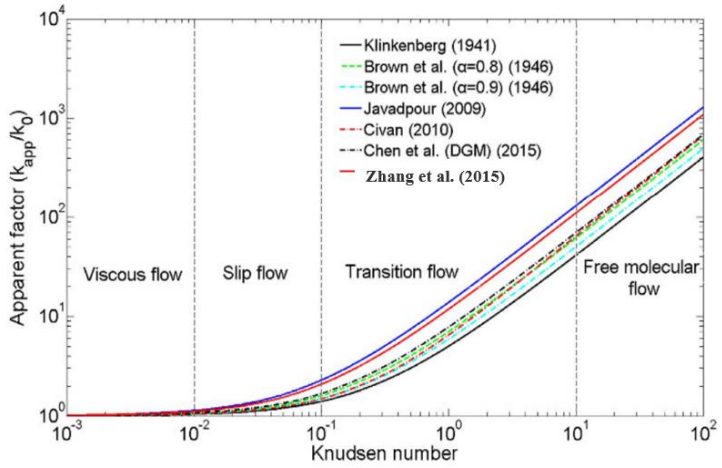

Figure 1-7. A comparison of the permeability of fluids through a pore as a function of the Knudsen number obtained using different models. The different flow regimes are also identified. This figure is reproduced from Ref. 62 with the permission of Springer Nature under the Creative Commons CC BY license.

The fundamental understanding of gas transport in individual nanopores helped to advance the description of gas transport in shales. Due to the deviation of the transport behavior of fluids in narrow pores from that in wide pores, classical Darcy's law, widely and successfully used in describing the gas transport in conventional reservoirs, is no longer accurate for the gas transport in shale reservoirs. The limitation of Darcy's law has been addressed using various models that were derived based on the understanding of gas transport in single nanopores. For example, the Klinkenberg model and the Knudsen diffusion model have been developed to predict the gas transport in nanopores. [67, 71] More refined models that are capable of describing the gas transport in all four flow regimes have also been proposed (see Fig. 1-7).[33, 40, 72-77]

The second thrust of research on gas transport in shales focuses on the recovery of gas from shales. Typically, the macro-fractures produced by hydraulic fracturing and the nanopores within shales are considered simultaneously at the continuum level using multiscale models.[49, 51, 56, 78-86] The gas adsorption is often neglected in these models,[87] but nanoscale transport physics such as gas slippage and Knudsen diffusion are often included. These models are useful for understanding the overall behavior of gas recovery from shale reservoirs. For example, the model predicts the gas recovery follows a diffusive scaling law at the early stage (see Fig. 1-8) and the gas production rate is two orders of magnitudes high than the predictions based on Poiseuille's law.[87-88] More recently, continuum models that consider not only the free gas in nanopores but also the adsorbed gas on pores walls have also been reported. These models have been used to investigate the impact of adsorbed gas inside Kerogen nanopores on the reservoir production rate and to clarify the correlations between the amount of kerogen in shale matrix and the gas production rate.[78-80]

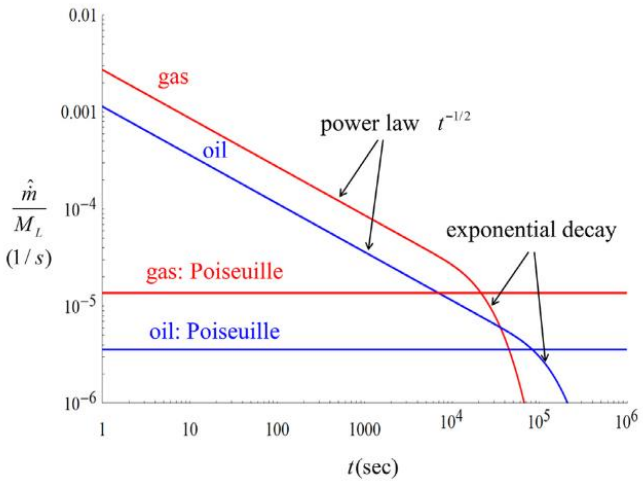

Figure 1-8. Shale gas production rate given by a theoretical model based on the compressible Naiver-Stokes equatins. The gas and oil production rate at the early time follows the diffusive scaling law and the values are 2 orders of magnitude higher than the prediction by Poiseuille's law. This figure is reproduced from Ref. 88 with the permission of Elsevier.

In addition to continuum simulations, MD simulations are gaining popularity in studying the recovery of shale gas[89] since they can model the thermodynamic and hydrodynamic behavior of shale gas inside shales without the many assumptions that must be made in continuum models. However, because MD simulations are limited to small time and length scales (typically tens of

nanoseconds and nanometers), these simulations must be carefully designed and interpreted to help understand the gas recovery behavior at the core- and field-scales.

Gas transport – Outstanding issues. Thanks to prior studies on shale gas recovery,[49, 51, 56, 81-86] many useful insights into the gas transport (recovery) in (from) shales are available. However, some outstanding issues remain to be addressed.

First, how the gas recovery behaviors (e.g., gas recovery rate and its scaling law) are affected by unique phenomena in nanoconfined gas (e.g., surface adsorption) is not well understood. Though some of these phenomena have been incorporated into continuum models (e.g., the Klinkenberg model and the Knudsen diffusion model), the first-principle validation of these models is still lacking. In fact, in many of these models, the interactions between gas and pore walls are treated using kinetic theory, which neglects the adsorption of gas molecules on the pore wall. In nanopores with a width that is comparable to the size of fluid molecules, this simple treatment is likely inadequate, but how gas-wall interactions and the ensuing surface adsorption affect gas transport and recovery is rarely studied quantitatively. In particular, their effect on the scaling law of gas recovery is not fully understood. Prior research has shown that the gas recovery at the early stage of the recovery process follows a diffusive scaling law[87]

$$\mathrm{PR}(t) \approx \alpha t^{-1/2};\ \ \mathrm{RF}(t) \approx \beta t^{1/2} \tag{1-3}$$

where $\mathrm{PR}(t)$ is the gas production rate, $\mathrm{RF}(t)$ is the recovery fraction, and α and β are the pre-factors that depend on the working conditions of the gas recovery process (e.g., pore size, gas pressure, etc.). Nevertheless, gas recovery rate with other behavior (non-diffusive scaling law) has also been observed from 25 wells of the Barnett shale,[90] where the recovery rate obeys a super-diffusive scaling law $\mathrm{RF}(t) \approx \beta t^{m}$ with $\mathrm{m} \approx 0.6$. The origin and physics of this super-diffusive scaling law are still unknown. Some studies have shown that the desorption of gas from pore walls tends to make the decay of gas production rate slower, but its impact on the scaling law of gas recovery was unknown.[91]

Second, the recovery of multicomponent gas mixture is not well understood. Most studies of shale gas recovery focus on the single-component (methane) scenario. However, as shown in Fig.

1-3, there is usually a modest fraction of heavier hydrocarbons in shale gas and the recovery of these more valuable hydrocarbons is of great interest. The recovery rate, sequence, and scaling law of the recovery of the different species are little understood. For example, how is each gas species extracted from nanopores? Is some gas species extracted preferentially over other species? How does the transport coupling between different gas species affect the recovery of each species? Answering these questions experimentally is challenging due to the difficulties in accessing the gas composition in shale prior to gas recovery operations. Continuum models can be valuable tools for answering these questions. However, these models must be built upon adsorption and transport models for multicomponent gas in nanopores, which themselves are not well developed.

1.2.2 Drying of nanoporous materials

Drying is multiphysics progress during which liquids are removed from a material (often porous) via the combination of heat transfer, mass transfer, and phase change. Drying of porous media has abundant applications in areas such as processing of ceramics, foodstuff, paper, and wood.[1, 13, 92] It is also involved in soil remediation and recovery of volatiles from subsurface.[2]

Numerous technologies have been developed for the effective drying of porous materials. For instance, infrared radiation drying has been adopted for drying foodstuff. Despite great progress, drying remains the most energy-intensive process in many industrial processes, especially in the processing of nanoporous materials, where capillary effects are strong and permeability is small. Therefore, there has been a long-standing need to improve existing drying methods or develop new drying technologies with low energy cost, and research on drying porous media is of substantial scientific and practical interest. Among the approaches for studying drying, theoretical and computational research has the advantage of offering mechanistic insight into the macroscale drying behavior and has been pursued extensively. Below various models and the insights from these models are briefly summarized.

Current understanding. Drying of porous media is essentially a multiphase transport problem. As illustrated in Fig. 1-9a, porous media typically feature pores with a wide range of sizes (a few nanometers to sub-millimeters is common in nanoporous media) and connectivities.

Therefore, multiphase transport during drying has a distinct multiscale character. Because of these multi-faceted (multiphysics, multiphase, and multiscale) features, modeling the drying of porous media is a challenging problem.[11-12]

Many numerical models have been developed to address the difficulty in modeling the drying of porous media. There are generally two categories of models: pore-scale models and macro-homogeneous models. Macro-homogeneous models treat porous media as a continuum. They resolve neither the microstructures of porous media and nor the physical processes in pores (e.g., the capillary flow at the corners of non-circular pores, viscous fingering, etc). Instead, they use phenomenological laws to describe the multiphase transport involved in drying. These models may predict drying at large time/length scales effectively,[9, 93] but they provide limited insight into the fundamental physics behind the drying. To address this limitation, pore-scale models that resolve the heat/mass transport within porous media's microstructures have been developed.

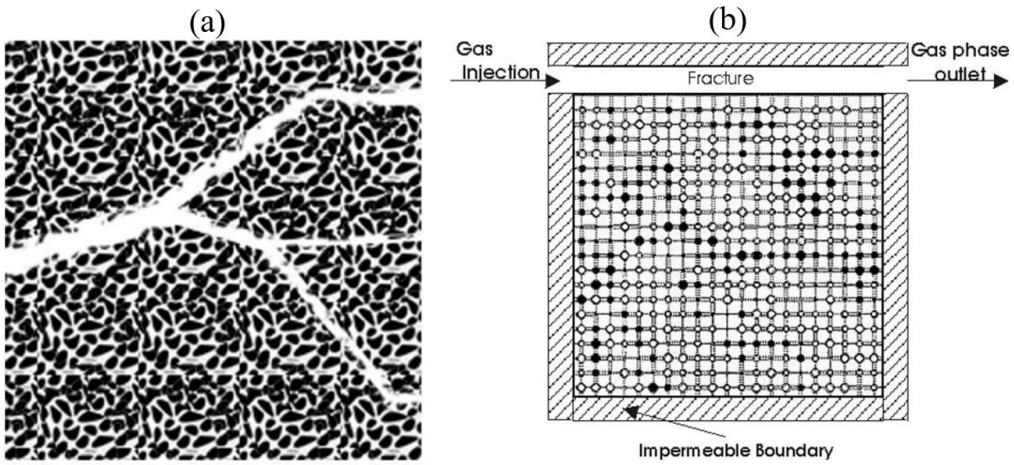

Figure 1-9. (a) A schematic of a porous medium. The black (white) region represents the solid (pore space). (b) A pore-network representation of a porous medium. These figures are reproduced from Ref. 94 with the permission of Elsevier.

Many kinds of pore-scale models exist. In some models, the Navier-Stokes (NS) equations are solved to predict the heat and mass transfer inside the porous media using methods such as the Lattice Boltzmann (LB) method.[95,96] In particular, LB models can resolve fluid transport under vapor-liquid coexistence by solving the concentration distribution functions.[97-99] In other models, the pore space inside porous media is represented using a network of pores and throats, as shown

in Fig. 1-9b. The transport rules within the network system are derived from the first principle, e.g., mass and momentum conservation law.[10, 94, 100-102] Much effort on modeling the drying of porous media has been based on pore-network models because of their excellent balance between resolving pore-scale physics and computational efficiency.[10, 94]

The pore network models are constructed to mimic the complex geometry of the interstitial space inside porous media. Large voids in porous media are simplified as pore bodies, and the connections between these void spaces are simplified as pore throats. The construction of the pore network model to represent real porous media has been widely investigated and much progress has been made.[103-105] For example, micro-computerized-tomography (micro CT) has been used to scan porous media and re-generate their pore space as 3D images. Those images can then be converted into pore network models using the maximum ball algorithm.[103, 105]

The first pore network model was applied to drying in 1954,[106] and more sophisticated models have been developed since then.[10, 101, 107-110] For instance, factors such as gravity,[111] temperature gradient,[10, 112] viscosity,[94] and corner flows[94] have been incorporated into pore network models. These models helped researchers explore the impact of complex pore geometry and mixed wetting property of pore walls on drying. For instance, these works showed that the distribution of mixed wettability considerably impacts the drying rate, and the drying rate is lowered when a drying front encounters horizontal hydrophobic layers.[113]

Thanks for extensive experiments and pore-scale modeling, many key features for drying of porous media have been revealed and their underlying physics clarified. The most widely studied drying scenario is shown in Fig. 1-9b, where the top surface of a partially saturated porous medium is exposed to external gas flow.[100, 108, 114-115] Such a scenario is widely encountered in the drying of foodstuff and soil remediation. Its typical drying curve, which describes the evolution of the drying rate as a function of the residual liquid saturation in the porous media is presented in Fig. 1-10. Four periods can be identified during the drying process: (1) the surface evaporation period, during which the drying rate decreases rapidly, (2) the constant rate period (CRP) during which liquid flow paths are well-connected to the top surface, (3) the falling rate period (FRP), during which

liquid clusters in the porous media become gradually disconnected from the top surface, and (4) main cluster disconnection (MCD) period during which the drying rate is very low.

The drying time is often dominated by the last three periods. In the constant rate period (CRP), the largely constant drying rate is mainly contributed by the capillary flow. Specifically, capillary flow delivers liquids from the interior of a porous medium to its top drying surface through wholly or partially wetted pores. In the falling rate period (FRP), while some of the liquid clusters are still connected with the drying surface, liquid clusters inside the porous media start to disconnect from each other. Because the external gas flow lowers the vapor density near the top surface, the vapor in the porous media is transferred to its top surface mainly by diffusion, thereby leading to a rapidly decreasing drying rate. In the last period, liquid clusters lose connection with the top drying surface and become isolated from each. During this period, the pore space directly connected to the drying surface is completely dried out and the drying front moves deeper and deeper into the porous medium until the end of drying.

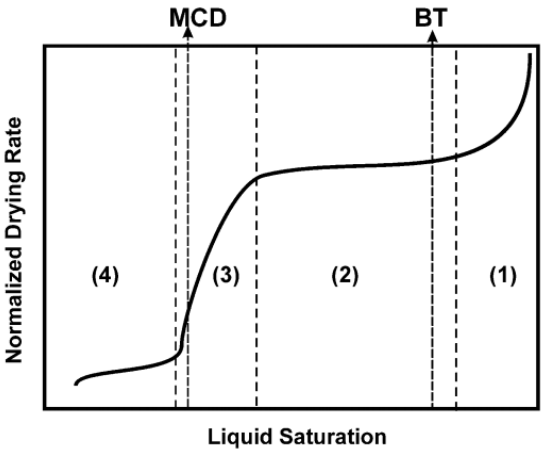

Figure 1-10. A typical drying curve for a porous medium dried by an external gas flow (see Fig. 1-9b). BT and MCD are breakthrough and main cluster disconnection, respectively. This figure is reproduced from Ref. 115 with the permission of Elsevier.

A much less studied drying scenario is when a purge gas is driven through a porous medium to remove its liquid content. This kind of drying process has been used for recovering and recycling the hydrocarbon solvents in coal-solvent mixtures produced during the dewatering of coal slurries. Dewatering of coal fines is an indispensable step for recovering the fine coal from coal tailings, but current dewatering technologies have shortcomings such as high cost and low efficiency.

Because of this, 70-90 million tons of coal tailings are discarded each year, according to the U.S. national research council.[116] This has caused significant economic loss and led to many environmental issues. Recently, the hydrophobic-hydrophilic separation (HHS) process has been developed to separate coal fines from coal tailings and dewater coal fines with size down to micrometers.[117-118] In the HHS process, a hydrophobic solvent, typically a hydrocarbon with low surface tension and boiling point (e.g., pentane), is introduced to a coal-water slurry. Because of the coal particles' hydrophobicity, they spontaneously transfer from the waterin to the hydrophobic solvents. Therefore, water and hydrophobic solvents are phase separated, and coal particles are loaded in the hydrophobic solvents.

Recovering and recycling the spent solvent in the coal-solvent mixture is essential for the economic operation of coal-dewatering based on the HHS technology. The recovery of solvents can be achieved by pumping a purge gas through the coal-solvent mixture positioned above a filter (see Fig. 1-11). Under the action of purge gas, liquid solvents are displaced through the filter and a filtration cake saturated with solvent is formed (cf. panel a). Next, the purge gas invades the filtration cake against the capillary force and eventually breaks through the filtration cake to form gas transport pathways (cf. panel b). Thereafter, drainage and evaporation occur concurrently until all solvents are removed from the cake (cf. panel c).

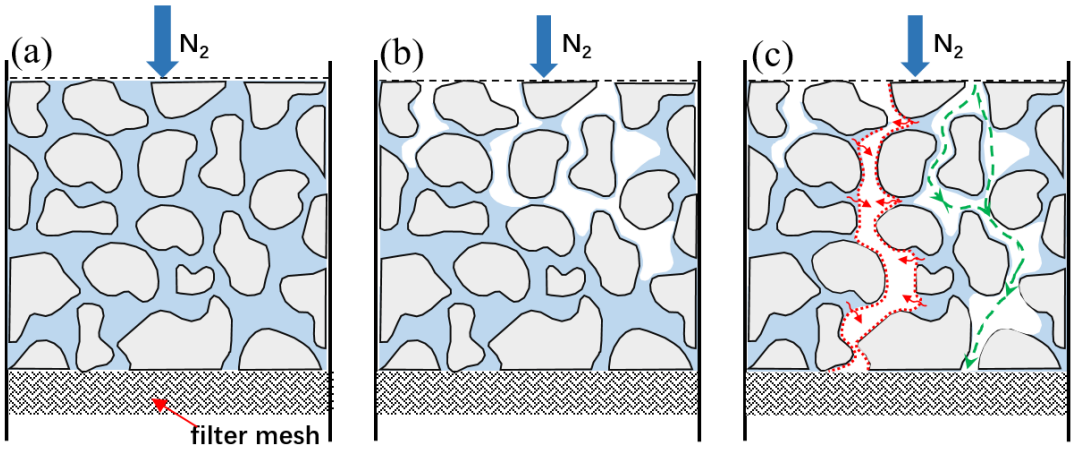

Figure 1-11. *A schematic of drying a filtration cake by flowing a purge gas through it*. This figure is reproduced from Ref. 119 with the permission of Elsevier.

Outstanding issues. While much progress has been made to understand the drying of porous media, some issues do exist, especially for the less-studied drying scenarios. In particular, the drying of porous media by purge gas flowing through them is still poorly understood due to some unique features in such drying.

First, drainage and evaporation processes can occur concurrently during the last stage of drying (see Fig. 1-11c). The coupling between these processes and how such coupling affects the drying kinetics is unknown. Initially, the drying rate is dominated by the drainage process because most pore space is fully or partially saturated by liquid solvents. As drying proceeds, the importance of drainage becomes weaker, while the evaporation process becomes pronounced[120-121].

Second, how rarefication affects the vapor and purge gas transport and thus drying is little explored. The pore size in a porous filtration cake depends on the size of coal particles. For coal particles with diameters less than a few micrometers, the pore size in the cake can be as small as a few hundred nanometers.[122-123] Here, conventional gas transport models are not strictly valid (see Section 1.2.1), e.g., the gas slippage on pore walls must be considered. Given that vaporization of liquid solvents and the transport of these vapor dominates the final stage of drying, conceivably, the rarefication effect should impact drying, although the exact impact is still unknown.

Finally, multicomponent transport at the pore scale needs to be treated more rigorously than practice in prior literature. The liquid solvent in coal filtration cakes is highly volatile and their vapor pressure can be comparable to that of the purge gas. Therefore, the multicomponent gas transport behavior can involve strong coupling between purge gas and vaporized solvents, which cannot be described well using classical convection-diffusion equations. Instead, more advanced models such as the dusty gas model (DGM)[20-21] should be used to describe the multicomponent gas transport in filtration cakes. However, these advanced models have not been incorporated into the pore network models to study drying.

1.3 Effective Solution of Transport Processes in Heterogeneous Media

Solving transport phenomena problems in heterogeneous media effectively is important in many engineering applications but is often challenging. These problems can be classified into two broad categories. In forward problems, the structure of the porous media and the full mathematical model of the transport phenomena are given, and the objective is to predict the transport behavior. In inverse problems, some observables related to the transport phenomena (e.g., velocity or temperature field) and part of (or the entire) mathematical model of the transport phenomena are given, and the objective is to predict the structure of the porous media or some parameters in the mathematical model (e.g., the transport properties). Inverse problems are important for materials design and optimization, e.g., how to design the structure or loadings of a thermal composite to achieve a specific thermal conductivity. [124]

Forward and inverse transport phenomena problems have been investigated extensively, and the general approach is to formulate them into physics-based partial differential equations and solve these equations approximately. Recently, new, data-driven approaches for solving these problems are emerging. The basic idea is to leverage large dataset and statistical/machine learning techniques to solve these problems without necessarily resolving the physical processes underlying these phenomena. In this dissertation, we explore the solution of forward and inverse transport phenomena problems using machine learning approach, i.e., predicting porous media's transport properties and constructing the structure of thermal composites from their temperature fields.

1.3.1 Predicting the transport properties of porous media

The effective transport properties of porous media, e.g., diffusivity, thermal conductivity, and permeability, greatly affect the applications of these media.[18] Predicting these properties is essential for applications such as drying of porous cakes[125] and gas recovery from shales.[16-18, 87] To obtain the effective transport properties of porous media, many methods have been developed. For instance, pore scale simulation, in which the governing equations for related transport phenomena are solved in the pore space of the porous media, is a classical approach.[17, 126-127] This

approach can be highly accurate. Nevertheless, significant computational cost is often required when solving the governing equations for porous media with large dimensions and/or small pore size. In fact, the computational cost can become prohibitive if the topology and structure of the porous structure evolve as a function of time, which occurs in many problems, e.g., the charging/discharging of Li-air batteries and the dissolution/deposition of chemical species in rocks.

To circumvent the high computational cost of pore scale models in predicting the transport properties of porous media, many empirical formula have been developed. For example, the Bruggeman equation has been widely used to correlate the effective diffusivity of porous media with their porosity:

$$D_e = \varepsilon^{\beta+1} \tag{1-4}$$

where D_e and ε is the effective diffusivity and porosity of the porous medium, β is the geometry factor, which depends on the structure of the porous media. The Bruggeman equation can predict the effective diffusivity accurately for some special porous material (i.e., porous materials made of packed spheres[128]) with little computational cost. Nevertheless, the empirical models often lack generality, and their predictions are inaccurate for complex porous media. Therefore, developing methods for predicting the transport properties of diverse porous media with small computational cost but high accuracy remains a challenge.

Machine learning approach. Recently, machine learning is emerging as a new approach for the efficient and accurate prediction of the transport properties of porous media. Based on the availability of data to the learning machines and the learning algorithms, machine learning models can be divided into three main classes: supervised learning, semisupervised learning, and unsupervised learning. In supervised learning models, the machine learning model is trained to learn the correlations between the input and output responses (or label) data. Therefore, both the input and output data are provided to the machine learning model during the training step. Typical supervised learning models include support vector machine, decision tree, and neural networks. In unsupervised machine learning models, the models are trained to explore data analysis and identify

inferences or standard features from the input dataset without their output responses. The principal component analysis (PCA), autoencoder, and k-means are the most common unsupervised learning models. The semi-supervised learning models fall between the supervised and unsupervised learning model, where the input data and part of the output responses are adopted during the training step.

Among the many machine learning techniques, the artificial neural network (ANN) has received much attention. In an ANN, several layers of neurons are connected together to represent an input-output relation. An ANN can be trained using a large amount of data so that the correlations between the input and output are captured by the interactions between the neurons in the network. Machine learning based on ANN with more than two layers is usually termed deep learning. Deep learning has been used to solve transport phenomena problems in heterogeneous media.[129-131] For instance, surrogate models based on deep learning were developed for uncertainty quantification in single-phase flow in porous media.[132-133] These models outperformed conventional surrogate models and showed good predictive performance for stochastic and heterogeneous structures.

Deep learning has also been adopted to predict the effective transport properties of porous media by taking their structures as input. The effective transport properties of a porous medium are largely determined by its microstructure. During training, a deep learning model is trained (parameterized) to capture the correlations between the microstructure and transport properties in a large number of porous media. Once trained, the model can potentially predict the property of porous media with similar structures in the training dataset with little computational cost. The effectiveness of such an approach depends critically on whether the microstructures (or more precisely the patterns in them) can be extracted effectively. In this regard, the convolutional neural network[134] (CNN), which is effective in extracting features and critical geometry patterns from visual imagery,[135-137] has gained the most attention for predicting the effective transport properties of porous media.

Figure 1-12 shows a typical computational framework for using the CNN model to predict the effective transport properties of porous media. The framework consists of four basic steps. The first step is to generate enough data for the training and testing process. Many samples of porous media with diverse porous structures are generated and their corresponding transport properties are obtained. In the second, optional step, parameters based on physical or domain knowledge may be included as part of the input to CNN model to improve its prediction. In the third step, the CNN model built in the second step is trained using the training dataset. Finally, the trained model is deployed to predict the effective transport properties of new porous media (e.g., those in the test dataset). Using this approach, the effective transport properties of porous media has been predicted rather effectively with very little computational cost.[135-137] As illustrated in Fig. 1-13, in a rcent work, the CNN model showed accurate predictions for different porous media with porosity ranging from 0.1 to 0.25, and performed much better than the empirical Kozeny-Carman formula.

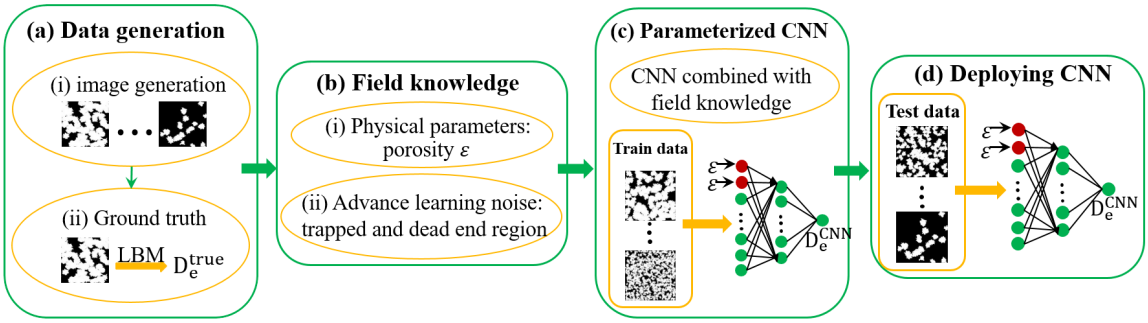

Figure 1-12. A typical computational framework for using convolutional neural network to predict the effective diffusivity of porous media from their images. This figure is reproduced from Ref. 137 with the permission of Springer Nature under the Creative Commons CC BY license.

Outstanding issues. Even though deep learning models have shown promise in predicting the transport properties of porous media, some issues remain. In particular, to what extent deep learning models can predict the transport properties of *realistic* porous media with complex micro-structures is still unclear. The porous media used in previous deep learning works are constructed with limited structure variability with a small range of porosity.[135] However, the microstructure of real porous media is not well-defined and complex topologies, for instance, dead-end pores and trapped pore space, are ubiquitous. Whether deep learning models can extract these features, resolve their correlation with the porous media's transport properties is still unknown. Moreover,

most of the existing deep learning models were tested for porous media with limited variation of transport properties, e.g., the permeability of the samples tested in previous models varies only by less than an order of magnitude (see Fig. 1-13 a).[135] In reality, the porosity of sandstone samples can range from 4% to 24% and their effective permeability for sandstone sample may range from 0.01 to over 5×10^4 millidarcy,[138] without simple correlation with their porosity. Porous media with such a wide range of transport properties has not been studied using deep learning models yet.

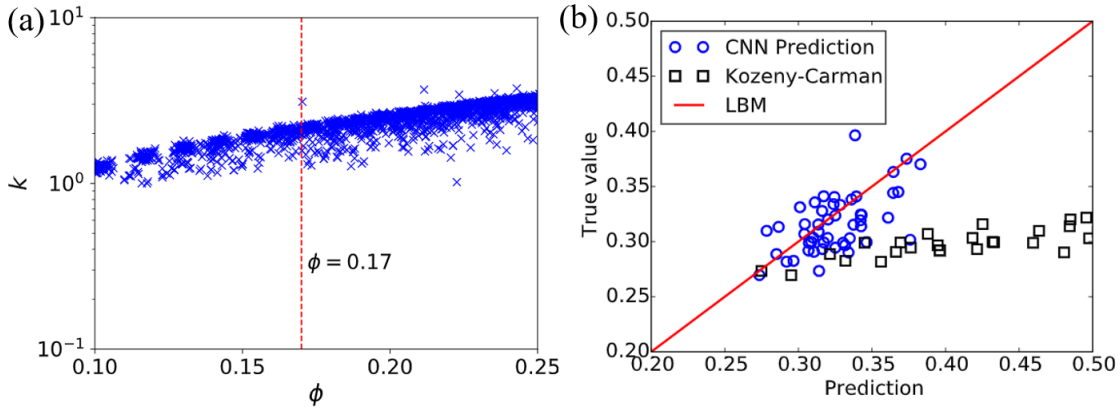

Figure 1-13. (a) The relation between the porosity and the permeability of porous structure in Ref. 135. (b) comparisons between the predictions by CNN model and the empirical Kozeny-Carman formula, the LBM predictions are considered as the ground truth. These figures are reproduced from Ref. 135 with the permission of Elsevier.

1.3.2 Constructing heterogeneous structures from transport phenomena data

Many techniques have been developed to solve inverse problems with various degrees of success. Of these techniques, the Monte Carlo (MC) methods are especially widely used, e.g., to solve inverse problems in subsurface flows, in civil and petroleum engineering applications.[139-140] However, MC methods, and in fact many other inverse problem solvers, lack well-established convergence criteria. Furthermore, these methods often require significant computational cost, which become prohibitive for inverse problems involving complex geometry and large parameter space.[141] These limitations are at least in part due to the fact that many inverse problems involving transport phenomena are ill-posed.

Machine learning-based models can potentially address the difficulties encountered by inverse problem solvers. For example, Gaussian process regression (GPR) models can predict the thermal properties of orthotropic materials accurately using temperature measurement as an input. The GPR models can provide predictions with an average error $< 10\%$ for the entire testing dataset even when random noise is introduced to the input data.[142] Besides, ANN has been adopted to solve nanophotonics inverse design problems by training the model to learn and approximate the interaction rules between nanophotonics. It has been demonstrated the machine learning model can solve the inverse design problem faster than the conventional solver.[143] Nevertheless, these machine learning based models have difficulties in solving high-dimensional inverse problems.

The challenge associated with high dimensionality may be addressed using deep learning models. For instance, CNN models, a popular type of deep learning models, have been used as surrogate models to quantify the uncertainties of multiphase flow in heterogeneous media with the media' permeability fields as input.[144] As mentioned in Section 1.3.1, CNN has also been adopted to predict the effective transport properties of porous media efficiently.[135, 145-147] Besides, deep learning models have been used in inverse molecular or system design to discover new materials with desired functionality. For instance, the generative adversarial network is used to optimize the redox flow batteries, and to design routes for organic compounds.[124, 148] Nevertheless, at present, the application of deep learning methods to inverse problems related to transport phenomena in heterogeneous media is limited and it is far from clear that the deep learning models is effective in solving these problems when the dimensionality of the data is high.

Another potential limitation of deep learning models for solving inverse problems is that these models often require a large amount of input data to ensure their prediction accuracy. Gathering large datasets is difficult and time-consuming. This is especially true when high-dimensional data are involved because a large number of sensors must be deployed and/or numerous measurements must be made. Furthermore, deploying a large number of sensors can potentially affect the physical processes in the system, thereby introducing systematic errors into the solution.[149-150] Because of

the above reasons, only sparse input information may be used as input to deep learning models. Under this condition, the inverse problems are likely ill-posed.[151-152] To what extent deep learning models can work with sparse input and how to improve their performance when the input data is limited are important issues that must be tackled.

1.4 Scope of This Dissertation

Transport phenomena in heterogeneous media play a key role in a wide range of applications, including shale gas recovery, drying of porous media, and engineering design and diagnosis. Although significant progress has been made in research on these phenomena, new challenges for the accurate understanding and prediction of these phenomena involving novel physics continue to emerge at the frontier of engineering practice. Meanwhile, many long-standing challenges for accurately and efficiently solving transport phenomena problems in heterogeneous media remain. In this dissertation, these challenges in several engineering applications are addressed.

In Chapter 2, the recovery of single-component shale gas from single nanopores is studied by molecular dynamics simulations. The van der Waals gas-wall interactions, which are neglected in many prior models, are considered from in the molecular dynamics simulations. The gas storage capacity is computed from the distribution of gas molecules across the nanopore to delineate the contribution of free and adsorbed gas to the storage. The recovery of gas from the nanopore is simulated by disabling the barrier between the pore entrance and a low-pressure gas reservoir. To help understand the gas production rate and its scaling law obtained in the simulations, separate simulations are performed to quantify the transport diffusion coefficients of gas inside nanopores. Furthermore, a continuum gas recovery model that considers gas adsorption and desorption is built and solved to help clarify the origins of the gas recovery scaling law observed in the molecular dynamics simulations.

In Chapter 3, the storage of methane-ethane mixtures in single nanopores and extraction of these gas mixtures from nanopores are investigated using molecular dynamics simulations. The contributions of adsorbed gas and free gas to the total storage capacity and the relative composition of the two species inside the nanopores are examined at different reservoir pressure and pore size.

The physical origins of the observed adsorption behavior of these gas species are clarified, and the validity of the ideal adsorbed solution (IAS) theory in predicting the gas adsorption is delineated. The recovery of the gas mixture from nanopore is simulated. The scaling law of the gas production rate and the relative recovery rate of the two gas species observed in the simulations are quantified. These observed gas recovery behaviors are rationalized using scale analysis based on non-equilibrium thermodynamics and the transport coefficients computed from separate molecular simulations.

In Chapter 4, a pore network model is developed to investigate the purge gas-assisted drying of nanoporous filtration cakes initially saturated with highly volatile solvents. The model considers, *for the first time*, the concurrent drainage and evaporation during the drying of a porous medium. The dusty gas model is incorporated, *for the first time*, into the pore network model to describe the multicomponent gas transport through pore necks. The net drying rate and the contributions by the drainage and evaporation effects are quantified. Several different stages of the drying process, each controlled by different physical processes, are identified. The interactions and coupling between the drainage and evaporation effects during different drying stages are analyzed by examining the evolution of the liquid saturation distribution inside the porous medium. Auxiliary simulations, in which the pore size in selected regions in the porous medium is reduced, are performed to help delineate the coupling between drainage and evaporation effects.

In Chapter 5, the effective diffusivity of two-dimensional porous media is predicted from their images using convolutional neural networks (CNNs). The emphasis of this work is to test whether deep learning models can accurately predict the effective transport properties of realistic porous samples with diverse microstructures and complex topologies (i.e., dead-end pathways and trapped pore space), which has not been widely used in previous deep learning models. CNN models with different architectures are constructed and trained using datasets featuring porous samples with highly challenging microstructures and effective diffusion coefficient that span more than 10 orders of magnitude. The computational cost of the CNN models is measured and compared to classical pore-scale modeling. The accuracy of the trained models is quantified in far more detail

than commonly practiced in deep learning studies. The limitations of current models and potential improvement strategies are discussed.

In Chapter 6, the heterogeneous thermal conductivity field inside a composite is constructed using a deep learning model, with temperature fields inside the composite as input. The composites feature circular, high-conductivity fillers randomly distributed inside a low-conductivity matrix. This high-dimensional, inverse problem is solved using a deep convolutional encoder and decoder model (U-net). In this model, the temperature field in a composite is represented using images and is mapped to the thermal conductivity field. The performance of the deep learning model is evaluated when the temperature input has different resolutions: a full-scale input (the temperature at all points in the composite is known), coarse-grained input (true temperature is available only at selected points in the composite), boundary-only input (true temperature is only available on the boundary of the composite). Strategies for improving the performance of the U-net model are discussed and tested.

In Chapter 7, the major contributions of the research in Chapters 2-6 are summarized.

Chapter 2. Shale Gas Recovery from Single Nanopores

Disclosure:

This work has been published by the American Physical Society: Wu, H.; He, Y.; Qiao, R., Superdiffusive gas recovery from nanopores. *Physical Review Fluids* **2016,** 1, (7), 074101.

2.1. Introduction

Natural gas production from shale formation has received significant attention recently and can potentially lead to a new global energy source. For example, according to the U.S. Energy Administration, shale gas provides the largest source of the growth in U.S. natural gas supply during the past decade, and its share is expected to grow continually in the future.[26] To enable the effective extraction of shale gas, accurate prediction of gas recovery from shale formation is needed.

Predicting the gas recovery from shale formations requires a fundamental understanding of the gas transport in these formations. A unique aspect of shale formations is that gas are mostly trapped in ultra-tight rock pores with permeability on the order of nanodarcies.[4, 87] The pore size of these shale matrices spans from a few to several hundred nanometers, [3, 23, 153-156] and the number of nanopores in shale gas reservoirs is much larger than that in conventional gas reservoirs[157]. Because the size of nanopores can become comparable and even smaller than the intrinsic length scale of the gas (i.e., the mean free path) or the length scale of the molecular interactions between gas molecules and pore walls, gas transport in nanopores can deviate from that in macropores. Much insight has been gained on such transport thanks for the extensive research in the past century. [81, 84-86, 158] For example, [153] the nature of gas transport in nanopores depends on the Knudsen number $Kn = \lambda/d$, which is the ratio of the local gas mean free path (λ) to the pore width (d). [24, 63, 159] The gas flow is classified into different regimes including continuum flows ($Kn < 0.01$), slip flows ($0.01 < Kn < 0.1$), transition flows ($0.1 < Kn < 10$), and molecular flows ($Kn > 10$).[24, 64] Except in the continuum flow regime, the no-slip boundary condition and/or the Navier-Stokes equations are not strictly valid. Under these conditions, more advanced models, most of

which based on kinetic theories, have been be used. For example, various slip models have been used to describe the slippage effect on the pore walls.[33, 40, 72-73] In addition to the non-classical flow behaviors, prior research also indicated that the Knudsen diffusion can dominate the transport process in nanopores when the Knudsen number is large because the collisions between gas molecules and pore wall are more frequent than collisions between gas molecules.[18, 160-163] These insights are highly relevant to the gas transport in shale gas formations. For instance, Chen and co-workers[160] constructed the structure of shale formation using with the Markov chain Monte Carlo method and simulated the gas transport in the constructed structures using the Lattice Boltzmann method. Their simulations indicated that gas flow in shale formation differs greatly from the Darcy flow, and the Knudsen diffusion always plays a role in shale gas transport. Finally, when the pore width approaches the length scale of molecular gas-pore wall interactions (usually on the order of a few nanometers), the gas transport within the pore is strongly affected by these interactions.[18, 160]

Building on the fundamental understanding of gas transport in nanopores, many theoretical and simulation studies on the recovery of gas from shale formations have been carried out.[82-83, 87] Much of these works showed that the gas recovery from shale formation is effectively a diffusive process: during the early stage of gas recovery, the cumulative gas production obeys a simple scaling law

$$\mathrm{RF}(t) \approx \alpha t^{1/2} \tag{2-1}$$

$$\mathrm{PR}(t) \approx \beta t^{-1/2} \tag{2-2}$$

where $\mathrm{RF}(t)$ is the recovery fraction of the total trapped gas inside the shale formation recovered between time 0 and t, and $\mathrm{PR}(t)$ is the gas production rate. α and β are pre-factors that depend on the size of pore, the initial pressure of gas inside the pore, etc. During the late stage of gas recovery, the gas production rate decreases exponentially and is often not useful for practical gas recovery operations. While the scaling laws in Equations 2-1 and 2-2 have indeed been observed in some field experiments, other behavior has also been reported. For example, data compiled from the gas production from 25 wells of Barnett shale[90] showed that, during the early

stage of gas production, the decay of the production rate approximately follows a power law with an index -0.4, the accumulative gas recovery thus observes a super-diffusive scaling law $\mathrm{RF}(t) \approx \alpha t^m$ with $\mathrm{m} \approx 0.6$. At present, the physical origins of this super-diffusive scaling is not yet well understood. Nevertheless, some studies have shown that the desorption of gas from pore walls tends to make the decay of gas production rate slower, but its effect on the scaling of gas production was not discussed.[91] It has also been suggested that[163] the ultimate gas recovery will increase significantly as the gas transport of the adsorbed-phase increases.

In this work, we study the gas recovery from single nanopores using molecular dynamic (MD) simulation. In particular, we focus on the scaling laws for gas recovery fraction and the impact of gas-pore wall interactions on gas transport inside the pore and the gas recovery from the pore. Our work is inspired in part by prior studies on shale gas recovery.[81, 83, 87] While these studies have provided powerful insights into the dynamics of shale gas recovery, some important issues were not yet addressed. For example, since they are based on classical kinetic theories, these studies do not clarify the effect of molecular gas-wall interactions. These interactions are expected to be important in pores narrower than a few nanometers, which are abundant in some shale formations.[157] By using MD simulations to study the gas recovery from nanopores, we will explicitly address these issues.

The rest of the paper is organized as follows: In Sec. II, we introduce the MD model for gas recovery from nanopores, the MD simulation method, and our simulation protocol. In Sec III, we present our simulation results on gas recovery, focusing on its qualitative nature (i.e., scaling law of gas recovery) and its quantitative aspect (i.e., rate of gas production and the total diffusion coefficients of gas inside pores). Finally, the conclusions are drawn in Sec. IV.

2.2. MD Simulation Details

Simulation of gas recovery from shale formations appears extremely difficult due to the vastly different scales of pore sizes in shale formations (from a few nanometers to millimeters), the complex structures of these pores, and the complicated connectivity between these pores. Nevertheless, it has been recognized that the overall gas recovery from the formation is limited by

the transport of gas from the narrow pores to large fractures.[87] In addition, prior studies have shown that the essential features of gas recovery is captured well by pore scale modeling utilizing simple pore geometries, e.g. cylindrical or slit pores.[83] In this work, we study the gas recovery from slit-shaped nanopores using MD simulations.

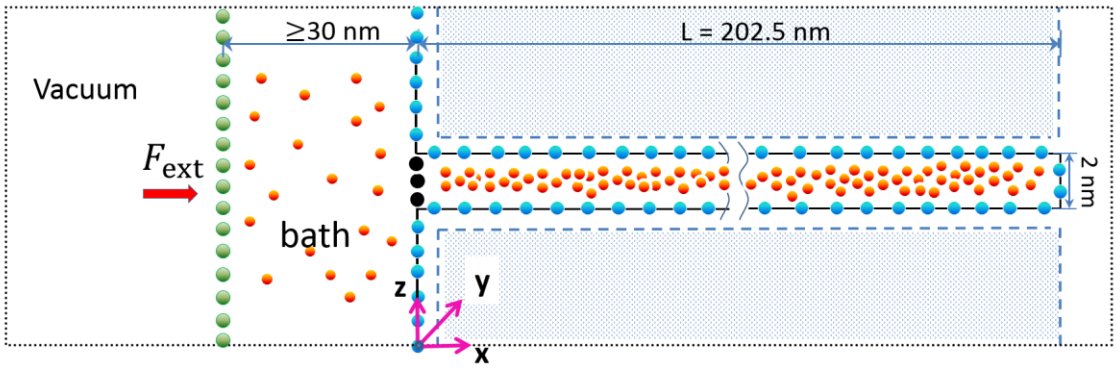

Figure 2-1. A schematic of the nanopore-piston MD system used for studying gas recovery from nanopores. The black dotted line denotes the simulation box, which is periodical in *y*- and *z*-directions. The shaded regions denote the implicit pore walls (see text for details). The black spheres at the pore entrance are "blocker" atoms that are removed during gas recovery simulations.

Figure 2-1 shows a schematic of the MD system. The system features a slit pore, a gas bath, a piston, and the methane gas molecules inside the pore and the gas bath. The right end of the pore is permanently sealed. Initially, the left end of the pore is sealed by fixing some "blocker" atoms at its outlet (the black spheres in Fig. 2-1), and gas inside the pore has higher pressure than in the gas bath. During gas recovery simulations, the left end of the pore is made open by removing those "blocker" atoms. In this setup, the slit pore can be considered as one of the many pores within a shale-rock matrix, while the gas bath can be considered as the secondary fracture in the shale formation, whose permeability is orders of magnitude larger than that of the shale-rock matrix and thus has a nearly constant pressure.[87] The center-to-center width d of the nanopore is 2nm since pores with such small size are abundant in many shale formations.[82-83, 87] Because of the finite size of the methane molecules and the wall atoms, the accessible pore width in MD model W_p is about 1.62 nm. The pore length L is 202.5 nm. The left side of the gas bath is bounded by a piston plate, whose atoms move only in the *x*-direction. To maintain a constant pressure P_{bath} inside the gas

bath, an external force $F_{ext} = P_{bath} L_y L_z$ is applied on the piston plate (L_y and L_z are the plate's width in *y*- and *z*-directions, respectively). The external force is distributed on the atoms of the piston plate such that the plate remains planar. Hereafter, the MD model shown in Fig. 2-1 will be termed nanopore-piston model for brevity.

Table 2-1. Lennard-Jones parameters for interactions between molecules.

	Parameters	
pair	σ (nm)	ϵ/k_B (K)
methane-methane	0.3810	148.1
methane-wall	0.3355	207.2
methane-wall (weak)	0.3355	119.6

The methane molecules are modeled as structure-less, spherical molecules. The interactions between a methane molecule "*f*" and any another atom j in the system are modeled using the Lennard-Jones (LJ) potential

$$\phi_{\mathrm{fj}} = 4\epsilon_{\mathrm{fj}} \left[\left(\frac{\sigma_{\mathrm{fj}}}{\mathrm{r}} \right)^{12} - \left(\frac{\sigma_{\mathrm{fj}}}{\mathrm{r}} \right)^{6} \right] \tag{2-2}$$

where σ_{fj} and ϵ_{fj} are the LJ parameters for the interaction pair, and r is the distance between the two molecules. The piston plate is modeled as a square lattice of carbon atoms (lattice spacing: 0.3 nm). We confirmed that the simulation results are independent of the mass for piston plate atoms. The pore walls are modeled as semi-infinite slabs constructed from a FCC lattice oriented in the <111> direction (following Ref. [81], the lattice constant is taken as 0.54 nm). Explicitly modeling all wall atoms will incur significant computational cost. To overcome this difficulty, only the innermost layer of the wall atoms (i.e., the layer in contact with methane molecules) is explicitly modeled. The wall atoms beneath this layer are treated collectively as an implicit slab, and any methane molecule inside the system interacts with an implicit slab of wall atoms (the shaded region in Fig. 2-1) via an effective interaction described by the LJ 9-3 potential

$$\phi_{\mathrm{f-iw}} = \frac{2}{3}\pi\rho_{\mathrm{w}}\epsilon_{\mathrm{fw}}\sigma_{\mathrm{fw}}^{3} \left[\frac{2}{15} \left(\frac{\sigma_{\mathrm{fw}}}{\mathrm{r}_0} \right)^{9} - \left(\frac{\sigma_{\mathrm{fw}}}{\mathrm{r}_0} \right)^{3} \right] \tag{2-3}$$

where ρ_{w} is the number density of the wall atoms in the implicit slab, ϵ_{fw} and σ_{fw} are the LJ

parameters for interactions between wall atoms and methane molecules, and r_o is the distance between the methane particles and the surface of the implicit slab. The LJ parameters for the methane molecules and the wall atoms are taken from Refs. [164] and [22], respectively, and they are summarized in Table 2-1.

Simulations are performed using the Lammps code[165] with a time step size of 2 fs. Cutoff lengths of 1.2 nm and 1.5 nm are used in the calculation of the methane-methane interactions and the methane-wall interactions, respectively. In each simulation, the number of methane molecules inside the system is kept as constant and the pore walls are fixed in position. The dimensions of the simulation box are kept constant, but the volume of the gas bath increases during gas recovery simulation as its pressure is maintained by the piston wall (note that the simulation box is large enough in the *x*-direction that the piston plate never crosses its left boundary). The temperature of the methane molecules is maintained at 373 K using the Nose-Hoover thermostat. To explore the mechanisms of the gas recovery process, we designed several simulation cases with different pressures in the gas bath ($P_f = 25, 100, 200$ bar) while the initial gas pressure in the nanopore is fixed at $P_o = 250$ bar. These choices of the initial gas pressure in the nanopore, the pressure in the gas bath, and the gas temperature, have been used in recent simulations[82-83, 87] and are relevant to the situations in some shale formations.

Each simulation consists of three steps. In step A, the "blocker" atoms at the pore entrance are removed and F_{ext} on the piston plate is set to a value corresponding to the gas bath pressure P_o. The system is then evolved to equilibrium. In step B, the "blocker" atoms at the pore entrance are reinstated and F_{ext} on the piston plate is set to a value corresponding to the gas bath pressure P_f. The system is then evolved till equilibrium is reached in the gas bath. In step C, the "blocker" atoms at the pore entrance are removed (this moment is defined as t=0) while F_{ext} on the piston plate remains at the value set in the previous step. The system is evolved for 200 ns to study the gas recovery from the nanopore. During each simulation, the density, pressure, and temperature of gas in both the nanopore and the gas bath are computed on-the-fly. Each simulation was repeated three times with different initial configurations to obtain reliable statistics.

2.3. Results and Discussion

A. Qualitative and quantitative aspects of gas recovery

We quantify the recovery of gas from the nanopore by computing a dimensionless recovery fraction (RF) [83]:

$$\mathrm{RF}(\tilde{t}) = n/N \tag{2-4}$$

where n is the cumulative production of mole of gas from the nanopore, and N is the mole of gas in the nanopore at the initial state ($t = 0$). $\tilde{t}$ is a dimensionless time $\tilde{t} = t/t_c$, where t_c is the characteristic time for the gas recovery process. Since the Knudsen diffusion often dominates the transport of gas in the narrow pore considered here and gas recovery from nanopores is often a diffusive process,[83] t_c is chosen as[87]

$$t_c = \frac{4L^2}{D_m^o/K_n^0} \tag{2-5}$$

where L is the pore length. K_n^0 and D_m^o are the Knudsen number and the molecular diffusion coefficient of the gas molecules inside the pore at the initial state, respectively. D_m^o is given by

$$D_m^o = \frac{2}{3}\frac{\sqrt{mk_BT/\pi}}{A\rho_0} \tag{2-6}$$

where m is the mass of a single gas molecule, k_B is the Boltzmann constant, T is the absolute temperature inside the pore, A is the cross-sectional area of the gas molecule, and ρ_0 is the density of pore gas at the pressure and temperature corresponding to those found initially inside the pore. With the choice of pore width and gas in our system ($m = 2.66 \times 10^{-26}$ kg, $A \approx 0.45$ nm^2, W_p =1.62 nm, $P_0 = 250$ bar, $T = 373$ K, $\rho_0 = 168$ kg$\cdot m^{-3}$), $D_m^o = 5.83 \times 10^{-8}$ m^2/s and $K_n^0 = 0.16$.

Figure 2-2a shows the evolution of gas recovery fraction for several cases in which the initial pressure in the pore is fixed at $P_o = 250$ bar while the gas bath pressure P_f varies from 25 to 200 bar. The gas recovery faction increases rapidly during the early stage of operation but increases very slowly for $\tilde{t} \gtrsim 0.1$, similar to what was reported in prior works.[83, 87] Hereafter, we focus on the initial stage of gas recovery since shale gas recovery at the late stage is usually too slow to be practically useful. For $P_f = 200$ bar, $\mathrm{RF}(\tilde{t}) \sim \tilde{t}^{0.5}$ during the early stage of operation, indicating

that the gas recovery is a diffusive process, in good agreement with the previous theories.[83, 87] However, for $P_f = 25$ and 100 bar, $\mathrm{RF}(\tilde{t}) \sim \tilde{t}^{0.58}$, indicating that the gas recovery is no longer a diffusive process. This super-diffusive scaling differs from the prediction by prior theories qualitatively, but it resembles some reported experimental data. Specifically, the average gas production rate obtained from 25 wells by Baihly et al.[90] showed that the production rate decays as $t^{-0.4}$ and the accumulative gas recovery fraction increases on $t^{0.6}$ which is faster than $t^{0.5}$.

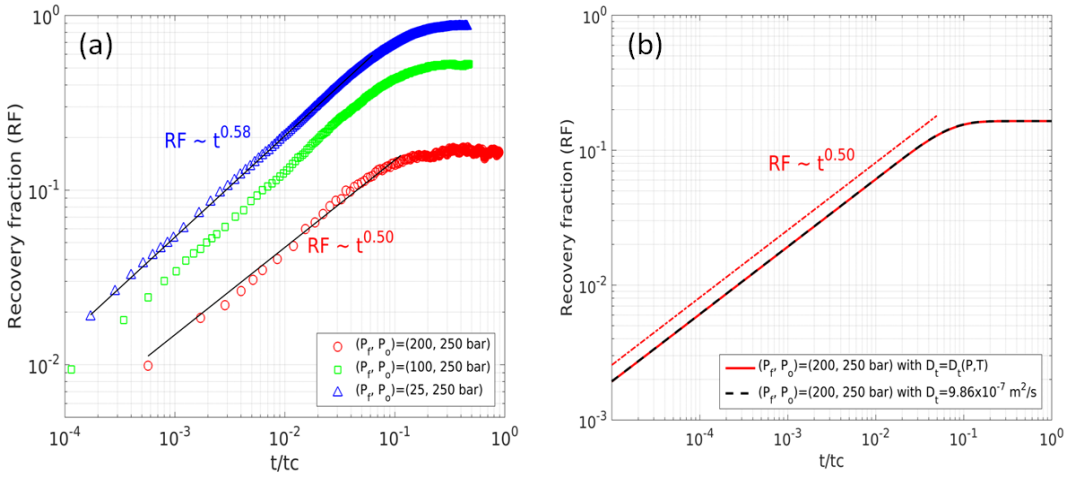

Figure 2-2. (a) The cumulative gas recovery computed by MD simulations for different gas bath pressure (P_f = 25, 100, 200 bar) but the same initial gas pressure inside the pore (P_o = 250 bar). (b) Cumulative recovery fraction calculated by continuum model with total diffusion coefficient taken as a constant or the pressure-dependent form given by Equation 2-8.

Since gas recovery follows the diffusive scaling law predicted by previous theories for $P_f = 200$ bar, we further examine whether the gas recovery under this condition can be italic predicted by prior theories.[87] Following these theories, for the gas recovery from the slit pore shown in Fig. 2-1, the gas density averaged across the pore, ρ, is governed by a one-dimensional model

$$\frac{\partial \rho}{\partial t} + \nabla \cdot \boldsymbol{j} = q \tag{2-7}$$

where ρ is the gas density inside the pore. q is a source term, which is equal to zero when the desorption of gas from pore walls is not considered. $\boldsymbol{j}$ is the gas flux given by $\boldsymbol{j} = -D_t \cdot d\rho/dx$, where D_t is the total diffusion coefficient. Note that isothermal transport is assumed in Equation 2-7. According to the kinetic theory, [87] we have

$$D_t(P,T) = \frac{D_m^o}{Kn}\left(\frac{2}{7}\left(\frac{\rho}{\rho_0 Kn} + 4\right) + \frac{1}{1 + \rho/(\rho_0 Kn)}\right) \tag{2-8}$$

where P is the gas pressure. The first term in the right-hand side is the gas advection including slippage effect and the second term is molecular and Knudsen diffusion under linear diffusion conditions. For the gas recovery simulated in our MD simulations, the initial and boundary conditions of Equation 2-7 are given by

$$\rho(x,0) = \rho_0 \tag{2-9a}$$

$$\rho(0,t) = \rho_f \tag{2-9b}$$

$$\frac{\partial \rho}{\partial t}(L,t) = 0 \tag{2-9c}$$

where ρ_0 is the initial gas density inside the nanopore, and ρ_f is the final density inside the pore. Solving Equations 2-7 - 2-9 leads to a prediction of the gas recovery from the nanopore. During gas recovery operations, the gas density varies along the pore. It follows from Equation 2-8 that the total diffusion coefficient of the gas molecules inside the pore varies temporally and spatially during these operations. Nevertheless, as shown in Fig. 2-2b, the $\mathrm{RF}(t)$ predicted by simulations based on Equation 2-8 agrees well with simulations in which $D_t(\rho)$ is taken to an appropriate constant (hereafter we denote this constant the effective diffusion coefficient D_{eff}; physically, we expect $D_t(P_f) < D_{eff} < D_t(P_0)$). When the total diffusion coefficient is taken as a constant D_{eff}, Equation 2-7 can be solved analytically, [166] and the gas recovery at short time is given by

$$\mathrm{RF}(t) = 2\left(1 - \rho_f/\rho_0\right)\sqrt{\frac{D_{eff}}{\pi L^2}}\,t^{1/2} \tag{2-10}$$

Fitting the gas recovery data from MD simulations under the conditions of $(P_0, P_f) =$ (250 bar, 200 bar) to Equation 2-10, one extracts an effective diffusion coefficient $D_{eff} = 4.62 \times 10^{-7}$ m^2/s, which is smaller than the total diffusion coefficient of gas given by Equation 2-8 at both $P_0 =$ 250 bar (10.20×10^{-7} m^2/s) and $P_f =$ 200 bar (9.27×10^{-7} m^2/s). The smaller D_{eff} extracted from MD data suggests that, for the situation examined here, the gas recovery rate is smaller than that predicted by the classical theories.

The above results indicate that, depending on the operating conditions, the gas recovery from the narrow pore considered here can exhibit qualitatively different behavior (e.g., super-diffusive gas recovery) or quantitatively lower gas recovery rate compared to those predicted by classical theories. These discrepancies can be attributed to the strong adsorption of gas molecules on the solid wall and the gas desorption during gas recovery process, which are often neglected in the classical theories.

B. Importance of gas–wall interactions for gas transport in nanopores

We first study why the gas recovery predicted by MD simulations is slower than that predicted by the classical theory; in another word, why the effective diffusion coefficient of gas molecules in the nanopore extracted from gas recovery data is smaller than the total diffusion coefficient given by Equation 2-8. To this end, we compute the total diffusion coefficient of the gas molecules in nanopore using MD simulations and examine its dependence on the strength of the gas-wall interaction.

To compute the total diffusion coefficient of gas molecules inside the nanopore, we built a separate MD system consisting of a nanopore (it is periodical along the *x*-direction) and the gas molecules inside it (see Fig. 2-3's inset). The width of the pore, the structure of pore walls, and the average gas density inside pore are identical to those in the nanopore-piston system. A constant force of $F_x = 0.238$ pN is applied to each gas molecule in the *x*-direction, and the average velocity of gas molecules is computed. Since the total diffusion coefficient is defined based on the constitutive law of $\boldsymbol{j}_x = -D_t(\rho) \cdot \partial\rho / \partial \mathrm{x}$, it cannot be computed directly from the above force-driven simulations. Instead, it is determined using the Darken equation[167]

$$D_t = \frac{k_B T}{F_x} \langle \mathrm{v}_x \rangle \cdot \left(\frac{\partial \ln f}{\partial \ln \rho} \right)_T = \frac{m}{F_x} \langle \mathrm{v}_x \rangle \cdot \left(\frac{\partial P}{\partial \rho} \right)_T \tag{2-11}$$

where $\langle \mathrm{v}_x \rangle$ is the average velocity of gas molecules in the pore under a driving force of F_x and f is the fugacity. $\left(\frac{\partial P}{\partial \rho} \right)_T$ is computed from the relation between the density and pressure of the gas confined inside the pore, which is determined during step A of the gas recovery simulation for the nanopore-piston system.

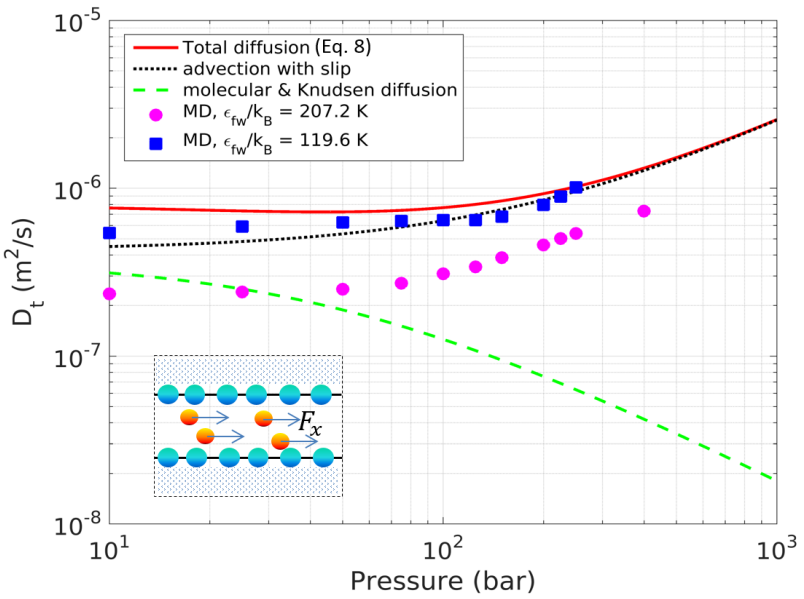

Figure 2-3. Comparison of the total diffusion coefficient of gas inside a 1.62 nm-wide nanopore determined using force-driven MD simulations and kinetic theory model (Eq. 2-8). The inset shows a schematic of the MD system used for studying the gas transport in nanopores.

Figure 2-3 shows the total diffusion coefficient D_t of the gas molecules confined in the pore when they interact with the pore walls with normal strength ($\varepsilon_{fw}/k_B = 207.2$ K) or with reduced strength ($\varepsilon_{sf}/k_B = 119.6$ K). For comparison, the predictions by Equation 2-8 are also shown. In agreement with the kinetic theory, D_t increases with pressure, which can be attributed to the important role of advection in nannopores with high gas density. For gas-wall interactions with normal strength, D_t increases from 4.60×10^{-7} to 5.37×10^{-7} m^2/s as the pressure inside the pore increases from 200 to 250 bar. We note that the D_{eff} determined from the gas recovery simulation operating with $(P_0, P_f) =$ (250 bar, 200 bar) is 4.62×10^{-7} m^2/s, which falls into the above range. Over the entire range of pressure investigated here, D_t computed from MD simulation with normal gas-wall interactions is always smaller than that predicted by Equation 2-8. When the gas-wall interaction is reduced, D_t increases and approaches toward that predicted by the kinetic theories. This suggests that the strong gas-wall interactions cause the slower transport of gas inside the narrow pore compared to the kinetic theory predictions. Strong gas-wall interactions slow down the transport of the gas molecules confined in nanopores because they lead to adsorption of gas molecules on the pore walls. Under a given driving force, the transport of

these adsorbed molecules is slower compared to the free gas in the center of the pore because their friction with pore wall atoms. Such an effect is especially obvious in narrow pores because, the fraction of the wall-adsorbed gas inside a pore increases as the pore size decreases.

C. Importance of gas adsorption/desorption for gas recovery

The strong gas-wall interactions lead to significant adsorption of gas molecules on the pore wall. During a gas recovery operation, the pressure inside the pore drops and those adsorbed gas molecules gradually desorb from the pore wall. Below we show that such gas desorption causes the super-diffusive gas recovery (i.e. $\mathrm{RF}(\tilde{t}) \sim \tilde{t}^{\mathrm{n}}$, with n > 0.5) observed in Fig. 2-2.

The importance of gas desorption in the super-diffusive gas recovery is consistent with the observation that, for a fixed P_0=250 bar in the nanopore, super-diffusive gas recovery is observed only when the gas bath pressure is much lower than P_0, i.e., when $P_f = 25$ or 100 bar but not when $P_f = 200$ bar. This is because gas desorption from pore walls is minor during gas recovery if the initial pressure of gas inside the nanopore is close to the gas bath pressure. Along a similar line, if the adsorption of gas on pore wall is weak at $t = 0$, the subsequent desorption of gas during gas recovery will be weak, and the super-diffusive gas recovery should be suppressed. To test this argument, we perform gas recovery simulations in the nanopore-piston system with reduced gas-wall interactions ($\varepsilon_{fw}/k_B = 119.6$ K), and results are shown in Fig. 2-4. We observe that for $(P_0, P_f) =$ (250 bar, 100 bar), $\mathrm{RF}(\tilde{t}) \sim \tilde{t}^{0.50}$ except at very short time ($\tilde{t} < 2.5 \times 10^{-3}$), while gas recovery operating under the same (P_0, P_f) but with normal gas-wall interaction strength exhibits super-diffusive scaling.

To further ascertain that gas desorption causes the super-diffusive gas recovery shown in Fig. 2-2, we incorporate this effect into the classical gas recovery model and examine the gas recovery computed using the improved model. Specifically, we adopt the method reported by Shabro et al.[91] by setting the source term in Equation 2-7 to be

$$\mathrm{q} = \chi(J_d - J_a) \tag{2-12}$$

where $\chi = 2/W_p$ is the surface to volume ratio of the slit pore, and J_d and J_a are the gas desorption and adsorption fluxes, respectively. J_d is given by

$$J_d = n(P,T)k_d \tag{2-13}$$

where $\mathrm{n}(P,T)$ is the number density of gas adsorbed on pore walls. $k_d = k_0 \exp(-E_d/k_BT)$ is the gas desorption rate (k_0 is a pre-factor and E_d is the desorption energy). The adsorption flux J_a is given by:

$$J_a = (n_\infty - n(P,T))k_aP \tag{2-14}$$

where k_a is the adsorption rate and n_∞ is the number density of the gas adsorption sites on the pore wall.

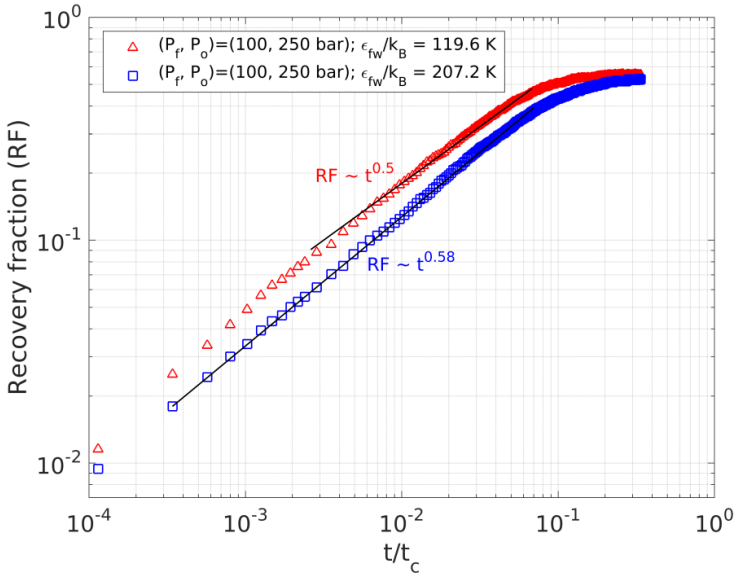

Figure 2-4. MD prediction of the evolution of gas recovery fraction for normal and weak gas-wall interactions (see Table 2-1). The gas bath pressure and initial pressure inside pore are the same, i.e., $(P_0, P_f) =$ (250 bar, 100 bar).

The gas recovery model described by Equations (2-7, 2-9, and 2-12-2-14) is hereafter referred to as the adsorption-desorption-transport (ADT) model. The model input parameters include D_{eff}, k_0, E_d, n_∞, k_a, and k_d. The total gas diffusion coefficient D_{eff} is taken as a constant because the gas recovery from nanopore can be predicted quite well when the spatial and temporal variation of gas diffusion coefficient inside the nanopore during gas recovery is neglected, providing a suitable value of D_{eff} is used (cf. Fig. 2-2b). D_{eff} and k_0 are taken as adjustable parameters in

the ADT model. The desorption energy E_d is determined by computing the depth of the potential well for the gas molecules in the layer next to the wall, and it is found to be 4.36 kJ/mol for the walls in our system. Of the other parameters, n_∞ and k_a/k_d can be obtained by study the thermodynamics of gas adsorption on the pore wall. Specifically, we first divide the gas inside the pore into "free gas" and "adsorbed gas" and compute the isotherm of the adsorbed gas inside the pore. As shown in Fig. 2-5a, to determine the gas adsorption on the pore wall, we partition the pore space into two "wall" zones ($z < 5.9$ Å and $z > 14.1$ Å) and an "interior" zone (5.9 Å $< z <$ 14.1 Å). The adsorbed gas density n is computed using $n = \int_0^{5.9\text{Å}} \rho(z)dz$ for various pore pressure considered. We next fit the computed adsorption-pressure relation to the Langmuir isotherm[168]

$$\mathrm{n}(P,T) = a\frac{bP}{1+bP} \tag{2-15}$$

where a and b are constants. Using Equations 2-13 and 2-14, one readily shows that $a = n_\infty$ and $b = k_a/k_d$. Figure 2-5b shows that the gas adsorption on the pore walls can be described very well by the Langmuir isotherm, with $n_\infty = 4.73$ $\#/nm^2$ and $k_a/k_d = 0.02$ MPa^{-1}.

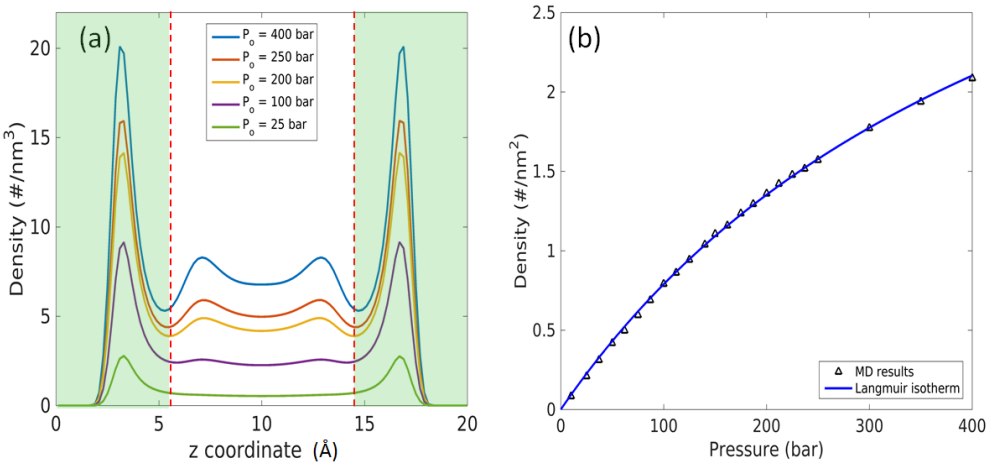

Figure 5. (a) Gas density profile across the nanopore computed using MD simulations under different pore pressure. Gas within the shaded regions is considered as adsorbed gas. (b) The gas adsorption isotherm determined using the gas density data in (a) and its fitting to the Langmuir isotherm.

With the above parameters, we solved the ADT model to predict the gas recovery from nanopore studied in our MD simulations with $(p_0, p_f) = (250, 25$ bar$)$, and compare the result

with that computed using MD simulations. Figure 2-6 shows that, with a pre-factor for desorption rate of $k_0 = 0.84 \times 10^{13}\ s^{-1}$ and an effective diffusion coefficient of $D_{eff}^{25-250} = 4.06 \times 10^{-7}\ m/s^2$, the gas recovery predicted by the continuum model agrees quite well with our MD results. We note that the desorption pre-factor k_0 used here is within the range used in previous studies.[169] In addition, the effective diffusion coefficient used above also falls into the range of D_t computed through separate MD simulations with normal gas-wall interaction strength ($\varepsilon_{fw}/k_B = 207.2$ K) ($D_t = 2.41 \sim 5.37 \times 10^{-7}\ m/s^2$ from 25 to 250 bar, see Fig. 2-3).

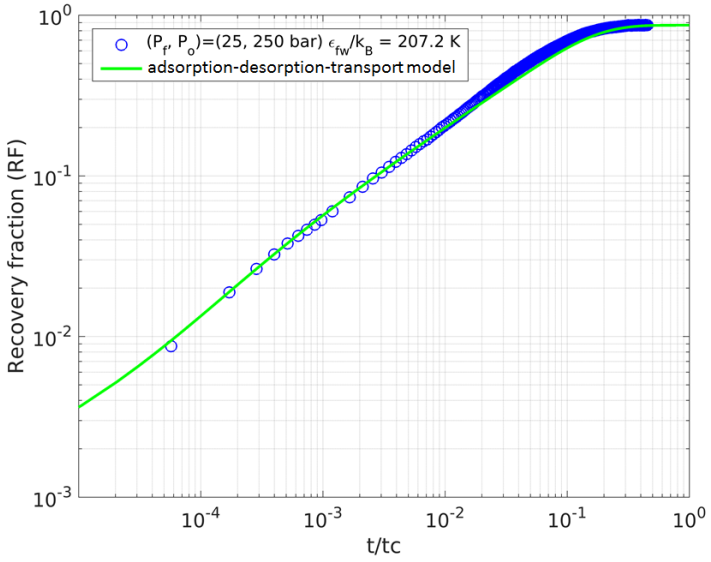

Figure 2-6. Comparison of the gas recovery fraction predicted by MD simulations and the adsorption-desorption- transport model for $(P_0, P_f) =$ (250, 25 bar).

The good agreement between the ADT model and the MD simulations confirms that the significant gas desorption impacts near the wall surface is responsible for the super-diffusive gas recovery observed in MD simulations. In addition, while the ADT model described above has been used in previous studies [91, 163] for shale gas recovery, it has not been validated quantitatively using more fundamental methods (e.g., MD simulations) to our knowledge. Given that the ADT model divides the gas within a nanopore into free gas and adsorbed gas (with no lateral mobility but finite exchange with free gas) while even adsorbed gas molecules have finite lateral mobility, it is not clear *a priori* that the ADT model can predict the gas recovery accurately. This is especially true in narrow pores in which the division between the free gas and adsorbed gas is less sharp compared

to wide pores. The results shown in Fig. 2-6 thus provides support for the effectiveness of the ADT model despite its rather drastic simplification of the real gas adsorption, desorption and transport processes in nanopores.

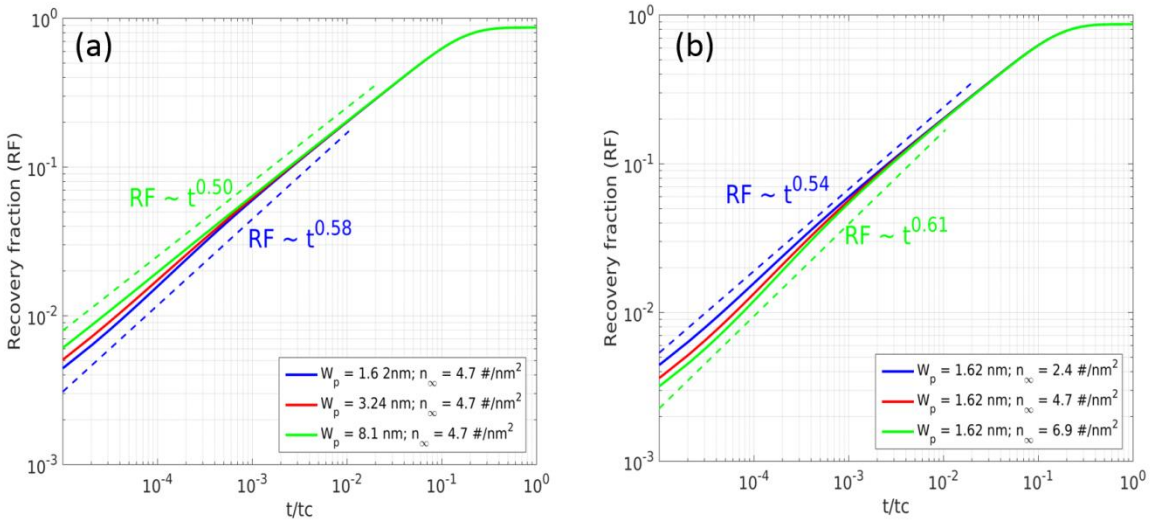

Figure 2-7. Effects of pore width W_p (a) and maximal gas adsorption capacity on pore walls n_∞ (b) on the gas recovery from nanopores predicted using the adsorption-desorption model for $(P_0, P_f) =$ (250 bar, 25 bar).

Because the ADT model can capture the gas recovery behavior from nanopores well, we next use it to examine how the scaling law of gas recovery is affected by the properties of the nanopores. In particular, we vary the pore width W_p and the maximal adsorption capacity of the pore wall n_∞ to study how they affect the deviation of gas recovery from the classical diffusive behavior. Figure 2-7a shows that, for a fixed $n_\infty = 4.73\ \#/\text{nm}^2$, the gas recovery becomes more "diffusive" as the pore width increases and the classical diffusive scaling is recovered in pores with width of 8.1 nm. Figure 2-7b shows that, for a fixed $W_p =$ 1.62 nm, gas recovery still exhibits notable super-diffusive behavior even when the maximal gas adsorption capacity reduces to $n_\infty = 2.4\ \#/\text{nm}^2$. Together, these results suggest that the super-diffusive gas recovery found in this work will likely occur in shale formations with pore size up to ~5 nm.

2.4. Conclusions

We perform MD simulation to investigate the gas extraction from single nanopores. The cumulative gas recovery and the effective diffusion coefficients for gas transport inside pores are

studied. The results showed that, in very narrow pores, the strong gas-wall interactions can change the gas recovery behavior both quantitatively and qualitatively. These interactions slow down the gas recovery rate because they cause the total diffusion coefficients of the gas inside nanopores to be smaller than those predicted by kinetic theories. Additionally, these interactions lead to significant adsorption of gas molecules on the pore walls and cause a super-diffusive behavior RF$\sim\tilde{t}^{0.58}$. We show that, even in very narrow pores, the super-diffusive gas recovery behavior can be captured quantitatively using the coupled adsorption-desorption-transport model despite its rather drastic simplification of the physical processes during gas recovery. Parametric studies using the coupled adsorption-desorption-transport suggest that, at the single-pore level, super-diffusive gas recovery occurs in pore size up to ~5 nm in diameter if the difference between the initial pressure inside nanopore and the pressure in the large gas bath (or equivalently large fractures) is large. These results suggest that the super-diffusive gas recovery behavior reported for some shale gas wells may be due to the adsorption-desorption effects, although a definitive conclusion requires simulations taking into account factors such as the polydispersity of pore size and the complex connectivity between pores in realistic shale formations.

Chapter 3. Multicomponent Shale Gas Recovery from Single Nanopores

Disclosure:

This work has been published by the American Chemical Society: Wu, H.; He, Y.; Qiao, R., Recovery of Multicomponent Shale Gas from Single Nanopores. *Energy & Fuels* 2017, *31*, 7932-7940.

3.1 Introduction

Natural gas production from shale formations has received extensive attention recently and can potentially lead to a new global energy source. The U.S. Energy Information Administration shows that shale gas provides the largest source of the growth in U.S. natural gas supply during the past decade, and its share is expected to grow continuously in the future.[26] The composition of shale gas varies with among shale reservoirs. While methane is always the most abundant component in shale gas, hydrocarbons with higher molecular weight are also present. In particular, ethane is the usually the second primary component in shale gas and can account for up to 15 vol% of the recovered gas.[170] The effective extraction of these hydrocarbons, which are much more valuable than methane, is of great interest for the shale gas industry.

A distinguishing feature of shale formations is that, while it typically features pores ranging from sub-nanometer to millimeters in size, its porosity is often dominated by nanopores smaller than 10-100 nanometers. As such, much of the gas is stored inside narrow nanopores as adsorbed gas and free gas.[157, 171] Based on extensive research on transport of fluids in nanopores[5, 172], e.g., layering of fluids on pore walls modulates their transport through narrow pores[61, 173-175], one can expect that the thermodynamic and hydrodynamic properties of gas inside such pores, which govern the extraction of gases from the pores, can be quite different from those of bulk gas.[176] Tremendous progress has been made for understanding the adsorption and transport of single-component gas (usually methane) inside nanopores[53, 57] in the past decade, but those of multicomponent gas mixtures are much less well understood. Among the available studies,[47-52] much attention is focused on the competitive adsorption of $CH_4/N_2/CO_2$ gas species in shales,

which plays an important role for enhancing shale gas recovery. However, a general understanding of the adsorption and transport of multicomponent shale gas under realistic reservoir condition (e.g., considering CH_4/C_2H_6 mixture) is still limited.

Research on the adsorption and transport of multicomponent shale gas in nanopores can potentially benefit from the extensive work on the thermodynamic and transport properties of multicomponent gas in other industrial applications.[52, 54-60] For example, previous studies have attempted to predicted the multicomponent adsorption via the Extend Langmuir (EL) model[55] and the Ideal Adsorbed Solution (IAS) model.[54, 59] In addition to these theoretical models, previous simulations also indicated that there exits complex competition between adsorbed species. [52, 56, 58]

We are interested in understanding the storage of multicomponent gas mixtures in shale formations and their recovery during gas extraction using numerical simulation. Simulation of shale gas storage and recovery in shale formations appears extremely difficult because of the vast spectrum of pore sizes involved, the diverse surface chemistry of the pores, and the complicated connectivity between nanopores. Nevertheless, prior studies[87, 177] show that the overall shale gas recovery is mainly controlled by the transport of gas from the narrow pores to wide secondary fractures, and the essential features of shale gas adsorption and transport inside nanopores can be well captured by pore scale modeling with simple pore geometries, e.g. cylindrical or slit pores.[87] In this work, we study the adsorption of CH_4/C_2H_6 gas mixtures in single nanopores and their subsequent recovery from these pores using molecular dynamic (MD) simulation. In particular, we focus on the competitive adsorption effect of the two gases in the adsorbed phase of the nanopore and the gas recovery behavior of each species from the nanopore. Our work is inspired in part by prior studies on recovery of multicomponent shale gas, [49, 56, 58, 178] which have provided many useful insights into the dynamic behavior of gas adsorption and transport with mixtures components. Nevertheless, some important issues have not been addressed yet in these studies. For example, the competitive adsorption of CH_4/C_2H_6 gas inside nanopores and its impacts on shale gas storage is still not well understood, and a molecular view of the recovery of multicomponent gas mixture from nanopores is not yet available. By using MD simulations to

study the gas recovery from nanopores, we will explicitly address these issues.

The rest of the paper is organized as follows: In Sec. II, we introduce the model and methods for simulations of the equilibrium isotherm and dynamic extraction of CH_4/C_2H_6 mixture from single nanopores. In Sec III, we present our simulation results on adsorption isotherm (with a focus on the competition between methane and ethane in the adsorbed phase) and the recovery characteristics of the two gases (with a focus on the recovery of ethane). Finally, conclusions are drawn in Sec. IV.

3.2. MD Simulation Details

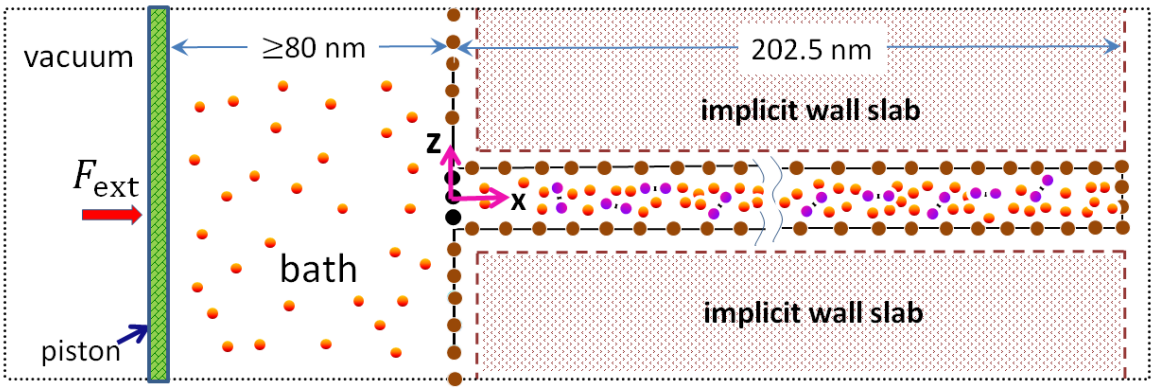

Figure 3-1. A schematic of the MD system used for studying the adsorption of $CH_4 - C_2H_6$ gas mixture in a single nanopore and their recovery from the pore. The simulation box is denoted using the black dotted lines. The brown spheres denote the explicitly modeled wall atoms and the shaded regions denote the implicit pore walls (see text for details). The black spheres at the pore mouth are the "blocker" atoms. The orange spheres and the purple dumbbells are the CH_4 and C_2H_6 molecules, respectively. The green plate at the left end side denotes the piston used to control the pressure in the gas bath.

Figure 3-1 shows a schematic of the MD system. The system features a slit pore, a gas bath with a constant pressure, a piston, and the shale gas molecules inside the pore and the gas bath. The system is periodical in the *y*- and *z*- directions. The pore's right end is permanently sealed. The center-to-center widths d of the investigated nanopores are 2nm and 4nm since pores with such small size are abundant in shale formations.[83, 87] Due to the finite size of the methane molecules and the wall atoms, the accessible pore width in MD model W_p is about 1.62 nm and 3.62 nm, respectively. The pore length L is 202.5 nm. The left side of the gas bath is bounded by

a piston plate (green plate in Fig. 3-1), whose atoms move only in the *x*-direction. The constant gas pressure inside the gas bath is maintained by applying an external force $F_{ext} = L_y L_z P_{bath}$ on the piston plate (L_y =13.5 nm and L_z=12.8 nm are the plate's width in *y*- and *z*-directions, respectively; P_{bath} is the desired gas pressure inside the bath). All forces experienced by the piston plate are averaged and re-distributed evenly on the atoms of the piston plate such that the plate remains planar.

Two types of simulations are performed: adsorption isotherm simulations and gas recovery simulations. For the adsorption isotherm simulations, initially methane and ethane molecules are placed in the gas bath and equilibrated; the pore is empty and sealed by "blocker" atoms at its mouth (see the black spheres in Fig. 3-1). During the simulations, the pore is made open by removing the "blocker" atoms at its mouth, thus gas molecules move from the gas bath into the nanopore till a new equilibrium is reached. By using a gas bath that is sufficiently large and adjusting the number of gas molecules inside the gas bath by trial and error, the mole fraction of methane and ethane molecules inside the gas bath have been controlled to be 4:1 within a few percent. The amount of methane and ethane adsorbed inside the nanopore from the equilibrium run is used to determine the gas reserve inside the nanopore

Table 3-1. Lennard-Jones parameters for interactions between atoms.

	Parameters	
atom pair	σ (nm)	ϵ/k_B (K)
methane-methane	0.3730	148.0
ethane-ethane[a]	0.3750	98.0
methane-wall	0.3315	207.2
ethane-wall[b]	0.3325	168.6

[a] this is for the interactions between the CH_3 sites of two different ethane molecules.

[b] this is for the interactions between wall atom and one CH_3 site of an ethane molecule.

For the gas recovery simulations, the system is setup with pure methane in the gas bath and gas mixtures (CH_4 : C_2H_6 molar ratio is 4:1) in the pore. Initially, the left end of the pore is sealed, and the system is equilibrated with higher pressure ($P_0 = 200$ bar) in the pore and lower pressure in the bath ($P_{bath} = 20$ bar). At *t* = 0, the "blocker" atoms at the left end of the pore are

removed. Because the initial pressure inside the pore is higher than that in the gas bath, gas recovery is initiated.

Methane and ethane molecules are modeled using the TraPPE Force Field.[179] Briefly, methane molecules are modeled as structureless, spherical molecules; ethane molecules are modeled as dumbbell-shaped molecules featuring two united atoms each representing one CH_3 site, and the two united atoms are separated by a bond length of 1.54Å. While it is desirable to explicitly resolve all hydrogen atoms in the methane and ethane molecules, prior works show that the united atom approach taken here already allows accurate prediction of gas adsorption on planar walls well with lower computational cost.[6,20] The inter-molecular interactions between an atom "*m*" and another atom "*j*" are modeled using the Lennard-Jones (LJ) potential,

$$\phi_{mj} = 4\epsilon_{mj}\left[\left(\frac{\sigma_{mj}}{r}\right)^{12} - \left(\frac{\sigma_{mj}}{r}\right)^{6}\right] \tag{3-1}$$

where σ_{mj} and ϵ_{mj} are the LJ parameters for the pair (*m*,*j*), and r is the distance between the two atoms. The piston plate is modeled as a square lattice of carbon atoms (lattice spacing: 0.3 nm). We confirmed that the simulation results are independent of the piston mass. Following Ref. [81], the pore walls are modeled as semi-infinite slabs constructed from a FCC lattice oriented in the <111> direction and the lattice constant is 0.54 nm. To avoid the significant computational cost of explicitly simulating all wall atoms, only the innermost layer of the wall atoms (i.e., the layer in contact with gas molecules) is explicitly modeled. The wall atoms beneath this layer are treated collectively as an implicit slab, and gas molecules inside the system interact with the implicit slab of wall atoms (the shaded region in Fig. 3-1) via an effective interaction described by the LJ 9-3 potential,

$$\phi_{m-iw} = \frac{2}{3}\pi\rho_w\epsilon_{mw}\sigma_{mw}^3\left[\frac{2}{15}\left(\frac{\sigma_{mw}}{r_0}\right)^{9} - \left(\frac{\sigma_{mw}}{r_0}\right)^{3}\right] \tag{3-2}$$

where ρ_{w} is the number density of the wall atoms in the implicit slab, ϵ_{mw} and σ_{mw} are the LJ parameters for the interactions between the wall atoms and the gas molecules, and r_0 is the closest distance between a gas particle and the surface of the implicit slab. The LJ parameters for the gas molecules and the wall atoms are summarized in Table 3-1.[179] The interaction parameters for the

methane-ethane (i.e., CH_4-CH_3) pair are determined from those for the CH_4-CH_4 and CH_3-CH_3 pairs using the Lorentz-Berthelot combination rule. With the structure of the wall and the LJ parameters for gas-wall interactions chosen here, the adsorption behavior of pure methane is found to be similar to those found in prior studies of methane adsorption in organic shale pores.[180]

Simulations are performed using the Lammps code[165] with a time step size of 2 fs. The cut-off lengths for gas-gas interactions and gas-wall interactions are 1.4 nm and 1.5 nm, respectively. For each simulation, the volume of the system and the number of gas molecules inside the entire system are both kept constant. The pore wall atoms are fixed. We emphasize that, although the dimensions of the simulation box are fixed, the volume of the gas bath can change during gas recovery and adsorption isotherm simulations because its pressure is maintained by the piston (the simulation box is large enough in the *x*-direction so that the piston plate never protrudes out of the left boundary of the simulation box). The temperature of the gas molecules is maintained at 353 K using the Nose-Hoover thermostat. In each simulation, the density, pressure, and temperature of gas in both the nanopore and the gas bath are computed on-the-fly. Each simulation is repeated three times with different initial configurations to obtain reliable statistics. Specifically, before gas recovery simulations start, the gas molecules in the bath and in the pore are separated by the blocker atoms (see Fig. 3-1) and the system is equilibrated for 2 ns. The configurations of the system at three time instants (1.0, 1.5, and 2.0 ns) of the equilibrium run are saved. We then perform three gas recovery simulations, in which the initial configuration is taken from those three equilibrium configurations just saved.

3.3. Results and Discussions

B. Methane and ethane storage in nanopores

As customary in studying material adsorption in porous materials, the storage of a gas species *i* inside a nanopore is measured per unit surface area of the pore using

$$n_{i,tot} = \frac{1}{2}\int_{-W/2}^{W/2} \rho_i(z)dz \tag{3-3}$$

where $\rho_i(z)$ is the density of the species across the pore, W is the pore width, and the factor 1/2

appears because each slit pore has two walls. Because the gas density is strongly inhomogeneous across nanopores (see, for example, the methane density profile in the inset of Fig. 3-2b), researchers often partition shale gas inside nanopores into adsorbed gas and free gas.[157, 171] To delineate these two forms of gas and to help understand the storage of methane-ethane mixture in nanopores, we first examine the storage of pure methane and pure ethane in nanopores. Here, gas molecules in the density peaks next to the wall (shaded region in the inset of Fig. 3-2b, hereafter referred to as the adsorption layer) are taken as adsorbed gas and said to belong to the adsorbed phase. The rest of the gas molecules inside the pore are considered as free gas and said to belong to the free phase. The adsorbed gas of species i is quantified using

$$n_{i,ads} = \int_{-W/2}^{-W/2+\delta} \rho_i(z)dz = \int_{W/2-\delta}^{W/2} \rho_i(z)dz \tag{3-4}$$

δ is the thickness of adsorbed gas layer in z-direction (taken as 4 Å here). In principle, δ may vary with pore size and pressure. However, examination of the gas density profiles in different pores at various pressures (see Fig. SA3 in the Supporting Information) showed that, within the parameter space explored here, such variation is small and can be safely neglected.

Figure 3-2a shows the isotherm of the methane storage inside a 2.0nm-wide pore and its contribution by free and adsorbed gases. We observe that the adsorbed methane accounts for more than 60% of all methane stored inside 2.0nm-wide pores in the range of pressure investigated here, and their contribution increases as the pressure decreases. Similar trends are observed when pure ethane is stored inside the same pore (see Fig. SA1). However, as shown in Fig. 3-2b, at the same pressure, the amount of ethane adsorbed on the walls of 2nm-wide pores is larger than that of methane. This is expected because the adsorption of gas molecules on pore walls is driven by the attractive van der Waals forces between the gas molecules and the wall, and ethane molecules, which contain two CH_3 sites, have stronger van der Waals interactions with wall than methane molecules. The stronger adsorption of ethane on pore walls is also observed in the 4nm-wide pores (see Fig. SA2).

Next, we examine the gas storage inside nanopores in equilibrium with bath of binary methane-ethane mixtures. In all cases studied, the mole fraction of ethane in the gas bath is set to

0.2±0.01. Figure 3-3a compares the storage of methane and ethane in a 2nm-wide pore as a function of pressure (data for methane-ethane mixture storage in 4nm-wide pore exhibits similar trend and is shown in Fig. SA4). The nonlinear increase of the gas storage with pressure, a signature of significant contribution of surface adsorption to gas storage, is similar to that of pure gas. Figure 3-3b shows that the molecular fraction of ethane inside the nanopores is higher than that in the bath, i.e., ethane is enriched in the pores. The enrichment is stronger in the 2nm-wide pores. Figure 3-3c further shows that, in both 2nm- and 4nm-wide pores, the enrichment of ethane inside pores is mainly caused by its enrichment in the wall-adsorbed phase. The latter is expected based on the results shown in Fig. 3-2b. However, Fig. 3-3c shows that the ethane enrichment decrease as the pressure increases beyond ~100 bar. This means that the adsorption of methane on the pore walls becomes more competitive than ethane as pressure increases beyond 100bar. To better understand this result, we examine the isotherm for the concurrent adsorption of methane and ethane on the walls of 2nm-wide pore.

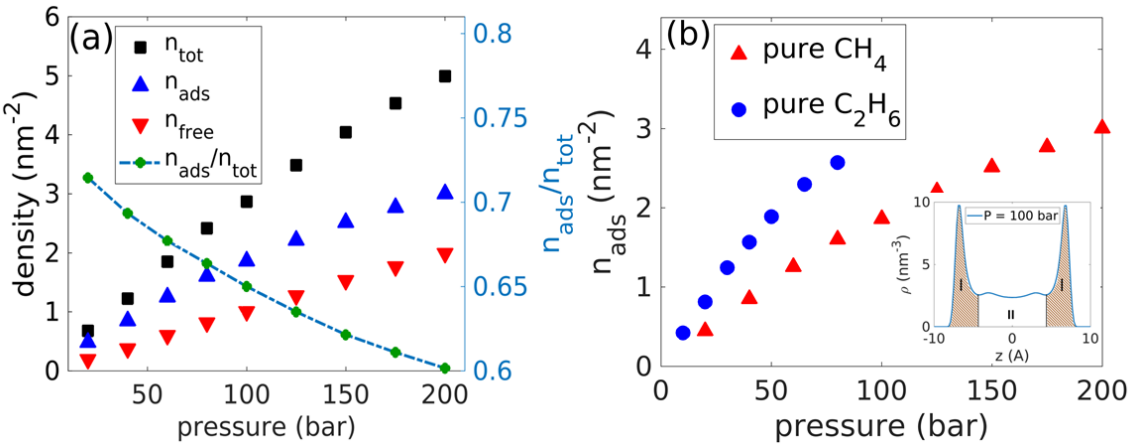

Figure 3-2. (a) Isotherm of the storage of methane in 2nm-wide nanopores in equilibrium with a pure methane bath and the contribution by the adsorbed and free gas to the total gas storage. (b) Isotherms of methane and ethane adsorbed on the walls of a 2nm-wide nanopore when the pore is in equilibrium with pure methane and ethane gas bath. The inset is the density profile of methane across a 2nm-wide slit pore when the pore pressure is 100bar. Gas molecules in the region I (region II) are taken as the adsorbed (free) gas.

Figure 3-4 shows the isotherms for the adsorption of methane and ethane on the walls of 2.0nm-wide pores. At P≲100bar, the adsorption of methane and ethane increases rapidly with

pressure. As pressure increases further, the increase of the adsorption of both methane and ethane slows down. However, the slowdown is much more distinct for ethane and the adsorption of ethane reaches a plateau at P~150bar. In another word, ethane becomes less competitive in adsorbing on the pore walls than methane, and this leads to the reduced ethane enrichment at elevated pressure (see Fig. 3-3c). The less competitive adsorption of ethane than methane at high pressure can be understood as follows. At low to moderate pressure, the gas adsorption layer on the wall is loosely packed, and gas-wall interactions play the most important role in determining gas adsorption. Since ethane molecules interact more strongly with the pore walls than the methane molecules, they outcompete methane in adsorption on pore walls. As the pressure increases, the gas adsorption layer becomes more densely packed and the entropic effects become more important. Since ethane molecules are larger than methane molecules, their entropy is lower than that of the methane molecules at elevated pressure. Therefore, ethane molecules become less competitive in adsorption on pore walls than the methane molecules. We note that a similar effect has been predicted theoretically in prior studies of binary adsorption of methane-ethane in zeolites.[181-183]

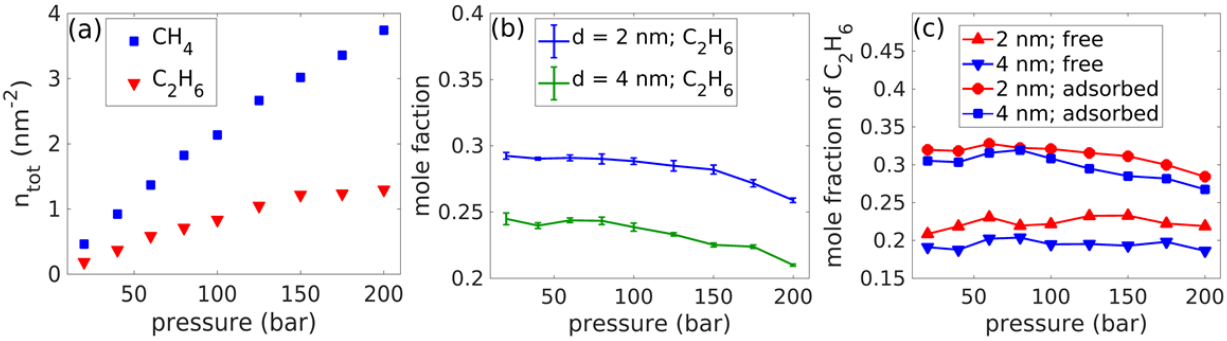

Figure 3-3. (a) Isotherm of the methane and ethane storage inside a 2.0nm-wide pore. (b) Mole fraction of ethane inside pores with different widths. (c) Mole fraction of free and wall-adsorbed ethane inside pores with different widths. All pores are in equilibrium with a bath of binary methane-ethane mixture (mole fraction of ethane is 0.2±0.01).

We next investigate to what extent the isotherms computed using MD simulations can be predicted using existing theories. Among the available theories on multicomponent gas adsorption, the ideal adsorbed solution (IAS) theory[59] is popular due to its simplicity and good predicting power. The theory introduces a two dimensional confinement pressure termed spreading pressure

in the adsorbed gas phase. By assuming that the different gas components are mixed ideally in the adsorbed gas phase and the area and enthalpy changes during mixing of different gas species are negligible for the same spreading pressure, the adsorption isotherm of different gas species (e.g., methane and ethane) on a solid substrate can be predicted using the isotherms for the adsorption of pure gases (e.g., methane and ethane) as input. Using the adsorption isotherm of pure methane and ethane shown in Fig. 3-2, the adsorption of methane and ethane on the wall of a 2nm-wide pore in equilibrium with a binary mixture of methane and ethane (ethane mole fraction: 0.2) is determined using the IAS theory. Figure 3-4 shows that the IAS theory captures key feature of the isotherm of mixture adsorption on pore walls. Most importantly, the theory predicts that, as pressure increases beyond ~100bar, the increase of the adsorption of ethane slows down more significantly than that of methane, i.e., ethane becomes less competitive in surface adsorption than methane. Nevertheless, the theory systematically overestimates the adsorption of both methane and ethane, especially at high pressure. Similar discrepancy between the IAS predictions and experimentally measured isotherms has been found in some prior work, [14] and it is likely caused by the non-ideality of mixing methane and ethane in the adsorption layer on the pore walls.

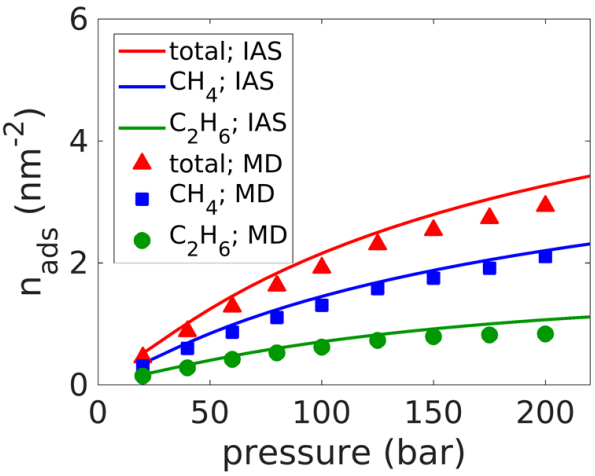

Figure 3-4. Isotherm of methane and ethane adsorption on walls of a 2.0nm-wide pore predicted by MD simulations and the IAS theory. The pore is in equilibrium with a bath of binary methane-ethane mixture (mole fraction of ethane is 0.2±0.01). Results for methane/ethane adsorption on walls of 4.0nm-wide pore are similar and shown in Fig. SA4.

C. Methane and ethane recovery from nanopores

In this section, we study the recovery of gas from a single nanopore ($d = 2$ or 4 nm) to a large gas bath. As detailed in Section 2, initially, each nanopore is filled with a methane/ethane mixture (CH_4:C_2H_6 molar ratio: 4:1; total pressure: 200 bar) and the gas bath contains pure methane. The pressure in the gas bath is maintained at 20 bar throughout the simulation. At $t = 0$, the blocker atoms at the pore mouth are removed to initiate the gas recovery.

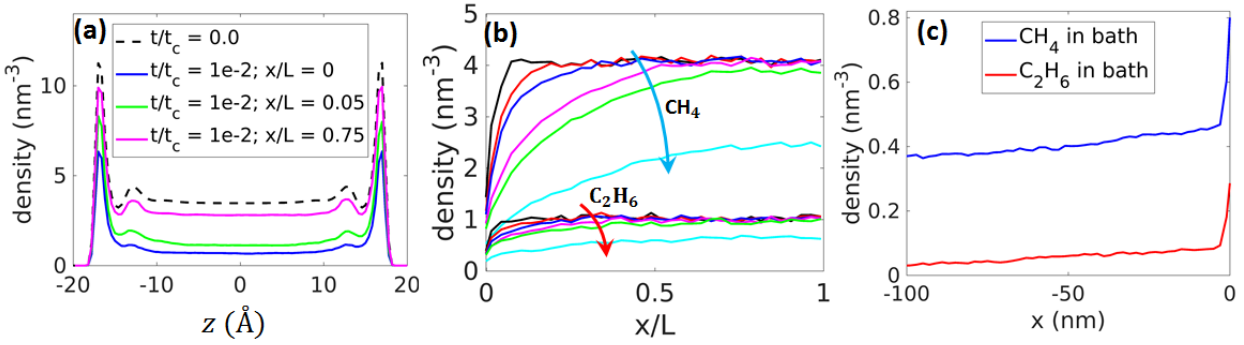

Figure 3-5. Evolution of the density profiles of methane and ethane molecules inside the 4nm-wide pore and the gas bath during gas recovery. **(a)** Methane density profile across the nanopore at difference positions along the pore ($x/L = 0, 0.05, 0.75$) at $t/t_c = 0.01$. The dash line denotes the initial methane density across the pore. **(b)** The cross-section averaged density of methane and ethane along the pore length at $t/t_c = 10^{-4}, 5\times10^{-4}, 10^{-3}, 5\times10^{-3}, 10^{-2}, 5\times10^{-2}$. The arrows in the figure indicate the direction of increasing time. **(c)** Density of methane and ethane along the x-direction in the gas bath at time $t/t_c = 0.01$ (x=0 corresponds to the position of the pore mouth, see Fig. 3-1).

To gain generalized insight into the kinetics of gas recovery using our MD simulations, we nondimensionalize the time using a characteristic time t_c. Since gas recovery from nanopore is generally considered as a diffusive process, following previous works,[87, 7] t_c is chosen as

$$t_c = \frac{4L^2}{D_m^0/\mathrm{Kn}^0} \tag{3-5}$$

where L is the nanopore length, D_m^0 and Kn^0 are the reference molecular diffusion coefficient and Knudsen number inside the pore prior to gas recovery. D_m^0 and Kn^0 depend on the molecular properties of the gas species and the pore size. For nanopores filled with multiple gas species, it is difficult to define D_m^0 and Kn^0, and thus t_c, uniquely. Here, we use the molecular properties of methane (cross-sectional area: 0.45 nm^2) to calculate the characteristic time t_c since methane

dominates the gas storage inside the nanopores. With the temperature and initial pressure inside the nanopores, we obtain a D_m^0 of 5.53×10^{-8}m/s^2. Furthermore, we compute a mean free path corresponding to the initial pressure inside the pore (λ_0) and a mean free path corresponding to the pressure inside the gas bath (λ_f). λ_0 is more relevant to the gas transport in the pore interior and at early stage of gas recovery; λ_f is more relevant to gas transport near pore mouth. It is found that λ_0 =0.26 nm and λ_f =1.9 nm. Using the accessible width of the pore as the characteristic length scale, the corresponding Knudsen numbers are found to be $\mathrm{Kn}^0 = 0.16$ and $\mathrm{Kn}^f = 1.19$ for the 2nm-wide pore. Note that the accessible width of a pore with a width of 2.0nm (4.0nm) measured between the center planes of the atoms in its two walls is 1.6nm (3.6nm) because the methane molecule has a diameter of ~0.4nm.

We first examine the qualitative features of gas recovery process. Figure 3-5a shows the methane density profile across the 4nm-wide pore at different *x*-positions at $t/t_c = 0.01$. We observe that, both near the pore wall and in the central portion of the pore, methane density decreases from their initial values (marked using a dashed line in Fig. 3-5a), which suggests that the adsorbed gas and the free gas are recovered from the pore concurrently. The drop of the gas densities from their initial values becomes less significant as we move from the pore mouth toward the pore interior, which is indicative of the diffusive nature of the gas recovery process. Figure 3-5b shows the evolution of the cross-section averaged density profiles of methane and ethane along the pore length. After the gas recovery starts, the methane and ethane densities near the pore mouth drops quickly because of the gas exchange between the gas bath (where the gas density is lower) and the gas at the pore mouth. As gas recovery proceeds, gas density in the pore interior drops and clear diffusion front moving toward the pore interior is observed. The diffusion front reaches the pore's sealed end at t/t_c~0.01, and the density of both methane and ethane decreases along the entire pore length after that. We note that the gas density at the pore mouth gradually decreases as gas recovery proceeds, which suggests that the gas exchange between the gas bath and pore mouth has a finite resistance. Such a resistance also manifests as concentration polarization in the gas bath. Indeed, as shown in Fig. 3-5c, the densities of methane and ethane are non-uniform inside

the gas bath, and a diffusion boundary layer in which the gas density varies sharply is visible near the pore mouth. The strength of concentration polarization, as indicated by the drop of gas density across the diffusion boundary layer, is comparable for methane and ethane. Because concentration polarization reduces the driving force for the gas transport from the pore to the gas bath, it slows down gas recovery. The nominal driving force for recovery of methane is larger than that for ethane because the maximal difference of the density of methane inside the pore and the gas bath (~4 nm^{-3} according to Fig. 3-5b and 3-5c) is larger than that for ethane (~1 nm^{-3} according to Fig. 3-5b and 5c). Because the strength of concentration polarization is similar for methane and ethane, concentration polarization likely slows down the recovery of ethane more notably than that of methane.

Next, we investigated the production rate of methane and ethane during gas recovery process. The production rate of a gas species *i* is quantified as its flux out of a nanopore using

$$Q_i(\tilde{t}) = -dN_i/d\tilde{t} \tag{3-6}$$

where $\tilde{t} = t/t_c$ is the dimensionless time and N_i is the number of species *i*'s molecules inside the pore. The fluxes of methane and ethane from the 2nm- and 4nm-wide pores are shown in Fig. 3-6a and 3-6b, respectively. At earlier time ($\tilde{t} < 0.01$), the flux of both methane and ethane follow a superdiffusive scaling law $Q(\tilde{t}) \sim \tilde{t}^{-\alpha}$ with $0.4 < \alpha < 0.5$, which differs from the $Q(\tilde{t}) \sim \tilde{t}^{-0.5}$ for purely diffusive gas recovery. Similar deviation from the purely diffusive scaling law has been reported for the recovery of pure gas from nanopores, and is caused by the delayed removal of gas molecules adsorbed on the pore walls.[7] At $\tilde{t} \gtrsim 0.04$ ($\tilde{t} \gtrsim 0.01$), the production of methane and ethane from the 2nm-wide (4nm-wide) pore starts to deviate from the power law scaling behavior. This is consistent with the fact that the diffusion front reaches the pore's sealed end at these times (see Fig. 3-5b). Figure 3-6c shows the evolution of the ethane and methane flux ratio (Q_e/Q_m) with time. We observe that, during the entire gas recovery operation, Q_e/Q_m is mostly in the range of 0.19-0.22, which is very close to the initial ethane-to-methane ratio of 0.25 inside the nanopores. This result is somewhat surprising. Specifically, because of the stronger attraction of ethane to the pore walls (and consequently stronger adsorption on the pore walls) than methane (see Fig. 3-3), the mobility

of ethane molecules confined inside narrow pores is much smaller than that of the methane molecules. For example, we compute the total diffusion coefficient of methane (ethane) molecules confined inside 2nm- and 4nm-wide pores filled with pure methane (ethane) at various pressure (see Supporting Information), and find that the mean total diffusion coefficient of ethane molecules confined in these pores is 4-5 times smaller than that of the methane molecules at the same pressure (see Fig. SA5). In addition, as discussed earlier, the concentration polarization near the pore mouth likely slows down the recovery of the ethane more significantly than that of the methane. Therefore, one could have expected Q_e/Q_m to be much smaller than 0.25 during gas recovery. Below we seek to understand why this is not what we observed in the direct simulation of gas recovery from nanopores.

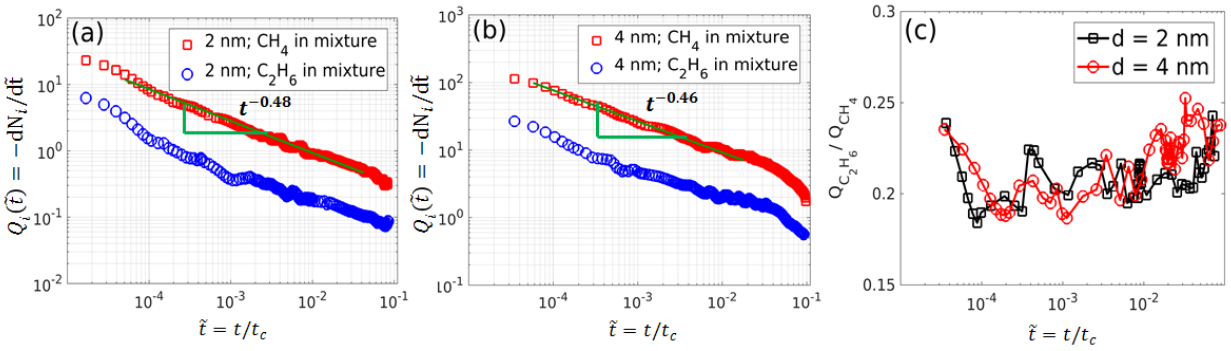

Figure 3-6. (**a-b**) The evolution of the production rate of the methane and ethane compared with the pure methane from the 2nm-wide pore (a) and the 4nm-wide pore (b). (c) The evolution of the ratio of the methane and ethane flux out of the pore.

In principle, the composition of the gas recovered from pores filled with multiple gas species can be understood using several theoretical methods for describing multicomponent fluid transport, e.g., the Onsager formulism based on non-equilibrium thermodynamics and the Maxwell–Stefan formulism.[184] Here we adopt the Onsager formulism, in which the transport of two species *i* and *j* in a mixture can be described using

$$J_i = -L_{ii}\nabla\mu_i - L_{ij}\nabla\mu_j \tag{3-7}$$

where J_i and μ_i are the flux and chemical potential of species *i*, respectively. L_{ij} is the Onsager coefficient, which depends on the concentration and distribution of species *i* and *j* in the mixture,

as well as the interactions between gas species.[178] Rigorous calculations of the gas fluxes from nanopores initially filled with multicomponent gas is complicated by the fact that, because the gas density and composition evolves both temporally and spatially inside the pore, the Onsager coefficients also vary temporally and spatially inside the pore and thus difficult to compute accurately. Here we combine scale analysis and MD simulations to obtain a semi-quantitative understanding of the composition of gas fluxes from pores during gas recovery operations.

Since the IAS theory predicts the isotherm of gas storage inside nanopores quite well (see Fig. 3-4), it is reasonable to assume that methane and ethane are mixed ideally inside the pore. We thus approximate the fugacity of gas species *i* using its partial pressure and write the chemical potential of species *i* as $\mu_i - \mu_{i,0} = k_B T \ln(P_i/P_{i,0})$, where $\mu_{i,0}$ and $P_{i,0}$ are the chemical potential and partial pressure of species *i* at a reference state, respectively. $k_B T$ is the thermal energy. Further assuming that each gas inside the pore behaves ideally, the gradient of the chemical potential of the species *i* can now be written as $\nabla\mu_i = \rho_i^{-1}\nabla P_i$, where ρ_i is the density of the species *i*. The flux of gas species *i* out of the nanopore, $Q_i(t)$, thus reads

$$Q_i(t) = A\left(-L_{ii}\rho_i^{-1}\nabla P_i - L_{ij}\rho_j^{-1}\nabla \mathrm{P}_j\right)\Big|_m \tag{3-8}$$

where the subscript *m* indicates that the terms in the bracket should be evaluated at the pore mouth, and A is the cross-section area of the pore. Because the gas recovery rate drops sharply at late stage and is thus of limited interest for practical gas recovery operations, we focus on the early stage of the gas recovery operation when the diffusion front has not reached the pore's sealed end (i.e., $t/t_c < \sim 0.01$ in the pore considered here, see Fig. 3-5 and 3-6). In this case, the scale of ∇P_i is given by

$$\nabla P_i \sim \left(P_{i,df} - P_{i,m}\right)/l_{df}(t) \tag{3-9}$$

where $P_{i,df}$ and $P_{i,m}$ are the partial pressure of species *i* at the diffusion front inside the pore and at the pore mouth, respectively (hereafter we denote methane and ethane as species "1" and "2", respectively). $l_{df}(t)$ is the distance from the pore mouth to the diffusion front at time *t*. While ρ_i varies along the pore length during gas recovery, one can reasonably approximate it as the average of the gas density at the pore mouth and the diffusion front. Since gas is assumed to behave

ideally, it follows that $\rho_i \sim (k_B T)^{-1}\left(P_{i,df} + P_{i,m}\right)/2$. L_{ij} depends on the composition of gas species and their interactions inside the nanopores. As a first attempt, we approximate L_{ij} in Equ. 3-8 using the Onsager coefficients computed for methane and ethane mixture inside the 2nm- and 4nm-wide pores at the beginning of gas recovery when the pressure is 200 bar (see below), and denote L_{ij} thus obtained as L_{ij}^0. With the above assumptions and approximations, the flux of a gas species *i* at the pore mouth can be estimated as

$$Q_i \sim -\frac{2k_B T}{l_{df}(t)}\left(\frac{P_{i,df}-P_{i,m}}{P_{i,df}+P_{i,m}} L_{ii}^0 + \frac{P_{j,df}-P_{j,m}}{P_{j,df}+P_{j,m}} L_{ij}^0\right) \tag{3-10}$$

The ratio of the ethane and methane flux from the nanopore can then be estimated as

$$Q_e/Q_m \sim \left(\frac{L_{21}^0}{L_{11}^0} + \frac{L_{22}^0}{L_{11}^0} G_{21}\right) / \left(1 + \frac{L_{12}^0}{L_{11}^0} G_{21}\right) \tag{3-11a}$$

$$G_{21} = \left(P_{2,df} - P_{2,m}\right)\left(P_{1,df} + P_{1,m}\right)/\left(P_{1,df} - P_{1,m}\right)\left(P_{2,df} + P_{2,m}\right) \tag{3-11b}$$

Taking advantage of the fact that gas bath contains mostly methane throughout the gas recovery operation and neglecting the concentration polarization at pore mouth, we have $P_{1,m} \approx P_{bath} = 20$ bar and $P_{2,m} \approx 0$. Since the gas density at the diffusion front differs little from the gas densities inside the nanopore prior to gas recovery operations and we assume that methane and ethane are mixed ideally, we take $P_{1,df} \approx P_0 x_1^0$ and $P_{2,df} \approx P_0 x_2^0$, where P_0 is the pressure inside nanopore $t = 0$. Because the mole ratio of ethane and methane inside the nanopore is 1:4 at $t = 0$, we have $x_1^0 = 0.8$ and $x_2^0 = 0.2$. It follows that $G_{21} \approx 1.29$.

To estimate Q_e/Q_m using Equ. 3-11, we next determine L_{11}^0, L_{21}^0, L_{12}^0, and L_{22}^0 using the method introduced by previous researchers.[178, 185] For a binary mixture of species *i* and *j* confined in a pore that is periodical in its length direction, one applies a constant force F_j on each molecule of species *j* in direction along the pore. By measuring the resulting fluxes of these species, L_{ij} can be computed using

$$L_{ij} = J_i/F_j = \quad \bar{\rho}_i < v_i > /F_j \tag{3-12}$$

where J_i, $\bar{\rho}_i$, and $< v_i >$ are the flux, average density, and average velocity of species *i* in the pore. Here, we build nanopores with geometry and wall properties identical to those of the pores used in our gas recovery simulations except that these pores are periodical in their length direction.

The pores are filled with ethane-methane mixture (mole ratio is 1:4) to a pressure of 200bar. To determine L_{11}^0 and L_{21}^0, we apply a constant force F_1 on each methane molecule inside the pore and compute the resulting fluxes of the methane and ethane molecules, L_{11}^0, and L_{21}^0 using Equ. 3-12. Here we use $F_1 = 0.143\text{pN}$, and we also find that increasing or decreasing F_1 by 3 times does not affect the computed L_{11}^0 and L_{21}^0 within statistical error. L_{22}^0 and L_{12}^0 are computed using similar methods.

Table 3-2 shows the computed Onsager coefficients. We observe that L_{12}^0 is equal to L_{21}^0 within statistical uncertainty, thus satisfying the Onsager reciprocity. The relative magnitude of the diagonal and off-diagonal terms depend only weakly on the pore size. The diagonal term L_{22}^0 is much smaller than L_{11}^0, and this is consistent with the facts that there are much more methane molecules in the pore than ethane molecules and the total diffusion coefficient of methane molecules confined in nanopores is larger than that of the ethane molecules (see Fig. SA5). Importantly, we observe that the cross-correlation L_{12}^0 is even higher than the L_{22}^0 term. This indicates that the interactions between methane and ethane play a critical role in the transport of ethane in the nanopores.

Table 3-2. The Onsager coefficients for the transport of methane (species 1) and ethane (species 2) inside slit nanopores with different widths.*

	L_{11}^0/L_{11}^0	L_{21}^0/L_{11}^0	L_{12}^0/L_{11}^0	L_{22}^0/L_{11}^0
d = 2 nm	1	0.19 ± 0.01	0.18 ± 0.01	0.08 ± 0.01
d = 4 nm	1	0.21 ± 0.01	0.20 ± 0.01	0.06 ± 0.01

* The nanopores are filled with methane and ethane with mole ratio of 1:4 and pressure of 200bar.

Using the Onsager coefficients shown in Table 3-2 and Equ. 3-11, the ratios of the ethane and methane fluxes (Q_e/Q_m) during gas recovery from 2nm- and 4nm-wide pores are estimated to be 0.219 and 0.220, respectively. These estimations are in good agreement with the results shown in Fig. 3-6c. The relatively large Q_e/Q_m originates from the facts that L_{21}^0 is not much smaller than L_{11}^0 and L_{12}^0 is larger than L_{22}^0, both of which reflect the effective coupling between the transport of ethane and methane inside nanopores. In the above analysis, the effect of concentration polarization at the pore mouth is neglected. When such effect is taken into account by using the

gas composition measured at pore mouth at representative time (e.g., at $t/t_c = 0.01$, see Fig. 3-5c) to determine $P_{1,m}$ and $P_{2,m}$ in Equ. 3-11b, the Q_e/Q_m predicted using Equ. 3-11a only decreases slightly (see Supporting Information).

3.4. Conclusions

We use MD simulations to investigate the adsorption of binary mixture of methane and ethane in nanopores and the gas recovery from these pores to low pressure gas bath. Calculation of the binary adsorption isotherm of nanopores in equilibrium with bulk methane-ethane mixture shows that while both methane and ethane are stored as free gas and adsorbed gas inside the nanopores, the adsorption of ethane on the wall is stronger than methane. The stronger adsorption of ethane on pore walls compared to methane leads to an enrichment of ethane inside nanopores. Such an enrichment is more pronounced in narrow pores but is weakened as the pressure increases due to entropic effects. During gas recovery operations, free and adsorbed gas are extracted concurrently from the nanopores, and noticeable concentration polarization, occurs near the pore mouth. Nevertheless, the production rates of both gases approximately follows the square root scaling law before the diffusion front reaches the sealed end of the nanopores. The ratio of the production rate of ethane and methane from the pores is only slightly smaller than their initial mole ratio inside the pores, which is attributed to the effective coupling of the transport of methane and ethane inside nanopores.

Our simulation results suggest that the storage of binary gas in narrow nanopores is affected strongly by the adsorption of different gas molecules on the wall, which depends on both the pore pressure and the nature of gas molecules. Since molecular simulations are computationally too costly for determining such adsorption in practical applications, molecular theories are needed. In this regard, we show that the classical IAS theory can predict the essential trends of binary gas adsorption on the pore walls, although it tends to overestimate the gas adsorption. Our simulations revealed that the recovery of binary gas mixture from single, narrow nanopores to gas baths is approximately a diffusive process and the coupling between the transport of gas species inside the nanopores plays an essential role in determining the composition of the recovered gas. These

results lend support to the existing theories for gas recovery from nanopores and point to the need to develop effective models for predicting the coupling of the transport of different gas species confined inside nanopores.

Molecular simulations of gas recovery are limited to systems with pores many orders of magnitude shorter than in real shale formations, and this necessarily introduces some undesirable features such as extremely large pressure gradient along pore length and from the pore opening to the gas bath during gas recovery. Nevertheless, the fact that the present and our earlier MD simulations[7] capture the scaling law of gas recovery rate reported in field studies and continuum simulations[87, 90] suggests that these undesired features do not incur significant artifacts into the simulations. Therefore, MD simulations not only can be used to understand the transport and adsorption properties of gases in nanopores as demonstrated extensively in the past years, but can also be used as a powerful tool for exploring the essential physics of gas recovery process. In this study, we focus on the recovery of CH_4-C_2H_6 mixture from nanopores. The same method can be used for understanding the recovery of other gas mixtures. For example, since some shale formations contains a greater share of CO_2 than C_2H_6, it would be interesting to study the recovery of CH_4-CO_2 mixtures. The same method can also be used for studying the enhanced recovery of methane by injection of CO_2 in shale formations.

Supporting Information

All supporting information cited in this chapter is located in Appendix A.

Chapter 4. Drying of Nanoporous Filtration Cakes: A Pore Network Study

Disclosure:

This work has been published by the Elsevier: Wu, H.; Fang, C.; Wu, R.; Qiao, R., Drying of Porous Media by Concurrent Drainage and Evaporation: A Pore Network Modeling Study. *Int. J. Heat Mass Tran.* 2020, *152*, 118718.

4.1. Introduction

Drying of porous media including building materials and pharmaceuticals is important in engineering applications ranging from material manufacturing and oil extraction to soil remediation.[1, 13, 92, 2] Although many technologies including thermal drying and infrared radiation drying have been developed,[186] they often suffer from limitations such as high energy cost, low throughput, *etc*. Hence, there is a long-standing need to improve existing methods or to develop new technologies to overcome these limitations. Addressing this need through trial-and-error experiments is often costly and ineffective, and numerical modeling can be helpful. Modeling of the drying of porous media, however, is challenging because coupled multiphase heat and mass transfer at scales from nanometer to centimeters must be simulated.[11-12]

To tackle the multi-faceted (multiphase, multiscale, and multiphysics) drying processes in porous media, many numerical models have been developed. These models can be loosely classified into two categories: macrohomogeneous models and pore scale models. In macro-homogeneous models, the porous media are treated as a continuum with volume-averaged or homogenized properties. These models can deal with large scale problems easily.[9, 93] However, because the microstructures of porous media and the physical processes in them (e.g., viscous fingering and corner flows) are not resolved but modeled heuristically using sub-models, they offer limited insight into the fundamental physics of the drying process and often lack predictive power in novel situations. In pore scale models, the heat and mass transfer in the microscale geometry of porous media are considered. In some models, the original heat and mass transfer equations such as the Navier-Stokes equation are solved in porous media.[95,96,187] In other models,[106] porous media

are represented using various building blocks and the transport processes are modeled based on rules derived from fundamental heat and mass transfer laws. Amount these models, pore network models have received much attention because they offer a good balance between capturing pore scale physics (hence drying) and being computationally efficient.

In pore network models, the pore space is simplified as discrete elements consisting of pore bodies interconnected with each other by pore throats. The first pore network model for studying drying was built in 1954[106] and many improvements have been made since then.[10, 101, 107-110] Key to these models is the consideration of fluid and mass transfer at the pore scale and in the interconnected pore systems. For example, the transport of vapor obeys convection-diffusion equations and the continuity equation is applied to the liquid phase and non-condensable gas phase;[10, 101] the pattern of receding liquid-vapor interfaces due to evaporation has been described using the invasion percolation (IP) model.[188-189] While existing pore network models have been successful in analyzing many porous media drying problems, new problems with unique features not explored previously continue to appear and the existing models need to be extended to study these problems. In this work, we extend pore network models to study the drying of porous media with nanoscale pores assisted by purge gas flowing through them.

Figure 4-1 show a schematic of the drying problem studied here, which is part of the solvent recovery step in the dewatering-by-displacement technology.[190] A bed of particles with diameter often smaller than 2 μm is initially saturated with a volatile solvent (e.g., pentane) and a purge gas is driven through the particle bed to remove the solvent. At the beginning, the injected purge gas penetrates into the particle bed to displace the liquid solvent, just as in the conventional drainage process. Eventually, the purge gas breaks through the particle bed and gas transport pathways are formed across the porous matrix. After this, evaporation occurs within the porous matrix and the vaporized solvent is “flushed” downstream by the purge gas. Meanwhile, the purge gas continues to drive the remaining liquids out of the porous matrix. The overall drying process is similar to the operation of filter dryers and the drying of packed beds.[120-121] Although the extensive pore network modeling in the literature has led to useful fundamental understanding of porous media drying,

they offer limited insights for this drying problem because of its several unique features:

1. Drying is assisted by the flow of purge gas *through* the porous media, which differs from the widely studied scenario where drying is assisted by gas streams flowing *over* the porous media's surface;
2. The drainage of liquid solvents and evaporation of solvents can occur concurrently in the porous media and become tightly coupled;
3. Because of the small particle size, the pores between them can have diameter of a few hundred nanometers.[191] Therefore, the gas slippage and Knudsen effects, rarely considered in previous drying research, can no longer be neglected in the gas transport process;
4. The liquid solvent is highly volatile and their vapor pressure can be comparable to that of the purge gas. The multicomponent gas transport behavior can involve strong couplings between the purge gas and vaporized solvents, which cannot be described well using the classical convection-diffusion equations.

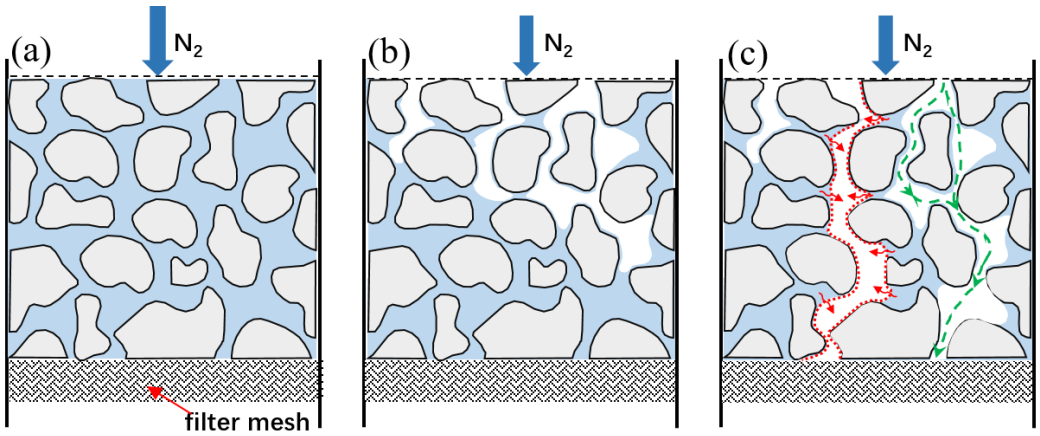

Figure 4-1. *Drying of a porous medium with purge gas flowing through it*. **(a)** The porous medium, a particle bed, is initially saturated with a volatile liquid solvent. **(b)** The purge gas displaces liquid solvents from the porous medium, and the solvent evaporation is negligible. **(c)** The purge gas breaks through the porous medium and evaporation of the liquid solvents becomes important; drainage and evaporation can occur concurrently and become strongly coupled.

In this work, we study the drying of porous media assisted by purge gas flowing *through* them using a pore network model. The rest of the manuscript is structured as follows: In Section II, we detail our model that accounts for the concurrent the drainage and evaporation processes during drying and the other unique features mentioned above. In Section III, we present the simulation

results for drying, reporting the evolution of the drying rate and discussing the couplings between the drainage and evaporation effects. Finally, conclusions are presented in Section IV.

4.2. Model Formulation

To study the drying problem shown in Fig. 4-1, we assume that the porous media is initially ($t = 0$) fully saturated with a volatile liquid solvent. The solvent liquids have a zero contact angle on solid surfaces and the purge gas has negligible solubility in the solvent liquids. Below, we first present the setup of the pore network, then discuss the physical and numerical models, and finally present the numerical algorithm.

A. Pore network

Since we focus on the coupling between drainage and evaporation, which is the most unique aspect of the drying problem shown in Fig. 4-1, the geometry of the porous media is simplified as a two-dimensional (2D) rectangular block represented by a pore network.[192-193] The pore network lattice consists of pore bodies connected to their four neighbors via pore throats (see Fig. 4-2a). The upstream (downstream) boundary of the pore network is connected with an upstream (downstream) reservoir. Periodic boundary conditions are applied on the left and right boundaries. The pore bodies have cubic shape and the pore throats have circular cross-sections. A schematic of two pore bodies connected via a pore throat is presented in Fig. 4-2b. Following previous work,[192-193] the sizes of pore bodies and throats follow a truncated log-normal distribution:

$$f(r_i) = \frac{\sqrt{2}\exp(-0.5(\frac{\ln\frac{r_i}{r_m}}{\sigma}))}{\sqrt{\pi\sigma^2}\cdot r_i(\mathrm{erf}\left(\ln\frac{r_{max}}{r_m}/\sqrt{2\sigma^2}\right)-\mathrm{erf}\left(\ln\frac{r_{min}}{r_m}/\sqrt{2\sigma^2}\right))} \tag{4-1}$$

where r_i is the radius of the inscribed sphere of a cubic pore body *i* (see Fig. 4-2b); in other words, the length of the pore body is $2r_i$. σ is the standard deviation. r_m, r_{min} and r_{max} are the mean of the inscribed sphere radius, the lower bound and upper bound of the truncation, respectively. The spacing between adjacent layers in the pore network in the *x*- and *y*-directions are denoted as $\Delta S_{x,i}$ and $\Delta S_{y,i}$, respectively:

$$\Delta S_{x,i} = a_x \max\{r(i,j) + r(i+1,j), \text{ for } j = 1{:}n_y\}, \ \ i = 1{:}n_x \tag{4-2a}$$

$$\Delta S_{y,j} = a_y \max\{r(i,j) + r(i,j+1), \text{ for } i = 1{:}n_x\}, \ \ j = 1{:}n_y \tag{4-2b}$$

where α_x and α_y are prefactors set to $a_x = a_y = 1.2$ and n_x (n_y) is the number of pore bodies in the x- (y-) direction. The length of the pore throats is then determined via

$$l_{x,i} = \Delta S_{x,i} - (r(i,j) + r(i+1,j)) \quad \text{for } j = 1{:}n_y,\ i = 1{:}n_x \tag{4-3a}$$

$$l_{y,j} = \Delta S_{x,j} - (r(i,j) + r(i,j+1)) \quad \text{for } i = 1{:}n_x,\ j = 1{:}n_y \tag{4-3b}$$

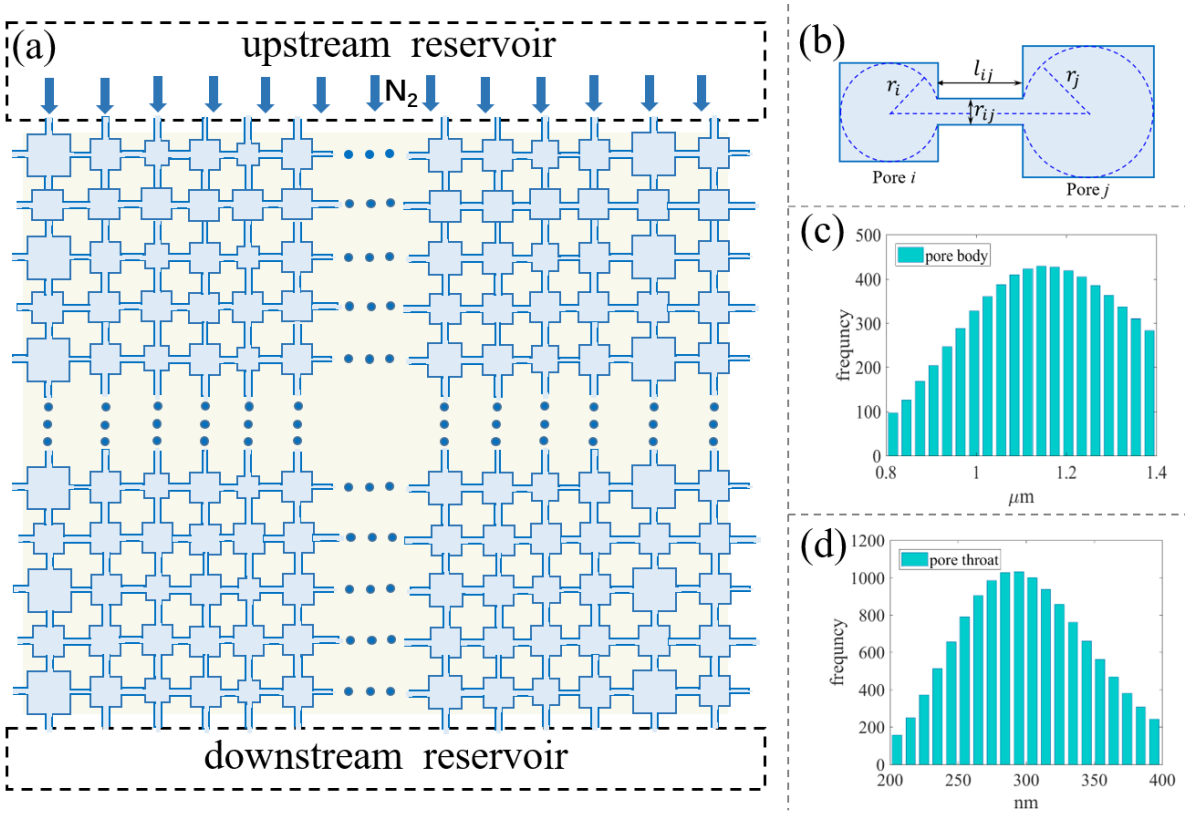

Figure 4-2. *The pore network model*. **(a)** A schematic of the pore network. **(b)** A sketch of two pore bodies connected by a pore throat. **(c)** The pore body size distribution. **(d)** The pore throat size distribution.

B. Physical and numerical models

Below, we present the models for the drying of porous media assisted by purge gas flowing through them. Key assumptions for model development, the models for liquid and vapor transport, the models for liquid vaporization, initial and boundary conditions, rules for events in the pore network model, and the computational algorithms are discussed.

B.1 Assumptions

The following assumptions are made in our pore network model:

1. Pore bodies have finite volume but zero hydraulic resistance for liquid and gas transport.
2. Pore throats have negligible volume and their hydraulic resistance corresponds to fully developed flows in ducts with the same size. A pore throat has only two states: filled with liquid or filled with gas. Meniscus is not tracked inside pore throats and the time required for filling/emptying a single pore throat by liquid/gas is negligible.
3. Liquid solvents are incompressible and the solid phase is considered as a rigid body.
4. For the gas and liquid flows in pore throats, the inertia effects are negligible.
5. Gravity effects are negligible because the drying process occurs at microscale.
6. Drying occurs under isothermal conditions.
7. The vaporization of liquid solvents at the corner of a pore body can occur if more than two throats connected with that pore body is occupied by the gas phase. For pore bodies in which vaporization does not occur, the density of the solvent vapor is set to its saturation density at the same temperature.

These assumptions have been adopted extensively in prior pore network simulations of porous media drying because they allow capture the essential physics of the drying process to be modeled with modest cost and computer memory.[10, 114, 189, 192, 194]

B.2 Transport model

We adopt the two-pressure algorithm[192, 195-196] for solving the pressure field for both liquid and gas phases. Hereafter, variables corresponding to the liquid and gas phases are identified using superscripts "*l*" and "*g*", respectively. Because the gas phase is generally a two-component mixture of the purge gas (species 1) and the solvent vapor (species 2), variables corresponding these components are identified using superscripts "*g1*" and "*g2*", respectively. The local capillary pressures in the pore bodies are defined and approximated as[192, 196]

$$P_i^c(S_i^l) = P_i^g - P_i^l = \frac{2\gamma}{r_i(1-\exp(-6.83S_i^l))} \tag{4-4}$$

where P_i^g P_i^l, P_i^c and S_i^l are the gas phase pressure, liquid phase pressure, capillary pressure, and the saturation of the liquid phase in the pore body *i*. γ is the interfacial tension.

Volume balance: A volumetric flux is assigned to a pore throat *ij* for both gas and liquid

phases and a volume balance is required for each pore body *i*:

$$\sum_{j=1}^{N_i}\left(Q_{ij}^{l}+Q_{ij}^{g}\right)=0 \tag{4-5}$$

where N_i is the number of pore bodies connected to the pore *i*, Q_{ij}^{l} (Q_{ij}^{g}) is the volumetric flux of liquid (gas) through the pore throats *ij*.

Liquid transport: The volumetric flux of the liquid phase through a pore throat *ij* is

$$Q_{ij}^{l}=-K_{ij}^{l}\left(P_i^{l}-P_j^{l}\right) \tag{4-6}$$

where P_i^{l} is the liquid pressure of pore body *i* and, K_{ij}^{l} is the conductivity of the pore throats filled with liquid. $K_{ij}^{l}=\frac{\pi r_{ij}^{4}}{8\mu_l l_{ij}}$ since we assume a Hagen-Poiseuille flow in pore throats. μ_l, l_{ij}, r_{ij} are the liquid viscosity, pore throat length, and pore throat radius, respectively.

Gas transport: The transport of gas through pore throats is complicated: because the partial pressure of the solvent vapor is comparable to that of the purge gas, a multicomponent transport model is required. Here, we adopt the dusty gas model (DGM), which have been widely used for multicomponent mass transfer in nanopores. The transport of an ideal mixture of *d* gas species through a pore with a radius of r_{ij} can be described using[20-21, 197-198]

$$\sum_{\substack{n=1\\n\neq m}}^{d}\frac{x_nJ_m-x_mJ_n}{\rho_tD_{mn}}+\frac{J_m}{\rho_tD_{mk}}=-\frac{1}{p}\frac{dp_m}{dz}-\frac{x_mk_p}{\mu_{mix}D_{mk}}\frac{dp}{dz}\quad(m=1,2,\dots d) \tag{4-7}$$

where J_m, ρ_m, and x_m are the molar flux, averaged molar density, and molar ratio of specie *m,* respectively. p is the pressure of the d-component gas mixture and p_m is the partial pressure of a specie *m*. ρ_t is the total molar density, k_p is the effective permeability, μ_{mix} is the mixture viscosity, D_{mn} is the mutual diffusivity between species *m* and *n*. $D_{mk}=\frac{2r_{ij}}{3}\sqrt{\frac{8R_gT}{\pi M_m}}$ is the Knudsen diffusivity of species m (M_m is the molar mass, R_g is the ideal gas constant and T is the temperature). When applied to a binary mixture of purge gas (species 1) and solvent vapor (species 2) that behaves ideally, the molar flux of each gas species can be reorganized and simplified as

$$J_1=\rho_1u_1=-\left(\left(\frac{(x_1D_{2k}D_{1k}+D_{12}D_{1k})/R_gT}{x_2D_{1k}+x_1D_{2k}+D_{12}}+\frac{k_p\rho_1}{\mu_{mix}}\right)\frac{dp_1}{dz}+\left(\frac{x_1D_{2k}D_{1k}/R_gT}{x_2D_{1k}+x_1D_{2k}+D_{12}}+\frac{k_p\rho_1}{\mu_{mix}}\right)\frac{dp_2}{dz}\right) \tag{4-8a}$$

$$J_2=\rho_2u_2=-\left(\left(\frac{x_2D_{2k}D_{1k}/R_gT}{x_2D_{1k}+x_1D_{2k}+D_{12}}+\frac{k_p\rho_2}{\mu_{mix}}\right)\frac{dp_1}{dz}+\left(\frac{(x_2D_{2k}D_{1k}+D_{12}D_{2k})/R_gT}{x_2D_{1k}+x_1D_{2k}+D_{12}}+\frac{k_p\rho_2}{\mu_{mix}}\right)\frac{dp_2}{dz}\right) \tag{4-8b}$$

The overall gas volume flux Q_{ij}^{g} through pore throat *ij* can be wrote as

$$Q_{ij}^{g} = \frac{\pi r_{ij}^{2}(J_{1,ij}+J_{2,ij})}{\rho_{ij}^{g}} = -\left(K_{ij}^{g}\left(P_i^{g} - P_j^{g}\right) + K_{ij}^{g2}\left(P_i^{g2} - P_j^{g2}\right)\right) \quad (4\text{-}9)$$

where $K_{ij}^{g} = \left(\frac{(D_{2k,ij}D_{1k,ij}+D_{12,ij}D_{2k,ij})/R_gT}{x_{2,ij}D_{1k,ij}+x_{1,ij}D_{2k,ij}+D_{12,ij}} + \frac{k_p\rho_{ij}^{g}}{\mu_{mix}}\right)\frac{\pi r_{ij}^{2}}{\rho_{ij}^{g}l_{ij}}$ and $K_{ij}^{g2} = \left(\frac{D_{12,ij}(D_{2k,ij}-D_{1k,ij})/R_gT}{x_{2,ij}D_{1k,ij}+x_{1,ij}D_{2k,ij}+D_{12,ij}}\right)\frac{\pi r_{ij}^{2}}{\rho_{ij}^{g}l_{ij}}$ are transport coefficients. P_i^{g2} is the vapor's partial pressure in pore body i, $\rho_{ij}^{g} = 0.5(\rho_i^{g} + \rho_j^{g})$ is the average molar density in pores i and j. Substituting Eqs. (4-6) and (4-9) into Eq. (4-5), we obtain

$$\sum_{j=1}^{N_i}\left(K_{ij}^{l}\left(P_i^{l} - P_j^{l}\right) + K_{ij}^{g}\left(P_i^{g} - P_j^{g}\right) + K_{ij}^{g2}\left(P_i^{g2} - P_j^{g2}\right)\right) = 0 \quad (4\text{-}10)$$

Eq. (4-10) can be reformulated using the average pressure of pore body $\tilde{P}_i = (1 - S_i^{l})P_i^{g} + S_i^{l}P_i^{l}$ as

$$\sum_{j=1}^{N_i}\left(K_{ij}^{l} + K_{ij}^{g}\right)\left(\tilde{P}_i - \tilde{P}_j\right) = -\sum_{j=1}^{N_i}\left(K_i^{c}P_i^{c} - K_j^{c}P_j^{c} + K_{ij}^{g2}\left(P_i^{g2} - P_j^{g2}\right)\right) \quad (4\text{-}11)$$

where $K_i^{c} = K_{ij}^{g}S_i^{l} - K_{ij}^{l}\left(1 - S_i^{l}\right)$ and $K_j^{c} = K_{ij}^{g}S_j^{l} - K_{ij}^{l}\left(1 - S_j^{l}\right)$.

Using the kinetic theory of gas transport inside nanopores and considering the first order slippage effect, the effective permeability for gas through a pore throat ij is given by[199]

$$k_p = \frac{r_{ij}^{2}}{8}\left(1 + 4\mathrm{Kn}\left(\frac{2}{\sigma_v} - 1\right)\right) \quad (4\text{-}12)$$

where σ_v is the tangential momentum accommodation coefficient. We assume $\sigma_v = 1$, which corresponds to a rough pore surface that reflects all molecules diffusively. $\mathrm{Kn} = \lambda/2r_{ij}$ is the Knudsen number of the gas mixture (λ is the mean free path for the gas mixture, see below), which defines the ratio of the Knudsen diffusion to self-diffusion in a bulk gas.

Properties of gas mixture: To complete the above gas transport model, the mutual diffusivity, mixture viscosity, and the mean free path of the gas mixture are needed. The mutual diffusivity in a pore throat ij is approximated using the empirical formula[19, 21]

$$D_{12} = \left(D_{x_1\to 1}\right)^{x_1}\left(D_{x_1\to 0}\right)^{(1-x_1)} \quad (4\text{-}13)$$

where $x_1 = 0.5(x_{1,i} + x_{1,j})$ is the molar fraction of species 1 in a pore throat ij, which is taken as the average of the molar faction of species 1 in pore body i ($x_{1,i}$) and pore body j ($x_{1,j}$). The bracketed terms are the infinite dilution values for the Maxwell-Stefan diffusivity at either end of the composition range and are given by $D_{x_i\to 1} = \frac{2}{3}\frac{\sqrt{m_i k_B T/\pi}}{M_i\sigma_{ai}\rho_i}$ $(i = 1,2)$, where m_i, M_i and σ_{ai} are the molecular mass, molar mass and effective collision cross-section area of specie i, respectively.

We approximate the viscosity of the binary gas mixture using an empirical correlation:[200]

$$\mu_{mix} = \frac{\mu_1}{1+\frac{x_2 1.385\mu_1}{x_1 D_{12}\rho_1}} + \frac{\mu_2}{1+\frac{x_1 1.385\mu_2}{x_2 D_{12}\rho_2}} \tag{4-14}$$

where μ_i is the viscosity for a species *i*. The mean free path of a binary gas mixture is given by

$$\lambda = \frac{x_1 m_1 + x_2 m_2}{\sqrt{2}\sigma_{a1}^{x_1}\sigma_{a2}^{x_2}(M_1\rho_1 + M_2\rho_2)} \tag{4-15}$$

B.3 Liquid vaporization model

The evaporation of liquid solvents at the corner of pore bodies and the vapor's subsequent transport to the pore center are essential steps of the vaporization process induced by purge gas. Since we assume that drying proceeds under the isothermal condition, the vaporization rate is limited by the vapor transport from the liquid surface toward the pore's center rather than the kinetics of liquid evaporation. Therefore, the vapor density on the liquid surface is equal to the liquid's saturation vapor density ρ_{sat} and the vaporization from the liquid surface inside a pore body *i* is given as:

$$\dot{m}_i^{evp} = \beta A_s(\rho_{sat} - \rho_i^{g2}) \tag{4-16}$$

where β is the mass transfer coefficient. A_s is the interfacial area between the liquid solvent and the gas phase inside the pore body and it is given by:[192]

$$A_s = \begin{cases} \frac{144}{\pi} r_i^2 \left(1 - S_i^l\right)^{\frac{2}{3}}, & S_i^l \geq 0.476 \\ \frac{12\pi r_i \gamma}{P_c} - \frac{8\pi\gamma^2}{P_c^2}, & S_i^l < 0.476 \end{cases} \tag{4-17}$$

The mass transfer of vapor from the surface of liquids at pore corners to the pore interior is characterized using the Sherwood number $Sh = 2\beta r_i/D_s$, which depends on the pore's shape. Here Sh is taken as 2.98, which corresponds to square-shaped pores.[201] Note that the above treatment of the vaporization flux neglects the Knudsen effects. In our pore network, the gas pressure is smallest at the network's exit (1.0 bar), which corresponds to a largest mean free path of ~60 nm. For the mass exchange between liquid and vapor, which occurs *in pore bodies*, the relevant length scale is the pore width. Because the smallest pore width is 1.6 μm in our pore network, the pertinent Kn number is at most 0.04 in the pore bodies of our pore network. Therefore, it is safe to neglect the Knudsen effects.

With the above vaporization model, the mass balance of the solvent vapor in a pore body *i* is given by

$$V_i^g \Delta\rho_i^{g2}/\Delta t = \sum_{j=1}^{N_i} \pi r_{ij}^2 J_{ij}^{g2} + A_s\beta(\rho_{sat} - \rho_i^{g2}) \tag{4-18a}$$

$$J_{ij}^{g2} = -\left(C_{ij}^g\left(P_i^g - P_j^g\right) + C_{ij}^{g2}\left(\rho_i^{g2} - \rho_j^{g2}\right)\right) \tag{4-18b}$$

where $V_i^g = V_i(1 - S_i^l)$ is the volume of the gas phase inside a pore body *i* and Δt is the time step (see B.5 for details), $C_{ij}^g = \frac{x_{2,ij}D_{1k,ij}D_{2k,ij}/R_gT}{x_{1,ij}D_{2k,ij}+x_{2,ij}D_{1k,ij}+D_{12,ij}} + \frac{k_p}{\mu_{mix}}\rho_{ij}^{g2}$ and $C_{ij}^{g2} = \frac{D_{2k,ij}D_{12,ij}}{x_{1,ij}D_{2k,ij}+x_{2,ij}D_{1k,ij}+D_{12,ij}}$ are transport coefficients.

B.4 Initial and boundary conditions

Initially, the pore network is fully saturated with the liquid solvents:

$$S_i^l(t = 0) = 1.0 \tag{4-19}$$

During drying, the pressure at the pore network's inlet (*y*=0 in Fig. 4-2) is fixed to that of the upstream purge gas reservoir P_u and no solvent vapor is transported into the pore from the upstream reservoir:

$$y = 0:\ P^g|_{y=0} = P_u \tag{4-20a}$$

$$y = 0^-: J^{g2} = 0 \tag{4-20b}$$

The pressure at the pore network's outlet ($y = L$ in Fig. 4-2) is fixed to that at the downstream reservoir (P_d):

$$y = L: P^g|_{y=L} = P_d \tag{4-20c}$$

$$y = L: \frac{\partial\rho^{g2}}{\partial y} = 0 \tag{4-20d}$$

B.5 Rules

1. *Threshold pressure for pore throats.* Because the contact angle of solvent liquids on the solid surfaces is zero, the threshold pressure for pore throats filled with liquids is

$$P_{th,ij} = \frac{2\gamma}{r_{ij}} \tag{4-21}$$

A pore throat filled with liquid can be invaded by the gas phase if the capillary pressure in the neighboring pore body exceeds the threshold pressure of this pore throat: [192]

$$P_c(S_i^l) > P_{th,ij} \quad \text{or} \quad P_c(S_j^l) > P_{th,ij} \tag{4-22}$$

Because the liquid saturation S_i^l in a pore body can be reduced by vaporization of the liquid solvents in it, Eq. (4-22) implies that evaporation can indirectly affect the invasion of a pore throat by liquid solvents or gas.

2. *Re-imbibition of pore throats*. If a pore body *i* is refilled with liquid solvent ($S_i^l = 1.0$), an empty throat (i.e., a throat free of liquid) *ij* can be re-imbibed with the liquid under the condition[196]

$$P_i^g > P_j^g \tag{4-23}$$

where P_i^g is the gas pressure of the target pore body and P_j^g is the gas pressure in the pore body connected to the target pore body by the throat *ij*.

3. *Selection of time step.* The time step for each iteration in the pore network simulation is determined based on the local time steps required for draining a pore body to the critical state, i.e., when the local capillary pressure satisfies $P_c(S_i^l) = \min\{P_{th,ij}\}$. Since the imbibition process is allowed to occur locally in pore bodies, the local time step can be determined by the time required to refill the pore body[192]:

$$\Delta t_i = \begin{cases} \frac{V_i}{\sum_{j=1}^{N_i} Q_{ij}^l}\left(S_i^l - S_{i,ct}\right) & \text{local drainage, } \sum_{j=1}^{N_i} Q_{ij}^l < 0 \\ \frac{V_i}{\sum_{j=1}^{N_i} Q_{ij}^l}\left(1 - S_i^l\right) & \text{local imbibition, } \sum_{j=1}^{N_i} Q_{ij}^l > 0 \end{cases} \tag{4-24}$$

where $S_{i,ct}$ is the saturation corresponding to the critical state. Using the $P_c - S_i^l$ relation by Eq.(4-4), the critical saturation can be given as

$$S_{i,ct} = -\frac{1}{6.83}\ln\left(1 - \frac{2\gamma}{r_i \min\{\Delta P_{ud}, \min\{P_{th,ij}\}\}}\right) \tag{4-25}$$

where $\Delta P_{ud} = P_u - P_d$ is the global pressure difference between the upstream and downstream reservoir. $\min\{P_{th,ij}\}$ is the minimum threshold pressure among the liquid throats connected to the target pore body. Then the global time step is selected as the minimum of all local time steps, i.e., $\Delta t = \min\{\Delta t_i\}$.

C. Computational algorithms

Starting from the initial conditions given by Eq. (4-19), Eqs. (4-4) and (4-11) are combined with the boundary conditions given by Eq. (4-20) to solve the pressure field in the pore network

using the direct sparse-matrix solver (DSS).[202] Using this pressure field, the solvent vapor density for the next time step is computed by solving Eqs. (4-17) and (4-18) subject to the boundary conditions in Eq. (4-20) using an implicit scheme. These calculations are repeated till the entire pore network is free of liquid solvents. These and other details of the computational algorithms for solving the pore network model are summarized in Fig. 4-3.

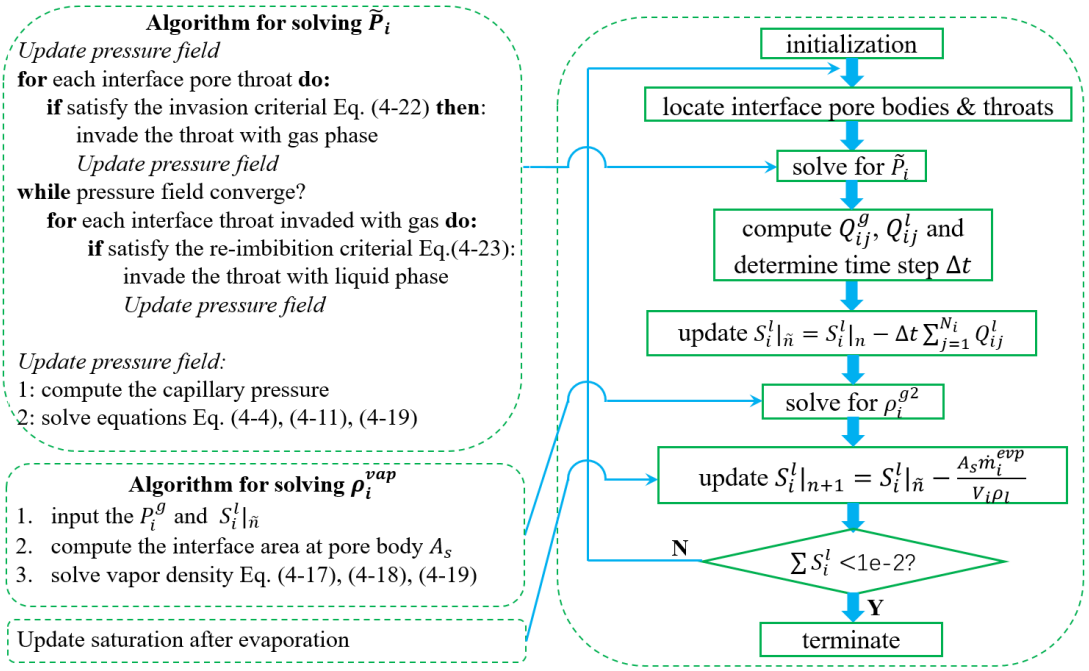

Figure 4-3. The computational procedure and algorithm for solving the pore network model in which drainage and evaporation can occur concurrently.

4.3. Results and Discussion

We consider the drying of a porous coal cake initially saturated with liquid solvent pentane by the flow of a purge gas N_2 through the cake. Because coal particles' diameter is often less than a few micrometers, the size of the pores in the coal cake can be a few hundred nanometers. Here, the coal cake is represented using a pore network consisting of 80×80 pore bodies, with each pore body connected to its 4 nearest pore bodies as shown in Fig. 4-2a. The size of pore bodies follows the truncated log-normal distribution with $\sigma_b = 0.22$, $r_{b,m} = 1.2$ μm, $r_{b,min} = 0.8$ μm and $r_{b,max} = 1.4$ μm. The size of pore throats follows the same distribution with $\sigma_t = 0.18$, $r_{t,m} = 300$ nm, $r_{t,min} = 200$ nm and $r_{t,max} = 400$ nm. The size distributions of the pore bodies and

throats are shown in Fig. 4-2c and 2d. The pore bodies and throats generated above are randomly packed into the pore network. With these parameters and the gas pressure being smallest at the network's exit (1 bar, see below), the maximal Kn number in the pore network is 0.17 and is found in the pores with a radius of 200 nm near the pore network's exit. Therefore, the Knudsen effects, although not significant, cannot be neglected.

The system temperature is 300 K. The material properties of the purge gas (N_2) and solvent (pentane) at this temperature are summarized in Table 4-1. Note that the effective cross-section areas of the N_2 and pentane molecules ($\sigma_{a,1}$ and $\sigma_{a,2}$) are calculated based on the results in Ref. [203].

Table 4-1. Properties of the purge gas N_2 (species 1) and solvent (species 2).

$m_1 = 4.65\times10^{-26}$ kg	$\sigma_{a,1} = 0.43$ nm^2
$m_2 = 12.0\times10^{-26}$ kg	$\sigma_{a,2} = 2.09$ nm^2
$\rho_{sat,2} = 28.1$ mol/m^3	$\mu_1 = 17.8$ μPa·s (gas state)
$P_{sat,2} = 0.7$ bar	$\mu_2 = 70.0$ μPa·s (gas state)
$\rho_2 = 626.0$ kg/m^3 (liquid state)	$\mu_1 = 224.0$ μPa·s (liquid state)
$\gamma = 15$ mN/m	

The pressure in the reservoir downstream the pore network, P_d, is 1.0 bar. For selection of the upstream gas pressure (P_u) , we identify a minimal pressure difference as

$$\Delta P_{ud}^{min} = \frac{2\gamma}{r_{t,min}} \tag{4-28}$$

When $P_u - P_d = \Delta P_{ud}^{min}$, not all all pores inside the pore network can be emptied by drainage because the pressure drop along individual throats is smaller than the global pressure difference across the entire pore network. Nevertheless, ΔP_{ud}^{min} provides an indication of the ability of the applied pressure difference to drain liquids from the pore network. For the pore network studied here, ΔP_{ud}^{min} =1.5 bar. In our simulations, we select $\Delta P_{ud} = P_u - P_d = 1.4, 1.5,$ and 2.0 bar to study how the applied pressure difference affects the drying behavior. These values are within the range used in the dewatering-by-displacement technology.[190]

A. Macroscopic drying behaviors

To quantify how a porous medium initially saturated with liquid solvents is dried, we define a *degree of drying* δ using $\delta(t) = 1 - \bar{S}(t)$, where $\bar{S}$ is the ratio of the liquid solvent mass at a time t and the initial solvent mass in the porous medium. In purge gas-assisted drying of a porous medium, solvent can be removed as liquid through drainage (termed drainage effect) and by the transport of vaporized solvents out of the porous medium (termed evaporation effect). We thus decompose the net solvent removal rate $\dot{F}_{net}$ from the porous medium as $\dot{F}_{net} = \dot{F}_{drn} + \dot{F}_{evp}$, where $\dot{F}_{drn}$ and $\dot{F}_{evp}$ are solvent fluxes at the porous medium' outlet due to the drainage and evaporation effects, respectively. To quantify the relative importance of the drainage and evaporation effects, we further define an evaporation-to-drainage ratio as $\alpha = \dot{F}_{evp}/\dot{F}_{drn}$.

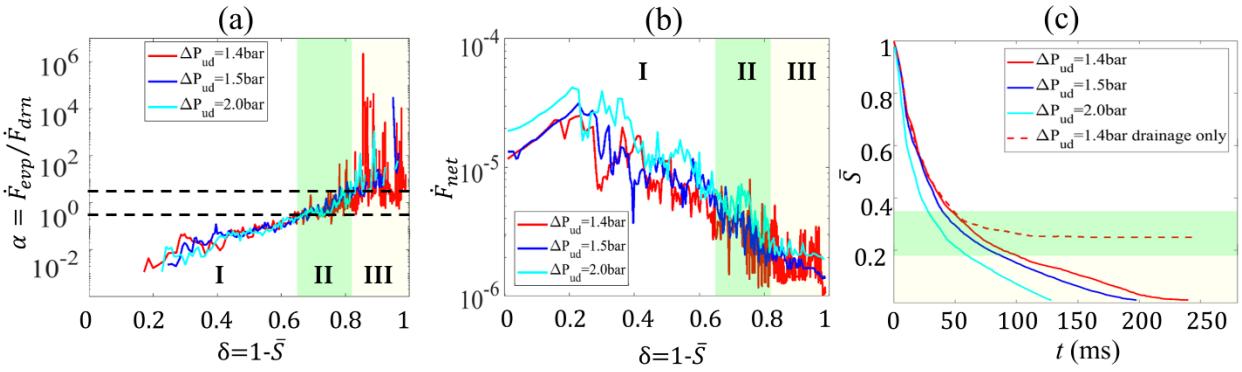

Figure 4-4. *The overall drying behavior at different applied pressure* ΔP_{ud}. (**a-b**) The evolution of the ratio of removal rates of solvent as vapor and liquid (a) and the total solvent removal rate (b) as a function of the degree of drying δ. **(c)** The evolution of the average liquid saturation in the porous medium. The dashed line corresponds to the simulation in which evaporation is disabled.

Figure 4-4a shows the evolution of α during drying under three pressure differences ΔP_{ud}. As drying proceeds, α generally increases, i.e., the evaporation effect becomes more and more important. Base on the relative importance of the drainage and evaporation effects, the drying process under all ΔP_{ud} can be divided into three stages: *stage I* with $\alpha < 0.3$, during which the solvent removal is dominated by the drainage effect; *stage II* with $0.3 < \alpha < 3.0$, during which the drainage and evaporation effects are comparable; *stage III* with α mostly larger than 3, during which the drying is largely dominated by the evaporation effects. For all ΔP_{ud}, the degree of drying

spanned by each stage is similar, i.e., $\delta \lesssim 0.65$ in stage I, $0.65 \lesssim \delta \lesssim 0.82$ in stage II, and $\delta \gtrsim 0.82$ in stage III. During stage III, α fluctuates notably and can reach ~0.3-1 (i.e., drainage notably contributes to solvent removal), and this is especially pronounced for the smallest ΔP_{ud} studied (1.4 bar). The contribution of drainage to the solvent removal during each stage is summarized in Table 4-2. We observe that, in the first two stages, the contribution of drainage to solvent removal is similar for all ΔP_{ud}. However, in stage III, drainage contributes more significantly at lower ΔP_{ud}, e.g., the contribution of drainage to solvent removal increases from 6.2% at $\Delta P_{ud} = 2.0$ bar to 21.4% at $\Delta P_{ud} = 1.4$ bar. Nevertheless, because most of the solvents are removed during stage I, the overall contribution of drainage to solvent removal does not differ greatly for the ΔP_{ud} studied: as ΔP_{ud} decreases from 2.0 to 1.4 bar, the contribution of drainage increases only by 1.5%. Nevertheless, because solvent removal by drainage avoids the energy cost due to the heat of vaporization needed in evaporation-induced solvent removal, even a small increase of drainage's contribution is desirable, especially in large-scale applications.

Table 4-2. The contribution of drainage to the solvent removal and the duration of each drying stage.

		ΔP_{ud}	ΔP_{ud}	$\Delta P_{ud} = 2.0\ bar$
contribution of drainage to the solvent removal	stag	96.1%	96.6%	96.9%
	stag	57.8%	53.1%	61.0%
	stag	21.4%	8.9%	6.2%
	total	75.9%	73.3%	74.4%
duration (ms)	stag	46.82	39.58	27.77
	stag	53.91	47.77	32.22
	stag	139.30	110.50	68.46
	total	240.03	197.85	128.45

Figure 4-4b shows the evolution of the net solvent removal rate $\dot{F}_{net}$ during drying. Overall, $\dot{F}_{net}$ is higher for larger ΔP_{ud}. The $\dot{F}_{net}$ curves at different ΔP_{ud} exhibit similarities. First, $\dot{F}_{net}$ fluctuates notably except at the beginning of stage I. Second, the time evolution of $\dot{F}_{net}$ is similar: in stage I, $\dot{F}_{net}$ increases first and then decreases. $\dot{F}_{net}$ continues to decrease in stage II

but plateaus in stage III. Significant fluctuation of $\dot{F}_{net}$ is observed in the stage III, especially at $\Delta P_{ud} = 1.4$ bar.

Figure 4-4c shows the time evolution of the averaged solvent liquid saturation in the porous medium. The liquid saturation decreases sharply during stage I, but the decrease of saturation slows down in stage II and even more so in stage III. These observations are consistent with the fact that, as drying proceeds, drying becomes controlled more by the evaporation effects and the solvent removal rate decreases (see Fig. 4-4a and 4-4b). Note that the evaporation effects are essential for the complete removal of solvents. To appreciate this, we perform simulations in which the vaporization of liquid solvents is disabled and only drainage is allowed. Comparison of the result of this simulation (the dashed line in Fig. 4-4c; more drainage statistics are summerized in table B1 of the appendix B) with the above result shows that, as the average liquid saturation reduces to ~0.3, the solvent removal starts to be affected by the evaporation effect. In absence of the evaporation effects, a significiant fraction of the liquid solvents remains trapped.

Figure 4-4c shows that the evaporation effects-dominated stage III lasts longer compared to the other two stages, i.e., the throughput of drying is limited by the removal of solvents by evaporation effects. This is seen more clearly in Table 4-2, in which the time corresponding to each drying stage is listed. The time needed for the stage III is especially long under the applied pressure difference of 1.4 bar. The reason for this is as follows. At stage III, the pathway for gas (purge gas and solvent vapor) transport evolves slowly and thus the gas flow rate is relatively stable. The net flux of vaporized solvents out of a pore network is determined by the vapor speed and the number of pores accessible for gas transport at its exit. The former is affected both by the driving force for gas transport (ΔP_{ud}) and the topology and length of the gas transport pathway. For the case with $\Delta P_{ud} = 1.4$ bar, the gas transport driving force is smaller than the other cases ($\Delta P_{ud} = 1.5$ and 2.0 bar). Furthermore, at $\Delta P_{ud} = 1.4$ bar, there are more trapped throats in the pore network. Hence there are less pore bodies and throats accessible by gas flow and the gas transport pathways tend to be more tortuous than at higher ΔP_{ud}. Therefore, the drying time at stage III are longer at $\Delta P_{ud} = 1.4$ bar than at $\Delta P_{ud} = 1.5$ and 2.0 bar.

B. Microscopic drying processes

The existence of three drying stages, the contributions and interplay of drainage and evaporation effects during drying, and finally the evolution of the drying rate revealed in Fig. 4-4 can be understood by examining the microscopic processes in the pore network during drying. Figure 4-5 shows the snapshots of the liquid saturation distribution in the pore network at four representative degrees of drying (δ) when the applied pressure difference is $\Delta P_{ud} = 1.5$ bar. Similar results are observed for other ΔP_{ud} and are not shown here.

Once the pressure difference is imposed across the pore network, the purge gas starts to invade into the pore network. The purge gas travels preferentially through pathways with wider pore throats and displaces the liquids in a piecemeal manner. This is evident in Fig. 4-5a (δ =0.16), where finger-shaped gas paths are observed. The formation of these paths, often referred to as viscous fingering,[204-205] is generally considered as the onset and evolution of instabilities when a more viscous fluid (here, liquid solvent) is displaced by a less viscous fluid (here, purge gas). As the viscous fingers grow, the network formed by liquid-saturated pore bodies is fragmented into liquid clusters (hereafter, a liquid cluster is defined as a collection of pore bodies fully saturated by liquids and connected continuously by liquid-filled throats). In particular, the initial main liquid cluster spanning the entire pore network is fragmented into small liquid clusters, which are broken into even smaller clusters later. Many small liquid clusters, along with some large liquid clusters, appear inside the system (see Fig. 4-5b, where δ =0.5). During the early part of this process, as viscous fingers move toward but have not yet reached the pore network's outlet, the resistance for drainage decreases and the drainage rate increases, which is consistent with the initial increase of the drying rate (see Fig. 4-4b, $\delta \lesssim 0.2 - 0.3$). After the purge gas breaks through the pore network, drainage from the pore network's outlet becomes more limited. Therefore, the drying rate decreases as shown in Fig. 4-4b and the evaporation effects begin to contribute to solvent removal. However, until drainage pathways are diminished by the fingering of gas pathways, the removal of solvents is dominated by drainage and drying is in the stage I identified in Fig. 4-4a.

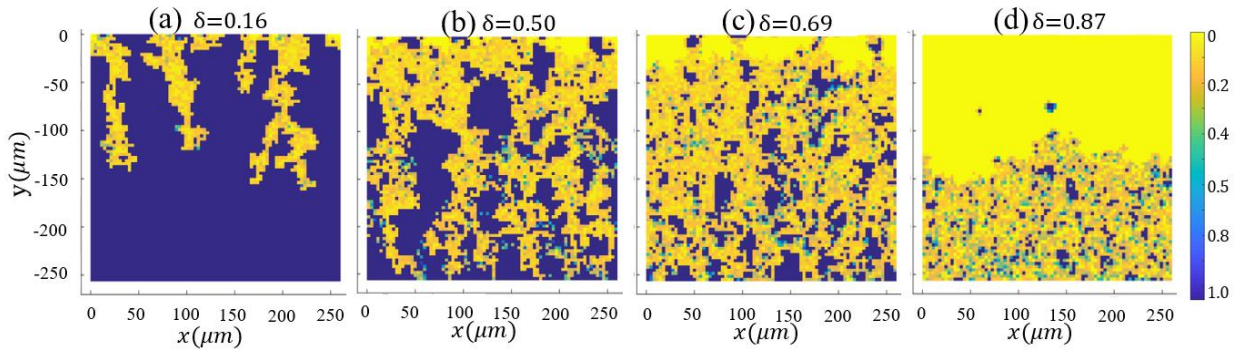

Figure 4-5. The evolution of liquid saturation in the pore network when the applied pressure difference ΔP_{ud} is 1.5 bar.

As drying proceeds, the liquid saturation throughout the pore network reduces, and this is evident in the snapshot in Fig. 4-5c (δ=0.69). Consequently, the drainage of liquid solvents through the network is reduced while more pathways for vaporized solvents to be "flushed" out of the network emerge. The solvent removal by the evaporation effects thus increases. The contributions of drainage and evaporation effects eventually becomes comparable and drying enters stage II. Because drainage is much more effective in removing solvent (note that the density of liquid solvents is >100 times larger than the density of vaporized solvents), the net drying rate continues to decrease in stage II.

In stage II of the drying process, a drying front, behind which few liquid clusters exist, appears near the pore network's inlet (see Fig. 4-5c) and moves downstream as drying proceeds. However, it important to note that solvents are removed from individual pores both near and *far ahead of* this drying front. As drying continues, more and more pores near the network's outlet become only partially occupied by liquid solvents (see Fig. 4-5d). Therefore, solvent removal by drainage (evaporation effects) diminishes (becomes significant), and drying enters stage III as shown in Fig. 4-4a.

In stage III, the drying rate is quite stable for ΔP_{ud} = 1.5 and 2.0 bar (see Fig. 4-4b). Even for ΔP_{ud} = 1.4 bar, the drying rate largely fluctuates around a constant value. These trends can be understood as follows. At this stage, small liquid clusters are mostly trapped in pores with narrow throats. The pathway for gas (purge gas + solvent vapor) transport evolves only slowly and the gas flow rate is relatively stable. Furthermore, as the purge gas flows toward the exit, it is in close

contact with many pore throats partially or fully saturated with liquid solvents. Thus the gas phase at the pore network's exit is generally saturated with the solvent vapor (except toward the very end of drying). Therefore, the net flux of vaporized solvents out of the porous medium is rather stable. Because drying is dominated by the vaporized solvents, the total drying rate is relatively stable.

In stage III, the solvent vapor tends to diffuse against the flow of purge gas toward the pore network's entrance because the vapor density at the pore network's exit is highest in the pore network. We find that the solvent vapor generally has a non-negligible density at the pore network's entrance. For example, for $\Delta P_{ud} = 1.5$ bar, at t = 112 ms, when the liquid saturation at the pore network's entrance has already dropped to zero, the vapor density at the pore network's entrance is about 8.4% of its saturation density. This result suggests that the transport diffusion of solvent vapor should indeed be considered in the model.

C. The interplay between drainage and evaporation effects

The above analysis highlights the role of drainage and evaporation effects in purge gas-assisted drying of porous media and helps understand the main features of the macroscopic drying behavior. However, some features of the drying data shown in Fig. 4-4 still cannot be readily understood. For example, a notable drainage flux can still appear after the evaporation effects start to dominate drying (see Fig. 4-4a and Table 4-2), which is also manifested as the spikes in the net drying rate in stage III (see Fig. 4-4b). These features essentially arise from the coupling between the drainage and evaporation effects.

To understand the coupling between drainage and evaporation effects and its impact on the macroscopic drying behavior, it is instructive to examine the evolution of liquid clusters in the pore network, which are affected oppositely by the two processes: in drainage, purge gas breaks through liquid clusters to fragment them into small clusters; the evaporation in pore bodies tends to eliminate small liquid clusters. Figure 4-6a shows the evolution of the number of liquid clusters N_c in the pore network. In stage I, evaporation effects are minor and N_c increases rapidly as viscous fingers break through increasingly smaller clusters. In stage II, fragmentation of liquid clusters by purge gas "fingers" becomes weaker while the elimination of liquid clusters by

evaporation effects becomes significant. The competition of these processes leads to a plateau of N_c. In stage III, where evaporation effects dominate, N_c decreases.

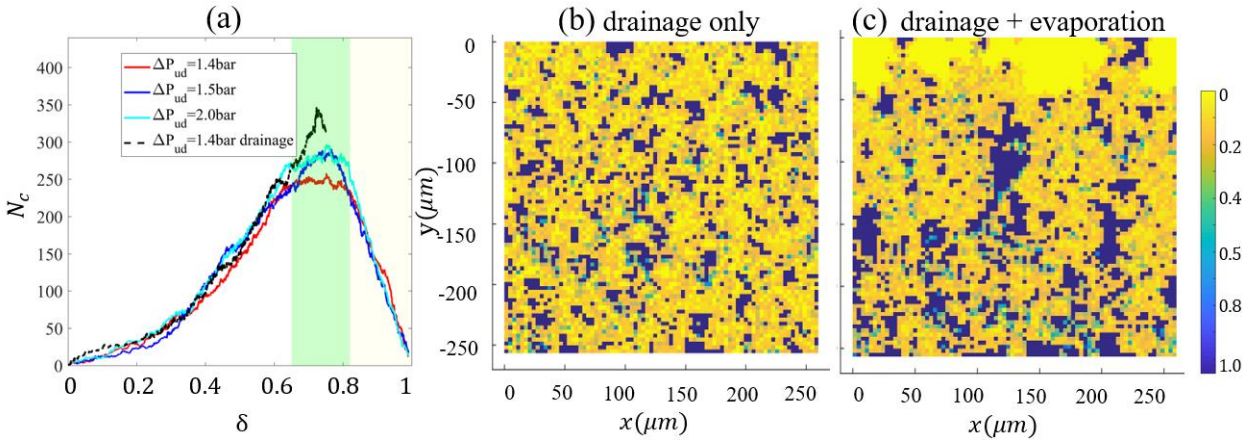

Figure 4-6. (**a**) The evolution of the number of liquid clusters in the pore network during drying and drainage-only operations. (**b-c**) The distribution of the liquid saturation in a pore network at a degree of drying of $\delta = 0.7$ as obtained from drying simulations (b) and drainage-only simulations (c). The pressure difference ΔP_{ud} is 1.4 bar.

To more directly appreciate the *coupling* between drainage and evaporation effects, we performed a new simulation in which the evaporation effects are turned off so that only drainage exists. The setup of the pore network is identical to the drying simulation reported above and the pressure difference ΔP_{ud} is set to 1.4 bar. Figure 4-6a shows that, in absence of evaporation effects, the evolution of N_c is similar in the drainage and drying simulations till the degree of drying δ reaches 0.6, which is expected because evaporation effects are weak in the stage I drying. However, in absence of evaporation effects, N_c increases with δ till it reaches ~0.7. After that, solvents are permanently trapped in small liquid clusters (see Fig. 4-6b) and N_c remains constant. Importantly, in this case, numerous liquid clusters with small size are scattered throughout the pore network (see Fig. 4-6b), in sharp contrast with the fact that, at the same δ, the liquid clusters in the simulation with both drainage and evaporation effects have much larger size and are distributed closer to the pore network's outlet (see Fig. 4-6c). This difference can be understood as follows. Once evaporation enables the emptying of a pore throat connected to a liquid cluster, drainage can displace the liquid in the cluster to neighboring pore bodies. This effectively drives the liquid cluster downstream and even allows it to merge with other liquid clusters and form the large liquid clusters seen in Fig. 4-6c.

The coupling between drainage and evaporation effects revealed through the comparison between Fig. 4-6b and 4-6c affects the macroscopic drying behavior. For example, the liquid clusters near the pore network's outlet can be removed through drainage, which helps explain why the solvent flux at the porous medium's outlet frequently includes a significant faction of liquid even in stage III of drying (see Fig. 4-4a, especially when ΔP_{ud} is 1.4 bar).

The extent of the coupling between drainage and evaporation effects during a drying process is affected by both the operating conditions (e.g., the applied pressure difference) and the stage of drying. To gauge the extent of this coupling, we note that, the coupling between the drainage and evaporation effects can be considered as three steps looped together. First, evaporation triggers the emptying of pore throats (see Eq. (4-22)) and prompts liquid to drain from pores. Second, drainage generates new gas transport pathways and affects the liquid saturation distribution in the pore network. Third, the altered gas transport pathways and liquid saturation distribution in turn affect the evaporation of liquid solvents in the partially saturated pores. These looped steps are most easily delineated for a liquid cluster surrounded by very narrow pore throats (see *Appendix B*) but they are applicable to all liquid clusters in a pore network. Because the coupling loop between drainage and evaporation effects is triggered when evaporation induces the emptying of pore throats, we can infer the extent of such coupling by counting the number of its triggering events (i.e., evaporation-induced emptying of pore throat) N_{trig}. A larger N_{trig} corresponds to a more extensive coupling between the drainage and evaporation effects during drying.

Figure 4-7a, 4-7b, and 4-7c show the histogram of N_{trig} under an applied pressure difference of $\Delta P_{ud} =$ 1.4, 1.5, and 2.0 bar, respectively. There are few triggering events for drainage-evaporation coupling in stage I, but these events start to appear in stage II, when the drainage and evaporation effects become comparable. In stage III, when the evaporation effect dominates, many triggering events are detected. The number of triggering events is largest at $\Delta P_{ud} =$ 1.4 bar, i.e., the coupling between the drainage and evaporation effects is most extensive at this applied pressure difference. As discussed in section III.B, liquid clusters can be removed in two processes in presence of the coupling effects: (1) liquid clusters can migrate downstream, merge with other

liquid clusters, and be drained out of the pore network at its outlet; (2) liquid clusters can be directly removed from the porous media via evaporation effects. Because the coupling of drainage and evaporation effects is more extensive for ΔP_{ud} = 1.4 bar, the first process is strongest at this applied pressure difference. This explains why, during stage III of drying, the removal of liquid solvents by drainage from the pore network's outlet is more significant for ΔP_{ud} = 1.4 bar than for ΔP_{ud} = 1.5 and 2.0 bar (see Fig. 4-4a and Table 4-2).

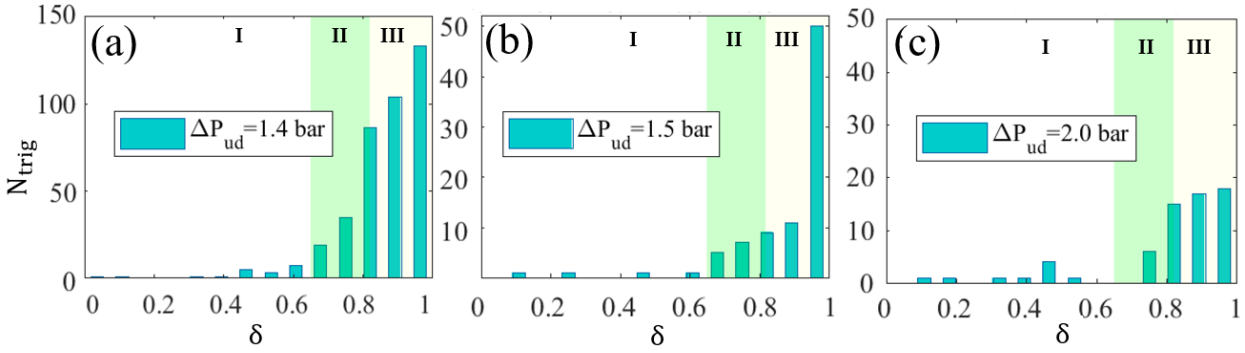

Figure 4-7. *The statistics of the triggering events (evaporation-induced emptying of pore throats) in the drainage-evaporation coupling loops during drying*. (**a-c**) The histogram of the number of triggering events as a function of the degree of drying δ under different applied pressure differences.

4.4. Conclusions

In this work, we develop a new pore network model for purge gas-assisted drying of porous media with nanoscale pores. The model considers multiphase and multiphysics processes such as liquid drainage, evaporation, and transport of gas mixtures through nanopores. Solutions of the model indicate that the drying process can be divided into three stages. In stage I, drying is dominated by drainage, in which gas flow displaces the liquid solvent in a fingering pattern. The net drying flux increases before the purge gas breaks through the porous medium and decreases after that. During this process the number of liquid clusters in the porous medium increases. In stage II, the evaporation effects become comparable to the drainage effect. While drainage tends to increase the number of liquid clusters in the porous medium, evaporation tends to reduce the number of liquid clusters. Hence, the number of liquid clusters in the porous medium plateaus. As drying proceeds to stage III, the liquid removal is largely dominated by the evaporation effects,

although notable drainage can also occur at the porous medium's outlet, especially when the pressure driving the purge gas is low.

A key feature of the present drying process is the coupling between the drainage and evaporation effects. Evaporation can trigger three-step coupling loops that begin with the emptying of pore throats, continue with the drainage of liquids and fragmentation of liquid clusters, and continue with evaporation in the newly created partially saturated pore bodies. Because of the interplay between drainage and evaporation effects in these coupling loops, studying purge gas-assisted drying by dividing it into a drainage period and an evaporation period and studying them separately is generally inadequate (cf. the vastly different liquid saturation distributions in Fig. 4-6b and 4-6c). The coupling between drainage and evaporation effects depends on operating conditions, e.g., it is extensive in a porous medium when the applied pressure difference is comparable to the minimum threshold pressure for gas to invade the narrowest pore throats. The extent of coupling greatly affects the evolution of the liquid clusters in the porous medium and consequently the drying behavior, e.g., as the coupling becomes more extensive, liquid removal through drainage in stage III of the drying process increases, which helps increases the energy efficiency of drying. The insight on the coupling between the drainage and evaporation effects in purge gas-assisted drying helps guide future application of this method.

Chapter 5. Predicting Effective Diffusivity of Porous Media by Deep Learning

Disclosure:

This work has been published by Springer Nature: Wu, H.; Fang, W.-Z.; Kang, Q.; Tao, W.-Q.; Qiao, R., Predicting Effective Diffusivity of Porous Media from Images by Deep Learning. *Sci. Rep.* 2019, *9*, 1-12.

5.1. Introduction

Predicting the transport properties of porous materials from their structure is important in numerical simulations of a wide range of engineering problems, e.g., extraction of nature gas from shale reservoirs,[16-18, 87] drying of building materials,[125] and charging/discharging of Li-air batteries. The transport properties of interest include effective diffusivity, permeability, thermal conductivity, among others.[18] A classical approach for calculating these effective transport properties is the pore scale simulations, in which the governing equations for the related transport phenomena are solved within the porous media.[17, 126-127] While this approach can be highly accurate, its computational cost is significant for porous media with large dimension and/or small pore sizes. In fact, for porous media that undergo long operation during which their structure evolves (e.g., the pores in electrodes of Li-air batteries are gradually clogged during discharging), this approach can be prohibitively expensive because their effective transport properties may need to be evaluated for millions of times. As such, the effective transport properties of porous media are often computed using empirical correlations or effective medium theories with their structure information (e.g., porosity) as input. Such an approach needs little computational cost and can be very accurate for some specific (often idealized) classes of porous media. However, because typically only a few structure parameters of the porous media are used as input in this approach, its prediction for complex porous media often lacks specificity and can be inaccurate. Indeed, it remains a great challenge to develop methods for predicting the effective transport properties of porous media that require low computational cost but offer high accuracy for diverse porous structures.

Machine learning can potentially be an effective approach for tackling the above challenge. Deep neural networks have demonstrated good predictive power when their input and output have important correlation with each other. Furthermore, image-based learning has been shown to be able to extract important physical features from images.[206-207] Because the effective transport properties (in particular, the effective diffusivity) of porous media is largely determined by their structure which can be conveniently represented using their binary images, conceivably, one can develop a surrogate deep learning model to extract key geometrical features from images of porous media and predict their transport properties. In terms of implementation, the application of deep neural network typically requires a training dataset, which can be generated numerically or experimentally for porous media. Next, a training model is constructed and trained using the dataset. Finally, the trained model can be used to predict the effective transport properties of new porous structures without repeating the training process. This general strategy resembles the investigation of image classification, where images are taken as the input and trained deep learning models predict the classification label (e.g. “dog” or “cat”) of images by identifying their key features.[208-210] As demonstrated in the studies of image classification, typically, a trained model can be used to make predictions with low computational cost. Therefore, a deep learning model, if well-constructed and trained, can potentially predict the effective transport properties of porous media both accurately and efficiently.

Of the many deep neural network models, convolutional neural network (CNN) [134] is commonly applied to analyze visual imagery and has achieved much success in image classification. Recently, CNN has also been adopted to study the effective properties of complex materials and showed much potential for efficient and accurate prediction of a material’s effective properties from its structure (e.g., presented in the form of images). For example, researchers have used CNN to predict the effective permeability and stiffness of materials from their microstructures.[135, 206-207, 211-212] In particular, three dimensional CNN has shown to capture the nonlinear mapping between material microstructure and its effective stiffness [206]. Study of the prediction of permeability from images of porous media using CNN has provided useful insights

in understanding the correlation between geometric features and transport properties.[135, 212] The features of connectivity between nearby pixels in the image of a porous structure can be extracted by performing convolution with many possible cross shape templates. It has been shown that the features thus extracted can be used to make better prediction of permeability than using the geometric measurements (Minkowski functionals).[212] Furthermore, it has been pointed out that deep learning approach can be further improved by incorporating physical parameters of porous media that are known to affect effective permeability.[135] Nevertheless, the porous structure in previous works is relatively well-defined and of limited geometrical variablity, and some of the chanllenging topologies (i.e. trapped and dead-end pathways) that are commonly seen in porous media were not included. Consequently, it is still not clear whether the CNN model can accurately predict the effective transport properties of practical porous media with diverse geometries and challenging topologies. Delineating the impact of such diversity and complexity of porous media on the performance of CNN models and building more sophisticated deep learning models to deal with them are important for the practical application of CNN models in porous media research.

In this work, we establish a computational framework to predict the effective diffusivity of porous media from their images using CNN. We focus on the effective diffusivity because of its importance in practical applications of porous media. The proposed framework is demonstrated in porous media with a wide range of porosity ($0.28 - 0.98$) and diverse/complex structures (e.g., tortuous diffusion pathways and trapped and dead-end regions). Different filter sizes and convolutional layers are tested during the cross-validation step in order to select the best hyperparameters for CNN. Physical parameter (the porosity) is also combined with the extracted features by CNN with different weights to generate better predictions. The CNN can predict the effective diffusivity of most of the porous media with less than 10% truncated relative error. Nevertheless, the prediction error, especially the relative error, increases as the true diffusivity of the porous media becomes smaller (especially if D_e <0.1). The large error is attributed to the complex transport behavior in porous media with low diffusivity, where the porous structure can be highly heterogeneous with tortuous diffusion pathways and trapped areas or dead-end paths.

The rest of the manuscript is structured as follows: In Section II, we detail the computational framework and methods used for predicting the effective diffusivity of porous media by deep learning models. In Section III, the performance of the developed model is examined and discussed. We first quantify the performance of CNN and compare the CNN prediction with the empirical Bruggeman equation predictions. Then, we attempt to improve the regular CNN prediction by leveraging field knowledge in the development and application of CNN models. Finally, conclusions and discussion on the future research directions of machine learning for porous media research are presented in Sec. IV.

5.2. Computational Framework

In this section, we discuss the deep learning model for predicting the effective diffusivity of porous media with diverse and challenging structures. In part A, we present the methods for generating the dataset for deep learning. In part B, we present the architecture of our CNN model and summarize the computational framework of using CNN to predict the effective diffusivity of porous media from their images. Finally, the methods for training and testing of the CNN models are presented in part C.

A. Generation of datasets

The dataset for training, validating, and testing our deep learning models includes the structure of porous media (in the form of images) and their corresponding effective diffusivity. Without losing generality, we will focus on two-dimensional (2D) porous media with a square shape. The microstructures of 2D porous material are generated using the quartet structure generation set (QSGS) method, a popular method in the porous media field.[213] Detailed descriptions of this method can be found in the literature and we only outline its key steps:[213] (1) The computational domain is partitioned into square cells. (2) Solid "seeds" are randomly distributed in the domain based on a distribution probability, c_d, which is smaller than the target porosity of the porous media. This is accomplished by assigning a random number to each cell and the cells whose assigned random number is less than c_d are selected as the "seeds". (3) Grow the "seeds" to their neighboring cells based on the directional growth probability, P_i. To this end, a

random number is assigned to each of the neighboring cell of a solid seed. If the random number of a neighboring cell is less than P_i, it will become part of the growing solids. (4) Repeat steps (2) and (3) until the target porosity is reached in the domain. Together, the above steps produce binary images of porous media. In these images, individual pores or grains are fully resolved, and each pixel is either a pore or solid node and is denoted with a binary value of 0 (pore space) or 1 (solid phase).

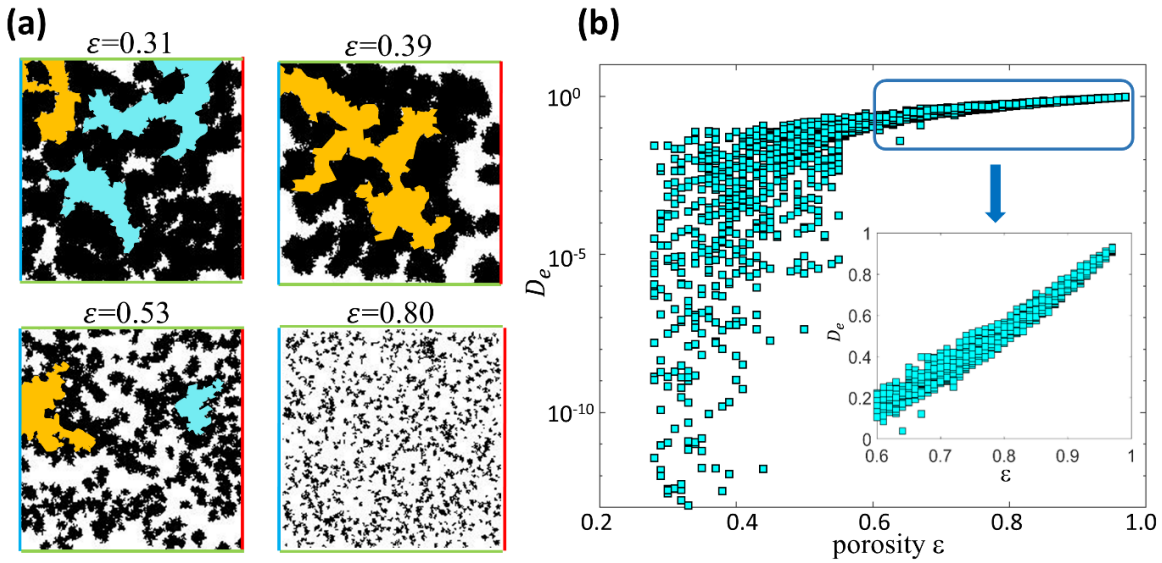

Figure 5-1. (**a**) Representative images of the two-dimensional porous media generated for the deep learning model. The white and black color denote the pore space and solid phase, respectively. The inlet (outlet) for the mass diffusion through the porous media are marked using blue (red) lines. The green lines at the top and bottom side of the porous media denote the periodic boundary in the LBM simulation. The orange areas represent the dead-end pathways (i.e., the pathways that are connected only to the inlet or outlet of the porous structure) and the cyan areas denote the trapped pore space (i.e., isolated pore space that is not connected to the porous structure's inlet and outlet). (**b**) The distribution of the effective diffusivity of porous media generated in this work.

Using the above method, 2-D porous media are generated within a 200×200 (pixel) area. This size of the porous structure is chosen so that (1) the microstructures are large enough to capture the range of the topologies and transport behavior occurring in realistic porous media and (2) the porous structures are small enough so that a large number of porous structures and their effectivity diffusivity can be obtained at a reasonable computational cost. To ensure that the dataset

include a wide variety of porous structures, 1960 samples are generated with porosity (ε) of 0.28, 0.29, ..., 0.98. For each porosity, 28 samples are generated. Figure 5-1a shows the representative images of the porous samples generated. A wide variety of structures featuring tortuous transport pathways, trapped regions, and dead-end pores are obtained in samples with porosity smaller than 0.5.

We next compute the effective diffusivity of the porous structures generated above. The molecular transport within the porous structure is assumed to follow Fick's Law with a constant diffusion coefficient $\widetilde{D}_0$. Therefore, the molecular diffusion within the porous structure obeys the Laplace equation with a zero-flux boundary condition on pore surfaces. To compute the effective diffusivity of each porous structure, a uniform concentration difference ($\Delta\tilde{C}$) is imposed between the left and right boundaries of each porous structure and the periodic boundary condition is imposed on the top and bottom boundaries, respectively. The Laplace equation is solved using the lattice Boltzmann method (LBM). Specifically, a two-dimensional, nine-velocity (D2Q9) LB model is adopted to simulate the diffusion process inside the porous structures. Different from traditional numerical methods by discretizing the Laplace equation in the pore space, LBM solves the evolution equation of the concentration distribution functions

$$g_i(x + e_i\Delta t, t + \Delta t) - g_i(x,t) = -\frac{1}{\tau}(g_i(x,t) - g_i^{eq}(x,t)) \tag{5-1}$$

where g_i is the concentration distribution function at the space location x and time t along i direction; τ is the relaxation time coefficient; $g_i^{eq} = \omega_i C$ is the corresponding equilibrium concentration distribution function, where $C = \sum g_i$ is the macroscopic local concentration, ω_i is weight parameter, and ω_0 = 4/9, ω_{1-4} = 1/9, ω_{5-8} = 1/36. In Eq. (5-1), e_i is the discrete velocity given by

$$e_i = \begin{bmatrix} 0 & 1 & 0 & -1 & 0 & 1 & -1 & -1 & 1 \\ 0 & 1 & 1 & 0 & -1 & 1 & 1 & -1 & -1 \end{bmatrix} \tag{5-2}$$

The relation between the intrinsic gas diffusion coefficient and the relaxation time coefficient is

$$\widetilde{D}_0 = \frac{1}{3}(\tau - 0.5)\frac{\Delta x^2}{\Delta t} \tag{5-3}$$

After the diffusion within the porous structure reaches a steady state, the cross-section averaged diffusive flux through the structure is obtained by[214]

$$J_x = \frac{\int_0^{L_y} \sum e_{i,x} g_i \frac{\tau - 0.5}{\tau} dy}{L_y} \tag{5-4}$$

where L_y is the domain size in the direction normal to the overall diffusion flux. The dimensional effective diffusivity of the porous structure is then determined using Fick's law, i.e., $\widetilde{D}_e = J_x L_x / \Delta C$ (L_x is the domain size in the direction of the overall diffusion flux). Because $\widetilde{D}_e$ is linearly proportional to the molecule diffusion coefficient in the pore space ($\widetilde{D}_0$), the dimensionless effective diffusivity $D_e = \widetilde{D}_e / \widetilde{D}_0$ is used hereafter. The effectivity diffusivity of the porous structures generated above spans ~10^{-10} to 1.0 and is shown as a function of the porosity of the porous structures in Fig. 5-1b.

The data generated above (porous structures and their D_e) are randomly divided into the training dataset (60% of the whole dataset), validation dataset (11.4%) and testing dataset (28.6%). The training dataset is used to optimize the parameters of the CNN model so that the model can describe the training dataset as accurately as possible. The validation dataset is used to select hyperparameters and avoid overfitting the CNN model. The testing dataset is used to evaluate the predictive performance of the trained CNN model.

B. Convolutional neural network for predicting effective diffusivity

The basic concepts of classical and convolutional neural networks, along with terminologies including hyperparameters and learnable parameters, are reviewed in the *Supporting Information*. These models, especially the CNN, have been used for image classification with great success and is being explored for predicting the effective permeability of porous media. Inspired by these works, we adapt the CNN model for predicting the effective diffusivisity of porous media from their images,[209, 215-216] and the architecture of our model is shown in Fig. 5-2. The binary image of a porous structure, in which a pixel with a value of 1 (0) corresponds to the solid phase (pore space), is the input of the CNN. We note that the binary nature of the input image is consistent with the format of the computationally generated porous media in this work (see Section II.A) and is not a result of the binarization of grayscale images as have been done in many image recognization

studies. Because the desired pixel size of images in CNN is 2^m (m is an integer), the images of porous structures made in Section A are downsampled to 128×128 pixels using kernel[217] before feeding to the CNN. Below we outline the different layers in the CNN. We focus on identifying the data flow as well as learnable parameters and their dimensions, but omit numerical implementation details as they are widely available in the literature.

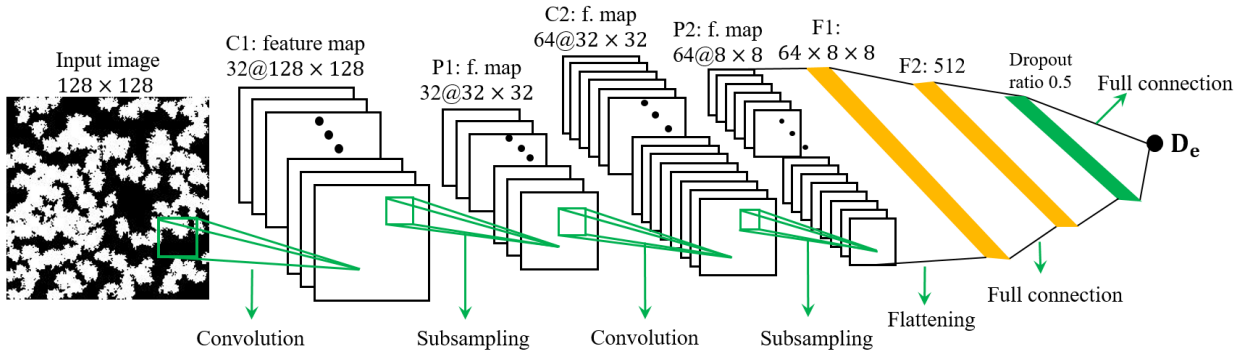

Figure 5-2. The architecture of our regular convolutional neural network (CNN) for predicting the effective diffusivity of 2D porous media from their images.

In this work, we adapt the CNN model have similar archietecture of the AlexNet,[209] Our CNN model has M pairs of convolutional and pooling layers and P fully-connected layers (M and P are both set to 2 in Fig. 5-2 for illustration purpose). When CNN is used in image-related studies as in this work, the ouput volume of a convolutional or pooling layer is typically termed *feature maps* as the purpose of these layers is to extract features from their input volume.[11, 20] For simplicity, the width of any input/ouput volume of convolutional/pooling layer is always equal to its height in this work. The number of slices of an ouput volume of a convolutional layer (d_o) is its depth. To obtain the δ-th slice of the feature map, $\mathrm{F.map}^{\delta}_{\mathrm{conv}}$, a filter is slided over every width and height position of the input volume and the result is the ouput for neuron at each position. By writing $\mathrm{F.map}^{\delta}_{\mathrm{conv}}$ as a $a_o \times a_o$ order-2 tensor (a_o is the width/height of the feature map), this operation can be written as

$$\mathrm{F.map}^{\delta}_{\mathrm{conv}} = \mathrm{ReLU}\left(W^{\delta} \otimes X_i + B(\delta) \cdot J\right) \tag{5-5}$$

where ReLU is the activation function adopted for the neurons in this work.[218] X_i is the input volume of the convolutional layer (for layers C1 and C2 in Fig. 5-2, X_i are the 2D binary image

and the feature map generated by the first pooling layer, respectively). X_i is a $a_i \times a_i \times d_i$ order-3 tensor, where a_i and d_i is the width and depth of the convolutional layer's input volume, respectively. W^δ is the kernel of the δ-th filter of the convolutional layer. It is a $s_\delta \times s_\delta \times d_i$ order-3 tensor, where s_δ is the filter's spatial extent in the width direction. $W^\delta \otimes X_i$ denotes the 2D-convolution of the filter kernel with the input volume, and its expression can be found in numerous textbooks.[219] $B(\delta)$ is the bias for the δ-th filter and J is a $a_o \times a_o$ order-2 tensor with all elements equal to 1.0. In Equation (5-5), W^δ and $B(\delta)$ $(\delta = 1, 2, \cdots d_o)$ must be "learned" during the trainning of CNN and they include a total of $\left(s_\delta^2 \times d_i + 1\right) \times d_o$ learnable parameters. On the other hand, a_o, s_δ, d_o, and the number of convolutional layers M are hyperparameters to be specified when building the CNN. Generally, the width and depth of the feature map must be large enough to ensure both short- and long-range features can be extracted but small enough to lower comptuational cost and suppress overfitting. In this work, the width of the output feaure maps of a convolutional layer is the same as its input feature map or image. The depth of feature maps geneated by the first and second convolutional layers in our CNN is taken as 32 and 64, respectively.

The feature map generated by each convolutional layer is feed into a pooling layer (see Fig. 5-2) to obtain a new feature map with the same depth but reduced width. The spatial span, stride, and type of filter used in the pooling layers are also hyperparameters that can be optimized through cross-validation. Here, we use the max pooling with a filter size of 4×4 and a stride of 4 to downsample the input feature maps.

The feature map generated by the last pooling layer is flatten into a vector ($\mathrm{X_{in,fc1}}$; length: $n_{\mathrm{in,fc1}}$). This vector is fed to the first fully connected layer with n_{fc1} neurons (see Fig. 5-2), which produces $\mathrm{F.map_{fc1}}$ through Equation (SC2) (supporting information) using a $n_{\mathrm{fc1}} \times n_{\mathrm{in,fc1}}$ matrix $\mathrm{W_{fc1}}$ as learnable weights and a vector $\mathrm{B_{fc1}}$ (length: n_{fc1}) as learnable biases. n_{fc1}, a hyperparameter, is taken as 512 in this work. To avoid overfitting, a dropout layer (dropout ratio = 0.5) is applied before the second fully connected layer. The output of the dropout layer is passed to the second fully connected layer to make the final prediction via

$$D_e^{CNN} = W_{fc2}X_{o,drp} + B_{fc2} \quad (5\text{-}6)$$

where D_e^{CNN} is the effective diffusivity predicted by CNN, $X_{o,drp}$ is output of the dropout layer, and W_{fc2} and B_{fc2} are the learnable weight and bias of the second fully connected layer, respectively.

In addition to the CNN above, we also test the deep residual network, Resnet50,[136] a more recent scheme of CNN (see Supporting Information). Because Resnet50 only performs slightly better than the above CNN but its structure is considerably more involved, below we present only the results based on the CNN outlined in Fig. 5-2. The implementation, results, and comparison of the Resnet50 with the above CNN model are summarized in the *Supporting Information*.

Using field knowledge to augment CNN model. A great advantage of CNN is that physical properties can be encoded into the CNN architecture to improve its final prediction. Because the effective diffusivity of a porous structure is strongly correlated with its porosity, following previous work,[135] we also combine the porosity with the flattened feature map of the last pooling layer to form the first fully connected layer in CNN. Specifically, the porosity of each porous structure is added as input to the first fully connected layer of the conventional CNN model with a fixed weight (a variety of weights have been tested with similar results, and a value of 10/4096 is used in the final model here).

Another method that can potentially improve the performance of CNN model is to preprocess the image of porous structures. As shown in Fig. 5-1a, for structures with low porosity (e.g., $\varepsilon < 0.5$), there exist many trapped areas and/or dead-end paths. These trapped regions are typically larger than the filter size used in the CNN model and thus can be difficult to extract directly using the CNN model. Moreover, the trapped regions are prone to provide faulty information to the feature map and induce noise during the learning process. In this work, before feeding to the CNN, images of porous structures are processed using the 8-connected component analysis[220-221] to eliminate all the trapped pore spaces (see Section III.C.2 for details).

Summary. The computation framework for predicting the effective diffusivity of porous structures from their images using CNN models can be summarized as four steps (see Fig. SC2):

(a) *Data generation:* Porous media with a wide variety of porosity and pore topologies are generated and their true effective diffusivity D_e (ground truth) is obtained using LBM simulations.

(b) *Augmenting CNN by field knowledge:* Trapped pore spaces are removed in the preprocessing step and physical properties of porous structure (porosity) are combined with feature maps built by the convolutional and pooling layers to serve as the input to the fully-connected layers in CNN.

(c) *Parameterizing CNN.* CNN's hyperparameters and learnable parameters are established through training and cross-validation using the training and validation datasets.

(d) *Deploying CNN.* Using the trained model in step (c) to predict effective D_e of porous media using their images as input.

C. Parameterization of convolutional neural networks

After the datasets are generated and CNN model is set up, we first need to select all hyperparameters in the CNN model. A CNN model has many hyperparameters such as the choice of the activation function, size of the feature map produced by each convolutional/pooling layer, etc. Although it is desirable to select all parameters through cross-validation, doing so requires prohibitively high computational cost. Therefore, many of these parameters are selected empirically. While this is not a rigorous approach, researches in image classification show that the performance of CNN models is often insensitive to the selection of many hyperparameters. These researches suggest that the number of convolutional layers and the spatial extent (size) of the filters used in these layers usually play the most important role in CNN. Hence, in this work, CNN models with different number of convolutional layers ($\mathrm{M} = 2, 3, 4$) and different filter sizes in the convolutional layer ($\mathrm{s} \times \mathrm{s} = 3\mathrm{x}3, 5\mathrm{x}5, 7\mathrm{x}7$) are evaluated. Other hyperparameters used in the model can be found in Section II.B.2.

We next optimize the weights and biases for all filters in each convolutional and fully connected layer by "learning" the training dataset. The proposed CNN model is implemented in the machine learning framework Tensorflow.[222] The loss function L, which quantifies how well the CNN reproduces the training dataset, is defined as the average mean square error over the entire training dataset

$$L = 1/N \sum_{i=1}^{N} \left(D_{e,i}^{LBM} - D_{e,i}^{CNN}\right)^2 \quad (5\text{-}7)$$

The weights of all filters are initialized using a truncated normal distribution with a standard deviation 0.1. All biases are set to 0.1 initially. The training model is converged through minimizing the loss function by the Adam Optimizer[223] with a learning rate $\gamma = 10^{-4}$. The training model stops at 1600 epochs. The optimized weights and biases for all learnable filters at the last epoch are saved in the trained model. The saved model will then be restored for evaluating the testing dataset without redoing the training process.

5.3. Results and Discussions

In this section, we first examine how key hyperparameters affect the performance of CNN models using cross-validation. We next present the performance of the regular CNN and compare it with that of a classical empirical model. Then, the performance of field knowledge-informed CNN on a wide range of porous structures is evaluated.

Table 5-1. The mean square error of CNN models with different hyperparameters obtained during cross-validation.

Number of convolutional layers	Filter size ($s \times s$)		
	3×3	5×5	7×7
2 layers	1.38×10^{-4}	8.76×10^{-5}	7.51×10^{-5}
3 layers	4.44×10^{-4}	1.09×10^{-4}	1.13×10^{-4}
4 layers	2.14×10^{-3}	6.17×10^{-4}	-

A. Cross-validation for hyperparameters selection

A trained CNN model often can fit the training dataset used to parameterize it well, but may not perform well on other datasets due to overfitting. To reduce overfitting of the trained model, one usually optimizes hyperparameters of the CNN model through cross-validation. Here, we systematically vary the number of convolutional layers and the filter size in the CNN and cross-validate the trained model using the validation dataset generated in Section II.A. Table 5-1 summarize the mean square error (MSE) of the effective diffusivity predicted by the CNN model

with relative to the true value. We observe that, for a fixed filter size, MSE is smaller for CNN models with fewer convolutional layers. For CNN models with the same number of convolutional layer, the MSE is highest when the filter size is 3×3, likely because the narrow filters cannot capture some important features spanning moderate to large number of pixels. The MSE is comparable for models with a filter size of 5×5 and 7×7. Because the computational cost is higher when filters with 7×7 size are used, we adopt the CNN models with 2 convolutional layers and a filter size of 5×5 (see Fig. 5-2).

B. Performance of the regular CNN model

The performance of the regular CNN model, in which field knowledge is not encoded, is evaluated using the testing dataset. For each porous structure described by a 128×128 binary image, its effective diffusivity is computed by the trained model using ~1.5×10^8 FLOPs of calculations. This cost is close to the cost of multiplying two 400×400 matrices and requires ~4 ms on a laptop (Intel CPU 6600, 3.3 GHz, 8 GB memory, single core). As a comparison, computing the effectivity diffusivity using LBM requires ~ 1 hour on the same computer. Therefore, the computational cost of the CNN model is roughly six orders of magnitude smaller than the LBM simulations.

Table 5-2. The mean square error and mean truncated relative error of the various CNN models

	Regular CNN trained using the loss	Regular CNN trained using the loss	Porosity-informed CNN	Regular CNN with preprocessed
Mean	8.64×10^{-4}	7.01×10^{-4}	7.64×10^{-4}	6.92×10^{-4}
Mean	68.8%	41.7%	59.2%	29.7%
R^2	0.9903	0.9921	0.9914	0.9912

The mean square error (MSE) of the effective diffusivity of porous structures in the entire testing dataset is found to be 8.64×10^{-4} (see Table 5-2). Since the porous structures feature diverse pore shape/topology and their effective diffusivity spans ~10^{-10} to 1.0, such a small MSE

suggests that the CNN model performs well for the complex porous structure examined here. Figure 5-3a further compares the effective diffusivity predicted by the CNN model and computed by LBM codes, and we observe that the CNN model's overall performance is again very good. It is worthwhile to compare the performance of the CNN model with that of empirical correlations. The Bruggeman equation has been widely adopted in predicting the effective diffusivity of porous structure and is given by $D_e = \varepsilon/\tau$ (ε: porosity, τ: tortuosity). The tortuosity of porous media is commonly modeled using $\tau = \varepsilon^{-\beta}$. Hence, the Bruggeman equation predicts

$$D_e = \varepsilon^{\beta+1} \tag{5-8}$$

The parameter β depends on the structure of porous media, e.g., the connectivity of pores. β is equal to 0.5 for porous media made of packed spheres and is otherwise an empirical parameter that is strongly correlated with the tortuosity of the porous media.[18, 224] Here, β is taken as 2.0 because it describes the scaling of D_e at large porosity relative well. Figure 5-3a compares the prediction of the Bruggeman equation with the LBM prediction. When the true D_e is larger than ~0.6, the Bruggeman equation performs as well as the CNN model. However, as the true D_e becomes smaller, which is mostly caused by the emergence of more tortuous transport pathway in the porous media, the Bruggeman equation systematically overpredicts the effective diffusivity and performs worse than the CNN model. Therefore, the CNN model can better capture the transport properties of porous media with complex structure than the Bruggeman equation.

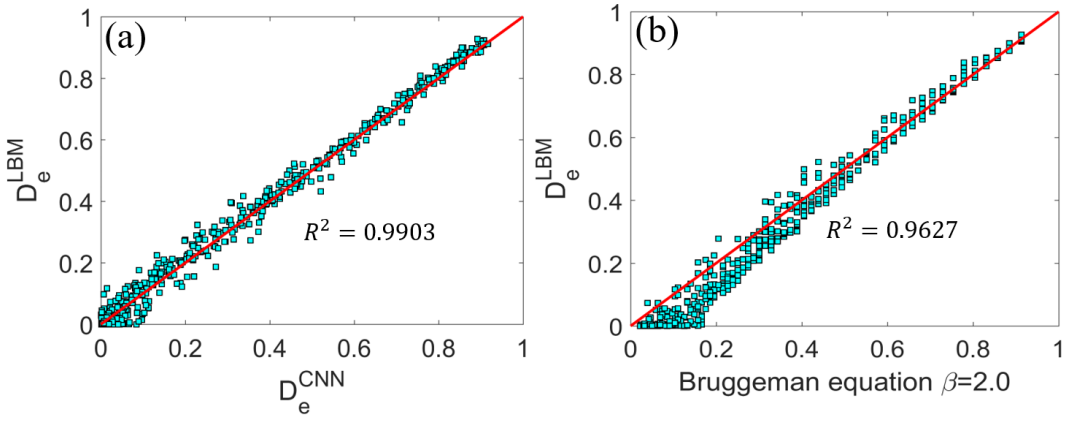

Figure 5-3. Effective diffusivity predicted by the CNN model (**a**) and the empirical Bruggeman equation (**b**).

We next quantify the predictive power of the CNN model *posteriori* systematically. Because the performance of the CNN model depends on the effective diffusivity of porous structure (see Fig. 5- 4a), the porous structures in the testing dataset are divided into three groups: those with $D_e < 0.1$, those with $0.2 < D_e < 0.6$ and those with $D_e > 0.6$. The top row of Fig. 5-4 shows the distribution of the absolute error of D_e predicted by the CNN model. In each group, over 95% of predictions have absolute error smaller than 0.1. Furthermore, the distribution of the absolute error is similar for all groups, which suggests that, during the training of the CNN model, the characteristics of all three groups are "learned" by the model.

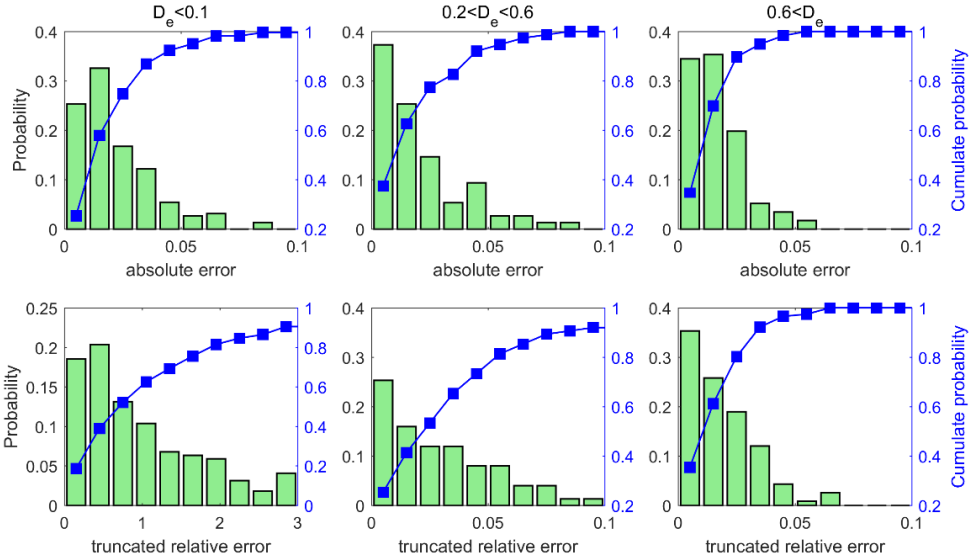

Figure 5-4. Distribution of the absolute error (top panels) and truncated relative error (lower panels) of the predictions of the CNN model for the porous structures in the testing dataset with $D_e < 0.1$, $0.2 < D_e < 0.6$ and $D_e > 0.6$. The CNN model is trained using the loss function based on the mean square error.

Another way to characterize the CNN model's predictive power is to study the relative error of its predictions. The standard calculation of relative errors, however, is not necessarily a good approach for the porous media studied here. Specifically, because many of our porous structures have extremely small D_e (e.g., 10^{-10}, see Fig. 5-1), a minute error in their D_e can correspond to an enormous relative error even though such minute error has little practical impact on the prediction of transport in the porous media. While there is no unique way to address this issue, we

define a truncated relative error, TRE, as

$$\mathrm{TRE} = \begin{cases} \frac{|D_e^{\mathrm{LBM}} - D_e^{\mathrm{CNN}}|}{D_e^{\mathrm{LBM}}} & (\text{if } \mathrm{D_e^{LBM}} > \mathrm{D_e^{thsd}}) \\ \frac{|D_e^{\mathrm{LBM}} - D_e^{\mathrm{CNN}}|}{\mathrm{D_e^{thsd}}} & \left(\text{if } \mathrm{D_e^{LBM}} < \mathrm{D_e^{thsd}}\right) \end{cases} \tag{5-9}$$

where D_e^{LBM} and D_e^{CNN} are the predictions by the LBM simulations (taken as ground truth here) and the CNN model, respectively. In this definition, only inaccuracy comparable to or larger than a threshold D_e^{thsd} (taken as 0.01 hereafter to be specific) is thought to affect the practical application of the D_e computed for the porous structure (e.g., in the prediction of pore clogging during the discharging of Li-air electrodes). Analysis of the predicted D_e shows that the mean truncated relative error is 68.8% for the entire testing dataset (see Table 5-2). The bottom row of Fig. 5- 4 further shows the distribution of the truncated relative error for the three groups of porous structure in the testing dataset. We observe that the truncated relative error is the larger in samples with smaller D_e: for samples with $0.2 < D_e < 0.6$, ~95% of the CNN predictions have a truncated relative error less than 10%; for samples with $D_e < 0.1$, ~60% of the CNN predictions have a truncated relative error less than 100%. These observations are consistent with the above observation that the magnitude of the absolute error similar among samples with different D_e.

The larger relative error in samples with small D_e is expected because the regular CNN model is trained to minimize the MSE (i.e., a measure of the absolute rather than relative error) over the training set. To explore whether the CNN model can be tailored to give smaller relative errors (especially in samples with $D_e < 0.1$), we define a new loss function for training the CNN model as

$$L = 1/N \sum_{i=1}^{N} (TRE_i) \tag{5-10}$$

where N is the number of porous samples in the training dataset, TRE_i is the truncated relative error for each training data, which is defined in Eqs. (5-11). Training of the CNN model based on this loss function is able to converge. The CNN thus trained gives a truncated relative error of 41.7%

when applied to the samples in the testing dataset, which is moderately better than that of the regular CNN model (68.6% see Table 5-2). Interestingly, the MSE of the new model (7.01×10^{-4}) is also slightly smaller than that of the regular CNN model (8.64×10^{-4}). This result indicates that the choice of the loss function during the training of a CNN model also affects how effectively the trained model performs, presumably because the tradeoff between how well the model is fitted for porous structures with low and high D_e is shifted when different loss functions are used. The latter is evident when predictions by the newly trained CNN model is compared against the LBM predictions. As shown in Fig. 5-5a, compared to the regular CNN model, the new model performs better for samples with $D_e < 0.2$ but worse for samples with $D_e > 0.8$. These observations are corroborated by the distribution of the absolute errors in the three groups of samples in the testing dataset (see Fig. 5-5b, upper panels). The improved performance of the CNN model for samples with low D_e is also evident in the distribution of the truncated relative error (see Fig. 5-5b, lower panels), e.g., for samples with $D_e < 0.1$, 85% of the predictions by the new CNN model is within a truncated relative error of 100%.

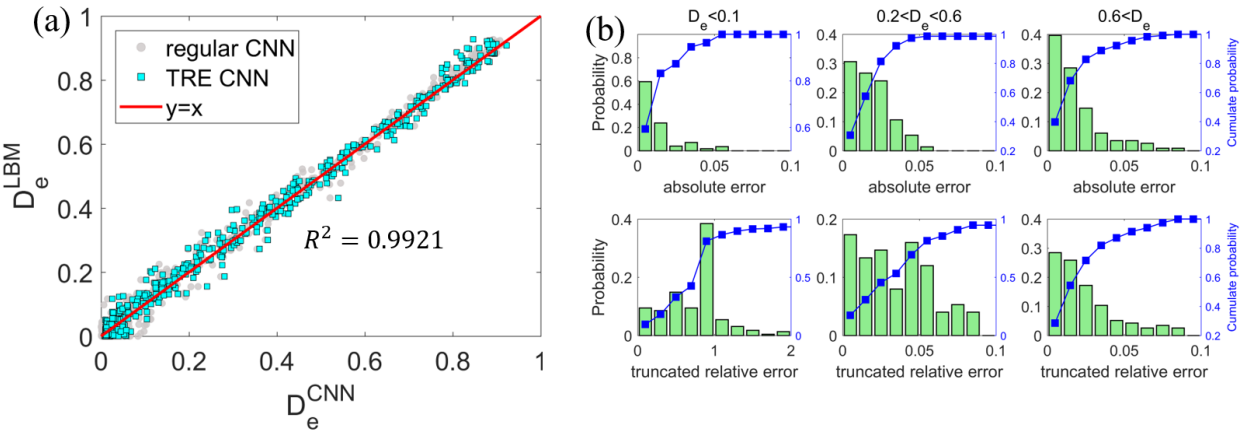

Figure 5-5. (**a**) The effective diffusivity predicted by the CNN model trained using a loss function based on the truncated relative error (Equation (5-9-5-10)). (**b**) Distribution of the absolute error (top panels) and truncated relative error (lower panels) of the predictions of the CNN model for the porous structures in the testing dataset with different D_e.

C. Improving CNN models using field knowledge

C.1. Porosity-informed CNN model

In the previous section, we demonstrate that the CNN model performs well for porous

structures with a wide range of porosity. Note that the key features determining the effective diffusivity of a porous structure are extracted through the convolutional layers and these features are mostly connected with the input images locally. Therefore, global features or features spanning large scale may not be effectively extracted using the CNN, which may compromise the predictive power of the CNN. Therefore, it may be useful to directly introduce physical parameters describing these features into the CNN model to improve its performance. As described in Section II, here we introduce the overall porosity of the porous media as an input to the first fully connected layer in the CNN. Although the complex porous structures spanning large scales are not easy to identify using CNN models, they can be easily identified based on knowledge of porous media.

The predictions of the porosity-informed CNN model are only marginally improved compared to the regular CNN, e.g., both the MSE and truncated relative error for the testing dataset are smaller than those of the regular CNN by about 12% (see Table 5-2). This is also evident in Fig. 5-6, where the CNN predictions for the entire testing dataset are shown. In particular, we observe that the limitations of the regular CNN model for porous structures with $D_e \lesssim 0.1$ are not greatly alleviated in the new model. The limited improvement of the new model may originate from several sources. First, porosity is not a reliable indicator of D_e, especially for porous structures with low D_e (see Fig. 5-3b), because the transport is hindered also by complex features such as dead-end transport pathways and trapped space beyond the overall amount of pore space. Second, though porosity is added as additional neurons in the CNN, their impact may have already been captured in the feature maps generated by the filters in the convolutional layer. In this case, the input due to porosity is redundant and thus does not improve the performance of the CNN.

C.2. The CNN model using preprocessed porous structure as input

The CNN model illustrated in the previous sections works well for porous media with moderate to large diffusivity ($D_e > 0.2$) but exhibits relatively large error for porous samples with very small diffusivity (e.g., $D_e < 0.1$). This is closely related to the more complex transport behavior in porous media with very small diffusivities: in these media, the diffusion pathways are tortuous and there exist many trapped pores and dead-end paths. Since CNN models may not

effectively extract features of these complicated structure spanning relatively large length scales using filters with small spatial extent, they do not perform well for such porous media. Nevertheless, these complex features are easily discerned based on field knowledge of porous media. Hence, here we explore the possibility of improving CNN prediction by processing the images of porous structures to remove dead-end and trapped pore spaces.

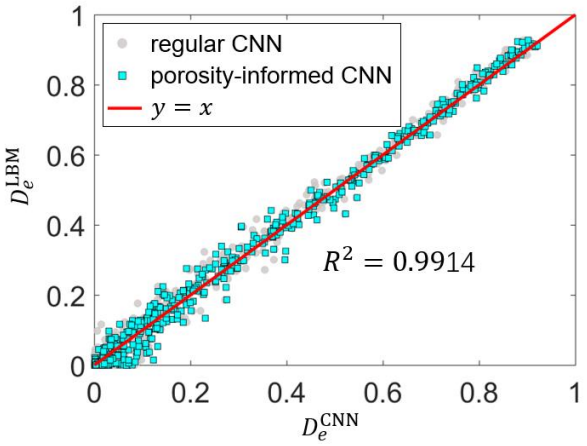

Figure 5-6. The effective diffusivity predicted by the porosity-informed CNN model.

To improve the CNN prediction for porous media with small D_e, *all* datasets are optimized by removing the trapped and dead-end pore spaces. First, each binary image of the porous structures is labeled using 8-connected component labeling method[220-221] with periodic conditions on the top and bottom side (see Fig. 5-7a). This labeling method is consistent with LBM simulations based on the D2Q9 scheme, where each target position is associated with the nearby 8 directions. Next, in each labeled image, all components with labels across the inlet and outlet of the porous structure are kept, while other components (trapped pores and dead-end pores) are eliminated. Afterward, the porous structure is reconstructed with the remaining pore space as the effective pore space and the rest as the solid space. Figures 5-7a and 5-8b show a porous structure before and after the preprocessing described above. Clearly, although there exists large pore space in the regular porous structure, only part of it is available for molecular transport. Finally, the CNN model is trained using the preprocessed binary images and their corresponding D_e.

Using the CNN model trained above, we again calculated the effective diffusivity of the porous samples in the testing dataset from their preprocessed images (see Fig. 5-7c). Overall, the

new predictions are in good agreement with the LBM predictions. As shown in Table 5-2, the MSE of the CNN predictions is 6.92×10^{-4}, which is 20% smaller than that of the regular CNN model. The mean truncated relative error is reduced from 68.8% in the regular CNN predictions to 29.7%. Examination of the distribution of the absolute and truncated errors of the predictions (see Fig. 5-7d) shows that the predictions are improved considerably for porous samples with $D_e < 0.6$, e.g., for samples with $D_e < 0.1$, over 70% of the predictions are within a truncated relative error of 20%. Therefore, leveraging field knowledge can help improve the predictions of the CNN model.

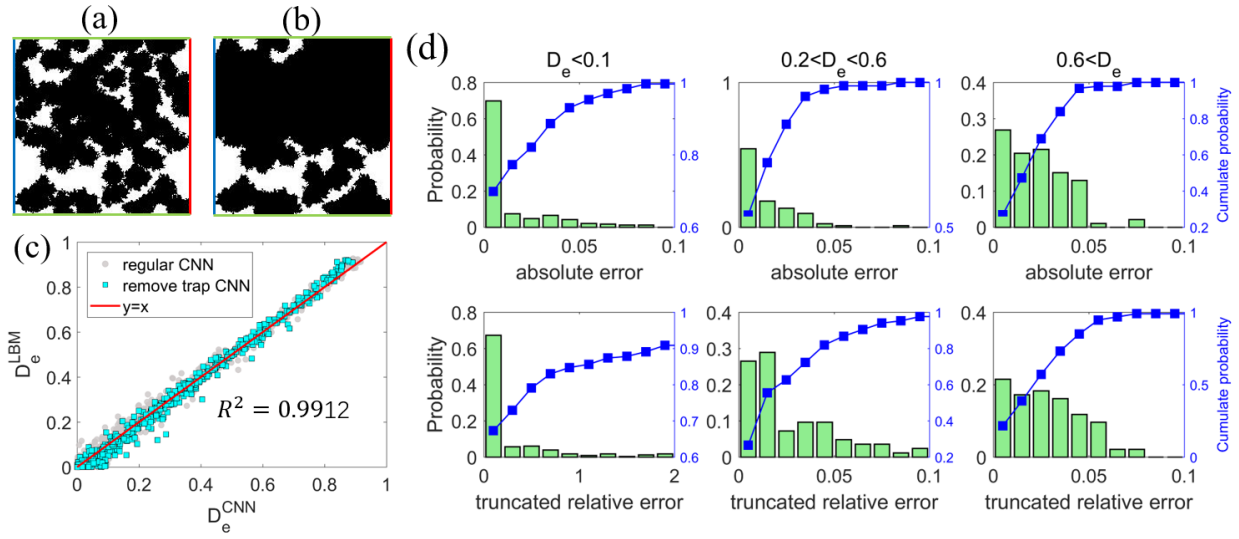

Figure 5-7. *Improving CNN prediction by preprocessing images of porous structures.* (**a-b**) Images of the regular (a) and processed (b) porous structure by removing the trapped pore space and dead-end transport pathways. The blue (red) lines on denote the inlet (outlet) of the molecule transport through the porous structure. The green lines denote the periodic boundaries. (**c-d**) The effective diffusivity predicted by the CNN model using the preprocessed image of porous structures (c) and the distribution of their absolute and truncated relative errors (d).

Even with the above improvement, for porous samples with $D_e < 0.1$, ~10% of the CNN predictions still have a truncated relative error >200%. Examination of these data points revealed that the true D_e of the corresponding samples is very small ($\lesssim 10^{-4}$) but the CNN prediction are much higher. In these porous samples, only a few diffusion pathways contribute to the net diffusion flux. A representative case is shown in Fig. 5-7a-b. Although there is a large amount of pore space in the original porous sample (Fig. 5-7a), only a single diffusion path is found after the trapped pore spaces are identified (Fig. 5-7b). The net transport through these porous samples is thus

dictated by a few narrowest throats along the long, tortuous pathway. Therefore, to accurately predict the effective transport property, both global feature (tortuous pathway) and local feature (critical throats) need be captured by the CNN model. This need can be difficult to meet by the convolutional layers, which retrieves relatively *local* characteristics of the porous structure. Indeed, similar situations are also frequently encountered in direct simulations of transport phenomena exhibiting multiple length and time scales (e.g., turbulent flows). Second, the number of samples having the above challenging geometrical features is limited and outweighed by other samples in the training dataset. Therefore, these features are likely not extracted accurately in the CNN model.

5.4. Conclusions

In summary, inspired by recent works on application of machine learning in porous media research, we develop deep learning models based on CNN for predicting the effective diffusivity of 2D porous media from their binary images. The computational cost of the model is six orders of magnitude lower than direct pore-scale calculations. The performance of the deep learning model is evaluated in detail by computing the mean square error, mean truncated relative error, and distribution of absolute and truncated relative errors for samples with different effective diffusivity. The effective diffusivity of realistic porous media spanning more than one order of magnitude ($0.1 \lesssim D_e < 1$) can be predicted well even when the porous media contain complex and diverse topologies and have large variation of porosity (0.28-0.98). The performance of the deep learning model, especially when applied to porous media with $D_e \lesssim 0.1$, can be improved by training the model using a loss function based on the truncated relative error or preprocessing images of porous media to remove the trapped pore space and dead-end transport pathways. Improvement due to incorporation of porosity of porous media into the CNN, however, is marginal.

Our results demonstrated that the transport properties of realistic porous media with diverse/complex topologies can be predicted with good accuracy and little computational cost. While only 2D porous structure is considered here, extension of the model to 3D situations is possible given that CNN can handle high dimensional data effectively. Indeed, the recent success of extending 2D CNN model to 3D for human pose and gesture recognition[225-226] and medical

image process problems[227] suggests that CNN can be highly effectively in tackling 3D problems. Nevertheless, there may exists caveats that makes CNN less effective in 3D than 2D for the transport in complex media, and extensive tests must be performed to confirm the feasibility of CNN in predicting the transport properties of 3D porous media.

Although all datasets are generated computationally here for generic porous materials, these data can also be generated experimentally for specific porous materials, e.g., porous structures can be built from CT-scan and X-ray microtomography,[228-230] and effective transport properties such as diffusivity and thermal conductivity can be measured experimentally. The experimentally generated data can be used to inform the computational reconstruction of porous structures for specific classes of porous materials (e.g., shales or ceramic matrix composites) and validate predictions of pore-scale simulations, thereby enabling the creation of high-fidelity computational models of many classes of materials. The creation of these models and pore-scale simulations of them by high-performance computing will produce large, high-quality datasets tailored to different classes of porous materials. Deep learning models based on these datasets will enable fast and accurate prediction of the properties of these materials and benefit their applications. These potential extensions of the present work, along with the predictive power of the CNN models demonstrated here, suggest that deep learning can be a powerful new tool in the future research of porous media.

The analysis of the performance of our current model points to the origins of its current limitations and directions for future development. Our present model does not perform very well when the porous media has a very low effective diffusivity. Such a limitation may be addressed through two possible approaches: *multiscale feature extraction* and *encoding of advanced geometrical properties*. Because the transport in low effective diffusivity porous media is often dictated by a few narrow throats along a few (or even just one) tortuous pathway, the accurate prediction of transport by deep learning models requires the geometrical features at both global and local scale to be extracted effectively and properly weighed during training. Research on multiscale feature extraction can likely benefit from work on feature extractions from complex

systems such as turbulent flows. Another way to simultaneously consider both the local and global structure of porous media is to directly encode information of such structure into the deep learning model, thereby bypassing the need to extract them using the convolutional layers. For example, given the importance of pore connectivity and pore size distribution in the transport in porous media, quantitative measures of these properties may be encoded into the deep learning model in the future. Identifying the best information to encode into deep learning models will benefit from the immense field knowledge on transport in porous media accumulated by the community over the past decades.

Supporting Information

All supporting information cited in this chapter is located in Appendix C.

Chapter 6. Reconstructing Heterogeneous Composites by Deep Learning

Disclosure:

This work has been accepted for publication by the American Institute of Physics: Wu, H.; Zhang, H.; Hu, G.; Qiao, R., Deep Learning-Based Reconstruction of the Structure of Heterogeneous Composites from Their Temperature Fields, AIP Advances, 2020, DOI: 10.1063/5.0004631

6.1. Introduction

Inverse problems involving transport phenomena are ubiquitous in engineering design, optimization, and diagnosis. Common applications include finding the configuration of systems and the properties of systems' materials to achieve the desired transport behavior, e.g., what structure and loading should be adopted for the constituents of a thermal composite so that it provides the required thermal conductivity. Monte Carlo (MC)-based techniques have traditionally been used to solve inverse problems.[139-140] However, these techniques tend to be computationally expensive because a large number of realizations are often needed to obtain accurate results in large parameter space.[141] Many new methods have been developed to lower the computational cost for solving inverse problems. For example, surrogate models have been constructed via generalized polynomial chaos expansion to perform inverse uncertainty quantification of thermal-hydraulic problems[231] and Gaussian process regression-based inverse models have been used to estimate the thermal properties of orthotropic materials.[142] However, these models often have difficulty in scaling to high dimensional inverse problems, in which the input fields are high dimensional.

Machine learning-based techniques can potentially be an effective approach for tackling the above difficulties. In particular, one branch of machine learning, deep learning, is gaining popularity in many disciplines (e.g., computer vision[215, 232] and natural language processing[233-234]) and has shown promise in solving transport phenomena in complex systems.[129-131] For example, surrogate model based on the deep convolutional encoder-decoder networks have been used for uncertainty quantification in single-phase flow[132-133] and deep learning models with variational

auto-encoder have been applied for the uncertainty quantification in reservoir simulations.[235] Convolutional neural network (CNN) has been used to predict the effective transport properties of porous media with complex structure with computational cost orders of magnitude lower;[135, 145-147] deep neural networks (DNN) have been used to predict the multiphase flow in heterogeneous media.[144] Nevertheless, the applications of deep learning methods for inverse problems involving transport phenomena in heterogeneous media are still limited. There also exist some conceivable challenges when deep learning is used in such problems. To ensure accuracy, deep learning-based models often require a large amount of input data, which is difficult or expensive to obtain in practice. Furthermore, obtaining fine-grained input data also needs a large number of sensors to be deployed. As suggested by recent works on sparse sensor placements for signal reconstruction[149] and fluid flow reconstruction from limited measurements,[150] a large number of sensors can potentially modify the data to be measured, thereby introducing systematic error into the model prediction. Therefore, whether and to what extent coarse-grained input data can be used effectively in deep learning to solve inverse problems involving high-dimensional data (e.g., when heterogeneous media are involved) remains a critical but open question.

In this work, we develop a deep learning-based model to predict the heterogeneous structure of a thermal composite from the composite's temperature fields. For composites, "heterogeneous" can be interpreted in three ways: (1) the spatial distribution of fillers is not homogeneous (e.g., fillers are randomly, rather than homogeneously, distributed within a matrix), and (2) the fillers are irregular in shape and size, and (3) fillers with irregular shape/size are distributed in a non-homogeneous fashion in a matrix. Here, we focus on the first kind of heterogeneity. Specifically, circle-shaped fillers with high thermal conductivity are dispersed randomly in a matrix with low thermal conductivity. We note that circle-shaped fillers are common, e.g., the cross-section of carbon nanotubes is circular and spherical solid particles are often used in thermal composites. Because both the input and output data of this inverse problem can be high-dimensional, we adopt the end-to-end image-to-image regression by using the convolutional encoder-decoder network (U-Net). Conceptually, the encoder network extracts important spatial correlations from the

temperature fields, which is then used as an input for the decoder network to predict the heterogeneous structure of the composite. The proposed model is trained and tested in two-dimensional (2D), highly heterogeneous composites using computationally generated datasets. We also investigate the model's performance and its improvement when sparse temperature field is used as input. Finally, we use the uncertainty of the model's predictions to guide the placement of additional temperature sensors, whose measurement helps improve the predictions of the deep learning model.

The rest of the manuscript is organized as follows: In Section 2, we introduce the definition of the inverse problem considered here and the generation of datasets for the deep learning model. In Section 3, we present our deep learning model based on the convolutional encoder-decoder networks for solving the inverse problem. In Section 4, the performance of the developed model is examined and discussed. The discussion and conclusions are provided in Sections 5 and 6.

6.2. Problem Definition and Dataset Generation

Thermal composites are heterogeneous materials in which fillers with high thermal conductivity are dispersed in a base matrix with low thermal conductivity. In forward problems related to these materials, the temperature field (and consequently the effective thermal properties) of the composites is predicted using the distribution of the fillers in the base matrix and the thermal conductivity of the fillers and base matrix as input. In inverse problems, the composite's temperature field is used as input to determine other observables of interest, e.g., the distribution of fillers and their thermal conductivity. Here, we consider an inverse problem in a 2D square composite with randomly distributed fillers (see Figure 6-1). The blue circles and the gray background represent the fillers and the base matrix, respectively. The temperature field measured at selected points in the composites is used as input to infer the distribution of the fillers in the matrix. We solve this inverse problem with a data-driven deep learning-based model. Below, we first define a data-driven model for solving this problem. We then will present the numerical method for generating the datasets that are needed for our deep learning model.

6.2.1. Deep learning-based model

Without losing generality, we consider a square-shaped composite (see Fig. 6-1). The base matrix and fillers have uniform thermal conductivity within them. Thus the composite is characterized by a binary thermal conductivity field $k(\boldsymbol{x})$. The 2D heat conduction within the composite is governed by

$$\nabla \cdot \big(k(\boldsymbol{x})\nabla T(\boldsymbol{x})\big) = 0, \quad 0 < x, y < 1 \tag{6-1}$$

with boundary conditions

$$\frac{dT}{dy}|_{y=0} = \frac{dT}{dy}|_{y=1} = 0 \tag{6-2a}$$

$$-k\frac{dT}{dx}|_{x=0} = q_0''; \;\; T|_{x=1} = T_1 \tag{6-2b}$$

Here, $T(\boldsymbol{x})$ is the temperature field, which serves as the input of our inverse problem. $k(\boldsymbol{x})$ is the binary thermal conductivity field in the composite, which is the desired output of our inverse model.

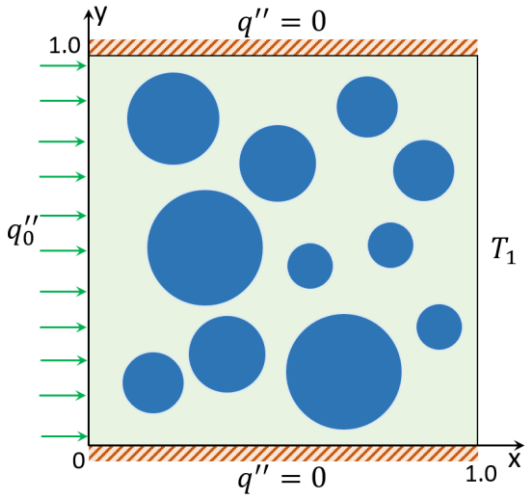

Figure 6-1. A two-dimensional composite with a binary thermal conductivity field $k(\boldsymbol{x})$ (blue circles: fillers with high thermal conductivity; gray background: base matrix with low conductivity). The goal of the inverse model is to predict $k(\boldsymbol{x})$ from the temperature field measured in the composite under the labeled boundary conditions.

Mathematically, the above problem is a special case of a more general problem governed by

$$\mathcal{L}\big(k(\boldsymbol{x}); T(\boldsymbol{x})\big) = 0, \quad \boldsymbol{x} \in \Omega \tag{6-3a}$$

$$\mathcal{B}\big(T(\boldsymbol{x})\big) = b(\boldsymbol{x}), \quad \boldsymbol{x} \in \partial\Omega \tag{6-3b}$$

where $\mathcal{L}$ is a differential operator, $k(\boldsymbol{x}) \in \mathbb{R}^{d_k}$ is the output feature of interest at a spatial location $\boldsymbol{x} \in \Omega \subset \mathbb{R}^{d_x}$ (d_x is the dimension of the space, and it can be 1, 2, or 3). $T(\boldsymbol{x}) \in \mathbb{R}^{d_T}$ is the input field, whose dimension d_T may differ from the spatial dimension (e.g., input data measured by sensors are available only on a 2D surface). $\mathcal{B}$ defines the boundary conditions of the physical processes occurring on the domain boundary $\partial\Omega$. Both the input and output fields of this type of inverse problem are high dimensional. For the problem shown in Fig. 6-1, if the binary thermal conductivity $k(\boldsymbol{x})$ at $k \times k$ points within the square domain is to be predicted from the temperature $T(\boldsymbol{x})$ measured at $m \times m$ points in the domain, then $T(\boldsymbol{x})$ and $k(\boldsymbol{x})$ are vectors of length m^2 and k^2, respectively, i.e., $T(\boldsymbol{x}) \in \mathbb{R}^{m^2}$ and $k(\boldsymbol{x}) \in \mathbb{R}^{k^2}$. The inverse problem can be treated as a mathematical mapping:

$$\hbar\colon\ T(\boldsymbol{x}) \to k(\boldsymbol{x}) \ \ (\mathbb{R}^{m^2} \to \mathbb{R}^{k^2}) \tag{6-4}$$

Usually, obtaining the above mapping is computationally expensive. To tackle this limitation, we adopt an inverse model $\hat{k}(\boldsymbol{x}) = f(T(\boldsymbol{x}), \theta)$ to approximate the exact mapping of the physical systems $k(\boldsymbol{x}) = \hbar(T(\boldsymbol{x}), \boldsymbol{x})$, where θ represents some model parameters. The model f is trained using N sets of data $\mathfrak{D} = \{T^i(\boldsymbol{x}), k^i(\boldsymbol{x})\}_{i=1}^{N}$ through the minimization of a loss function *Loss*

$$f = \arg\min_{\theta} \Big(Loss\big(f(T(\boldsymbol{x}), \theta); k(\boldsymbol{x})\big)\Big) \tag{6-5}$$

6.2.2. Generation of datasets

In this work, the datasets used for training, validating, and testing the deep learning model for solving the inverse problem include the temperature and the binary thermal conductivity fields. These data are presented in the form of images. For each dataset, we first build a square with 128×128 pixels to represent the composite. Circles with a radius of 10-26 pixels are placed within the square at random positions. The area covered by the circles (fillers) is 30-70% of the square's area. The pixels occupied by the filler and base matrix are marked as 1 and -1, respectively. Next, we compute the temperature field in the heterogeneous structure generated under the boundary

conditions in Eq. 6-2 and continuous heat flux and temperature at filler-matrix interfaces. Without losing generality, we set q_0 to 4000 W/m^2 and $T_1 = 300$K. The thermal conductivities of the filler and the base matrix are set to 200 and 4 W/(m·K), respectively. Eq. 6-1 is solved using the finite volume method. The temperature values are scaled to $T \in [0\ \ 255]$ and stored as grayscale images.

Using the method described above, we generate 1200 datasets. These datasets are randomly divided into the training dataset (60% of the entire dataset), the validation dataset (23.3%), and the testing dataset (16.7%). The training dataset is used to optimize the model f in Eq. 6-5. The validation dataset is used to tune the hyperparameters in the deep learning model and avoid overfitting. The testing dataset is used to evaluate the performance of the trained model.

6.3. Deep Convolutional Encoder-decoder Networks (U-Net)

We adopt the deep convolutional encoder-decoder network (U-Net) model to solve the inverse problem defined in Section 2. Conceptually, this model consists of an encoder network and a decoder network. The encoder network is used to extract important spatial correlations and features from the temperature fields and is constructed from deep CNN. The decoder network takes the extracted features as input and projects the feature maps to high dimensional space to predict the heterogeneous structure of the composite (i.e., the binary thermal conductivity field). The decoder network is constructed with the transposed convolution layers to up-sample the feature maps to high dimensional space. Below, we first briefly introduce the basic operations in CNN. We next present the transposed convolutional operation and its difference from the convolutional operation. We then present the architecture of our U-Net model and summarize the computational framework of using U-Net to predict the heterogeneous structure of composites.

6.3.1. Deep convolutional neural networks

Detailed descriptions of the classical and convolutional neural networks and their data flow, written in a way that is easily accessible for researchers with computational transport phenomena background, can be found in our recent work.[137] Here, we only briefly outline the key idea of these

networks. A neural network approximates an input-output relation $\hbar$: $\mathcal{X} \rightarrow \mathcal{Y}$ via a series of layers with an affine transformation followed by a nonlinear activation function. For example, the k^{th} layer of a neural network processes the output of its preceding layer $\mathcal{Z}^{k-1}$ by first assigning weights and biases to this output and then passing the results to an activation function to generate its output $\mathcal{Z}^k$:

$$\mathcal{Z}^k = \mathcal{g}^k(W^k\mathcal{Z}^{k-1} + B^k) \tag{6-6}$$

where W^k and B^k are the weight matrix and bias vector (called the learnable parameters) for this layer, respectively. $\mathcal{g}^k(\cdot)$ is an elementwise nonlinear activation function, such as the tanh function or the rectified linear unit (ReLU) function. For an *N*-layer neural networks, its input and output are $\mathcal{X} = \mathcal{Z}^0, \mathcal{Y} = \mathcal{Z}^N$, respectively. Classical neural networks are fully connected (i.e., a neuron in an arbitrary layer *k* is connected to all neurons in its previous layer) and W^k and B^k are different for each layer. Therefore, as the number of layers and the dimension of the input increase, the number of learnable parameters increases drastically, resulting in enormous computational cost.

CNN is designed to reduce the learnable parameters of neural networks greatly.[236-237] This is achieved by connecting neurons in a layer *k* only to some neurons in layer *k*-1 and sharing learnable parameters for all neurons in the same convolutional layer. When CNN is used in image processing, a series of convolution kernels are applied to compute the output volume, which is termed *feature maps* (as the purpose of a convolutional layer is to extract important features from the input volume). Typically, the number of channels of the feature map is the depth of the output volume of a convolutional layer. For example, consider a convolution layer with an input volume $\mathcal{X}_i \in \mathbb{R}^{x_i \times x_i \times d_i}$, where $x_i \times x_i$ is the size of each feature map and d_i is the depth of the volume. To obtain the β-th feature map ($\mathrm{F.map}^{\beta}_{\mathrm{conv}}$), the β-th filter $W^{\beta} \in \mathbb{R}^{s_\beta \times s_\beta \times d_i}$ (s_β: kernel size; d_i: the number of filters) is slided over the input volume and the results is combined with the β-th bias B before passing to the nonlinear activation function $\mathcal{g}(\cdot)$:

$$\mathrm{F.map}^{\beta}_{\mathrm{conv}} = \mathcal{g}\left(W^{\beta} \otimes \mathcal{X}_i + B(\beta) \cdot J\right) \tag{6-7}$$

where J is a tensor with all elements equal to 1. $W^{\beta} \otimes X_i$ denotes the 2D-convolution of the filter kernel with the input. Its detailed expression depends on the padding (p) and strides (st), and can be found in many textbooks.[219] Take for example the convolution of a 2×2 kernel (w_{ij}) with a 3×3 input matrix (x_{ij}), stride $\mathrm{st} = 1$ and padding $\mathrm{p} = 0$, the output is a 2×2 matrix (y_{ij}). If we unroll the input and output into vectors from left to right and top to bottom, the computation of convolution can then be represented as the matrix operation below:

$$\mathcal{M}x = y \tag{6-8}$$

$$\mathcal{M} = \begin{pmatrix} w_{11} & w_{12} & 0 & w_{21} & w_{22} & 0 & 0 & 0 & 0 \\ 0 & w_{11} & w_{12} & 0 & w_{21} & w_{22} & 0 & 0 & 0 \\ 0 & 0 & 0 & w_{11} & w_{12} & 0 & w_{21} & w_{22} & 0 \\ 0 & 0 & 0 & 0 & w_{11} & w_{12} & 0 & w_{21} & w_{22} \end{pmatrix}$$

$$x = (x_{11} \;\; x_{12} \;\; x_{13} \;\; x_{21} \;\; x_{22} \;\; x_{23} \;\; x_{31} \;\; x_{32} \;\; x_{33})^T$$

$$y = (y_{11} \;\; y_{12} \;\; y_{21} \;\; y_{22} \;\;)^T$$

Using this formulation, the forward passes during the training step are computed by multiplying the input data with $\mathcal{M}$, and the error is back-propagated by multiplying the loss with $\mathcal{M}^T$.

6.3.2. Transposed convolution

Transposed convolution is widely used in computer vision problems as a decoding layer of a convolution auto-encoder to project the feature maps to a higher dimensional space.[238-240] For example, people used stride transposed convolution layer to decode the feature maps from convolutional encoding layers and up-sample the feature maps to acquire the image semantic segmentation.[241] Transposed convolution can be considered as a transformation in the opposite direction of the regular convolution. It works by swapping the forward and backward passes of a regular convolution. As seen in Eq. 6-8, the forward and backward passes for a regular convolution are computed by multiplying the input x by $\mathcal{M}$ and $\mathcal{M}^T$, respectively; the forward and backward passes for transposed convolutions are calculated by multiplying input x with $\mathcal{M}^T$ and $\mathcal{M}$, respectively. Transposed convolutions are also known as the *fractionally strided convolutions* because it is always possible to emulate a transposed convolution with a direct convolution by adding many columns and rows of zeros to the input.[242] It should be noted that

transposed convolution does not recover the input of the convolution itself, but rather returns the feature maps that have the same size as the input.

6.3.3. Deep convolutional encoder-decoder networks (U-Net)

The convolutional encoder-decoder (U-Net) architecture is an extension of CNN for problems with pixel-wise prediction. It has shown high efficiency in handling the mapping between high-dimensional input and output. For example, U-Net has been used successfully in biomedical image segmentation[238, 243] and conditional shape generation.[244] Inspired by these works, we adopt the U-Net architecture for solving the inverse model defined in Section 2, i.e., to predict the binary conductivity field of a 2D composite from its temperature field.

The architecture of our U-Net model is shown in Fig. 6-2. The measured temperature field, represented as a 2D image, is the input for the U-Net and the binary conductivity field, in which a pixel value of 1 (-1) corresponds a local conductivity $k = 200$ (4) $\mathrm{W/(m \cdot K)}$ is the output prediction. To reduce computation costs, the input temperature field images are downsampled to 64×64 pixels using kernel[217] before feeding to the U-Net model. Below we outline the different layers in the U-Net model.

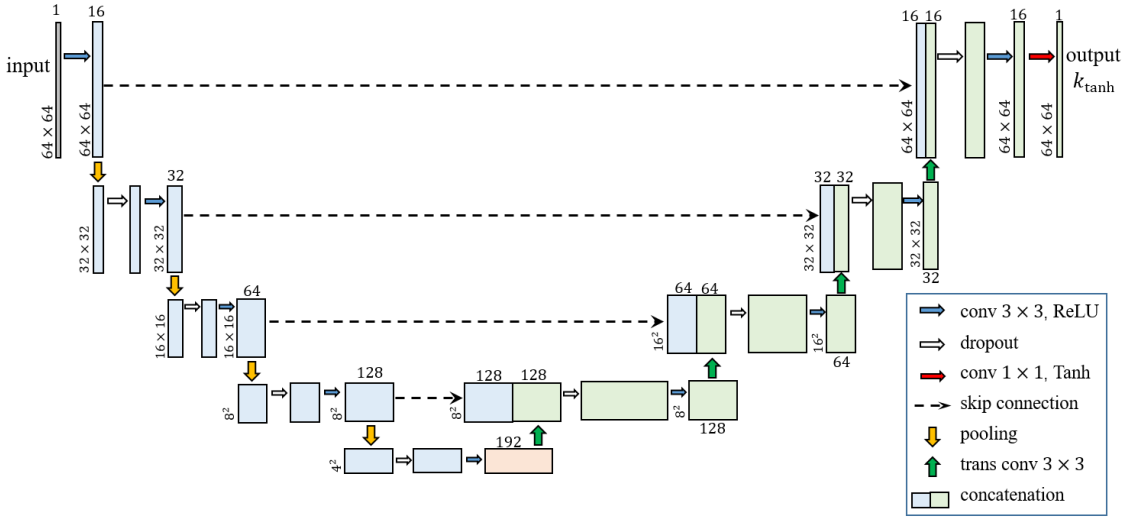

Figure 6-2. The U-Net architecture in this work. Blue boxes correspond to the feature map for the encoder, and the green boxes correspond to the feature maps for the decoder. The orange box denotes the bottleneck. The number of channels is marked on the top of each box; the x-y size (weight and height of the feature map) is provided at the lower-left edge of the box. The arrows denote the different operations explained in the legend.

As illustrated in Fig. 6-2, our U-Net model consists of an encoder with a contracting path (left side), a decoder with an expansive path (right side) and a bottleneck that connects the encoder and the decoder part. The encoder part follows the typical structure of CNN, with 4 repeating units and each unit contains three layers: (1) the input data of each layer is applied with a 3×3 convolutional layer (all convolution layers in this study have the same padding and unit stride) and followed by an ReLU activation function; (2) the output feature maps of the first layer are downsampled with a 2×2 max pooling layer with stride $st = 2$; (3) to avoid overfitting, a dropout layer with keep ratio $kp = 0.5$ is applied before feeding the data to the convolution layer at the next unit.

The decoder part consists 4 repeating units, and each unit contains 4 layers: (1) the input feature maps are up-sampled via transposed convolutions (all the transposed convolutions in this study are applied with the same padding and a stride of $st = 2$) and followed by the ReLU activation function; (2) the output features are then concatenated with its corresponding feature maps from the encoder part by the contracting paths, which are referred to as skip connections; (3) the dropout layer is applied to the concatenated features to avoid overfitting; (4) the output results from dropout layer are fed to a regular convolution layer and followed by the ReLU activation function.

We apply a convolutional layer at the bottleneck to connect the encoder and decoder part. At the last layer of the U-Net, a 1×1 convolution with tanh activation function is used to map features to the desired output $k_{\tanh}$. The final prediction for binary conductivity fields is obtained through thresholding

$$\hat{k}(\boldsymbol{x}) = \begin{cases} 200 & (\text{if } k_{\tanh} > 0) \\ 4 & (\text{if } k_{\tanh} < 0) \end{cases} \tag{6-9}$$

The U-Net model includes hyperparameters such as the size and volume of the feature map produced by each convolutional/pooling layer, the choice of the activation function after each convolution layer, the number of total layers, and training epochs, etc. In this work, these hyperparameters are selected based on the performance of the model on the validation dataset. The optimized hyperparameters are marked in Fig. 6-2 and presented in Section 3.

The above U-Net model is implemented using Tensorflow.[222] The L2 loss is adapted to quantify how well the model reproduces the training dataset:

$$L_2 = \frac{1}{2}\sum_{l=1}^{N}\sum_{i=1}^{N_x}\sum_{j=1}^{N_y}\left(k_{\mathrm{ij,tanh}} - k_{ij}^{l}\right)^2 \tag{6-10}$$

where N is the number of samples, N_x (N_y) is the number of pixels in the *x*- (*y*-) direction of the image of the 2D composite. $k_{\mathrm{ij,tanh}}$ and k_{ij}^{l} are the predictions by the model after the 1×1 convolution with tanh activation function and the ground truth for pixel *ij* of a sample *l*.

The U-Net model is trained using the training dataset. During training, all weights of the kernels are initialized using a truncated normal distribution with a standard deviation of 0.1, and all biases are set to 0.1. Adam Optimizer[223] with decay learning rate (initialized with 8×10^{-4} and decreased by 40% every 200 epochs) is applied to minimize L_2 in Eq. 6-10. The training stops at 3000 epochs when the validation error is minimized. We save the optimized weights and biases for all learnable filters every 1000 epoch during the training process. The saved parameters at the final step are then restored for evaluating the testing dataset.

6.4. Performance of Deep Learning Models

Here, we examine the performance of our deep learning model for predicting the heterogeneous structure of 2D composites (i.e., their binary thermal conductivity field) from their temperature fields. The prediction error for a sample *l* is defined as

$$E_l = \frac{1}{N_x \times N_y}\sum_{i=1}^{N_x}\sum_{j=1}^{N_y}\sqrt{\left(\hat{k}_{ij}^{l} - k_{ij}^{l}\right)^2} \tag{6-11}$$

where $\hat{k}_{ij}^{l}$ is the model's prediction of the binary conductivity field. The average accuracy for the testing dataset is defined as $\overline{Acc} = 1.0 - \frac{1}{N}\sum_{l=1}^{N} E_l$. The number of pixels at which the temperature is measured to serve as input, N_{mea}, is varied to test the model's performance. We first demonstrate that the deep learning model performs well if the temperature field measured at each pixel in the composite is used as input. We next show that the model performs quite well with the temperature at <1% of the pixels as input providing that suitable preprocessing of the temperature input is

performed. Finally, we demonstrate that the deep learning model can be used to guide the placement of the temperature sensors and the extra data measured by these sensors can be used to enhance the prediction accuracy of our model.

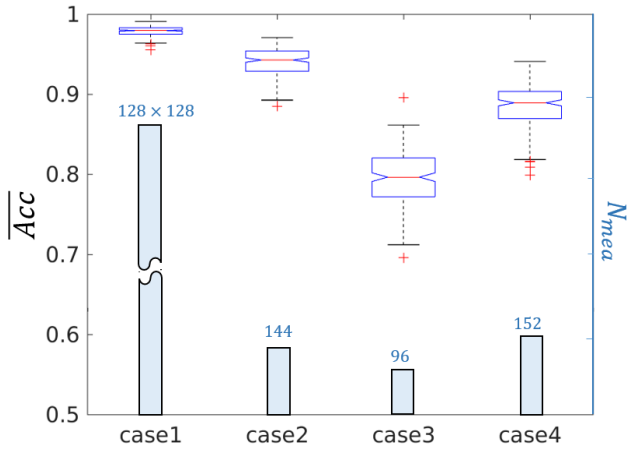

Figure 6-3. Boxplot of the prediction accuracy and the required number of temperature measurements for deep learning models in this work. case1: model trained with full temperature measurement (i.e., the temperature is available at each pixel). case2: model trained with temperature field obtained through the Laplace interpolation of the sparse temperature input. case3: model trained with temperature field obtained through the Laplace interpolation of the sparse temperature data on the composite's boundaries (<0.6% of the full measurement). case4: model trained with temperature field obtained through the Laplace interpolation of the sparse temperature data measured at positions suggested by the deep learning model.

6.4.1. Deep learning model with full-scale inputs

Figure 6-3 shows the performance of the deep learning model when its input is taken as the temperature field measured at all pixels in the composite (hereafter referred to as full temperature field) for the testing dataset. The average accuracy of the predicted binary conductivity field is $\overline{Acc} = 0.979$. Figure 6-4a shows the temperature field in a representative example. Figures 6-4b and 6-4c show the true and predicted binary thermal conductivity fields in the example shown in Fig. 6-4a, respectively. We observe that the conductivity field predicted by the U-Net model agrees well with the true field. The histogram of the prediction error for the testing dataset is presented in Fig. 6-4d and we observe that >70% of test data have prediction error less than 2%. Interestingly, from the input temperature field shown in Fig. 6-4a, we can loosely discern the contours of the high-conductivity fillers. Apparently, the spatial correlations within the temperature field discerned

by human is extracted well by the encoder model (in the form of feature maps, see Eq. 6-7); Otherwise, the binary conductivity field would not be predicted accurately by the decoder model, whose predictive power relies significantly on the effective extraction of features by the encoder model.

When the distribution of fillers becomes more complicated, e.g., when some fillers overlap with each other, it becomes increasingly harder to discern the contours of the fillers in the temperature field by eyes. Nevertheless, the U-Net model can still predict the binary conductivity fields well under those conditions (see Fig. SD1 in the Supplementary Material). This suggests that deep learning can perform better than humans under some conditions.

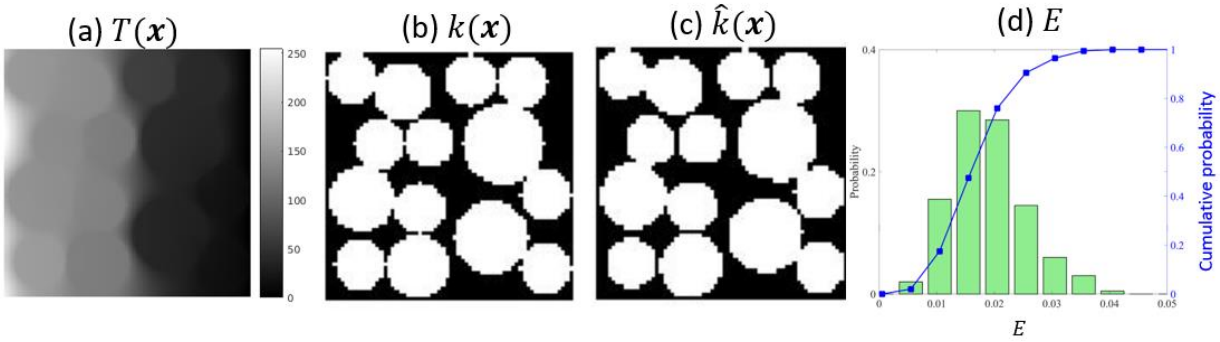

Figure 6-4. (**a-c**) The temperature field (a), true binary thermal conductivity field (b), and the predicted binary thermal conductivity field (c) in a representative composite. In (b-c), the black (white) color mark the positions with thermal conductivity of 4 (200) W/m·K. (**d**) The histogram of the prediction error of the U-Net model.

In the above example, the contrast between the thermal conductivity of the filler (200 W/(m·K)) and the matrix (4 W/(m·K)) is quite high. To clarify how the contrast between the conductivity of the filler and matrix affects the performance of our model, we performed four sets of studies by keeping the matrix conductivity at k_m=4 W/(m·K) but varying the filler conductivity as k_f =4.4, 8, 20, and 200 W/(m·K). Our studies thus cover a conductivity contrast of $\gamma = k_f / k_m$ = 1.1, 2, 5, and 50. The structure of the composite is identical to that used above. Figure 6-5 summarizes the model performance for these datasets. The model performs quite well for conductivity contrast $\gamma \geq 5$. For example, Fig. 6-5a shows the model's average accuracy $\overline{Acc}$, and we observe that $\overline{Acc}$ is better than 0.979 for $\gamma \geq 5$. Figure 6-5b shows the cumulative

probability of the prediction error E for all structures in each dataset. We observe that, at γ=5, the model has a prediction error E <0.02 for more than 70% of the structures in the dataset. Because a conductivity contrast of at least 5 is widely encountered (e.g., matrix materials such as plastics have a conductivity of ~0.1 W/(m·K) and most fillers have a conductivity of at least a few W/(m·K)), the performance of the model is adequate under practical conditions.

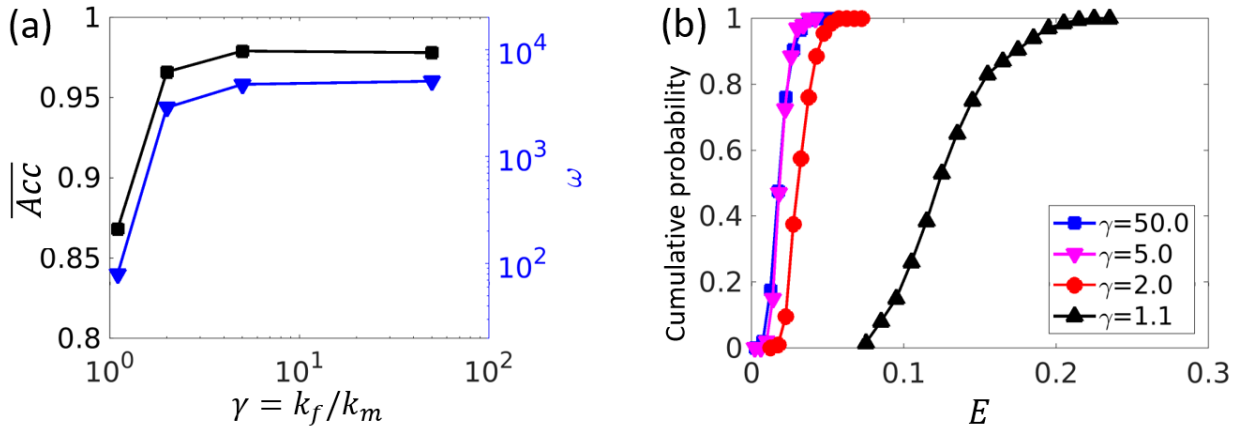

Figure 6-5. Performance of the deep learning model with dataset featuring different conductivity contrast between the filler and the matrix ($\gamma = k_f / k_m$ = 1.1, 2, 5, and 50). (**a**) The average prediction accuracy. (**b**) the cumulative probability of the distribution of prediction error E for all structures in the dataset. The histograms of the prediction error E for γ = 1.1 and 5.0 are shown in Fig. SD2 in the Supplementary Materials.

When γ decreases from 5 to 2, $\overline{Acc}$ decreases from 0.979 to 0.965. Such a reduction of $\overline{Acc}$ by 0.014, which corresponds to an increase of the error by 68%, is often considered a significant decline for deep learning models. When γ decreases further to 1.1, the model's predictive power decreases sharply: its $\overline{Acc}$ drops to 0.87; its prediction error is larger than 0.08 for virtually all structures in the dataset and is between 0.12 and 0.24 for more than 50% of the structures.

The decreased model performance as γ is lowered can be understood as follows. If the conductivity is homogeneous in a composite, its temperature field obeys the Laplace equation (i.e., $\nabla^2 T = 0$) everywhere. Essentially, the deep learning model is trained to approximate the correlations between the non-Laplacian distribution of the temperature field and the binary

conductivity fields in the composite. We postulate that if the non-Laplacian nature of the temperature field is strong, then the model should be able to learn to approximate these correlations and perform well; otherwise, the model will perform poorly. To test this postulation, we characterize the non-Laplacian nature of the temperature field by defining a parameter ω

$$\omega = \frac{1}{N_t}\sum_{i=1}^{N_t}\iint|\nabla^2 T|\,dA \tag{6-12}$$

where the integration is performed over each composite i and N_t is the number of composites in the dataset. As shown in Fig. 6-5a, ω decreases as γ is reduced, especially when γ reduced from 2 to 1.1. This trend corresponds very well to the evolution of the average accuracy with γ shown in the same figure, thus supporting our postulation. In the following sections, simulations are all performed under fixed conductivity contrast γ=50.0.

6.4.2. Deep learning model with coarse-grained inputs

The above deep learning model uses a high-resolution temperature field in the composite as input (128×128 pixels in the composite considered here). In practice, measuring high-resolution temperature fields can be time-consuming and costly, both when preparing the training dataset and when applying the trained model. Here, we test the performance of the U-Net model when coarse-grained temperature fields are used as input. Specifically, for each training dataset prepared in Section 2, which features the temperature at 128×128 pixels (see, e.g., Fig. 6-6a), the temperature at 12×12 pixels uniformly distributed in the 2D composite (see Fig. 6-6c) is extracted. The measurement effort is thus reduced to $12^2/128^2$ (i.e., <1%) of the original models. Each training, validation, and testing dataset now contains the coarse-grained temperature field and the original binary thermal conductivity field given at 128×128 pixels.

Since we seek to predict the binary thermal conductivity field with high resolution, we first up-sample the coarse-grained temperature field in all datasets to 128×128 pixels uniformly distributed in the composites. Next, a U-Net model with the same architecture, hyperparameters, and training protocol as those in Section 4.1 is adopted and trained. Finally, using the coarse-grained temperature field in the testing dataset as input, we evaluate the performance of the trained

model. Note that because the true temperature field is available only at 12×12 pixels both during the training and deployment of our U-Net model, the above scheme does allow us to evaluate the performance of deep learning models using coarse-grained input.

We use the Laplace interpolation for the upsampling of the input temperature field. The Laplace interpolation method has been widely used to recover damaged images.[245] For an arbitrary variable y defined in a 2D space, whose value y_i is known at points x_i (i=1 to N), its values at other points are obtained by solving the Laplace equation $\nabla^2 y = 0$ under the condition $y(\boldsymbol{x}_i) = y_i$. The Laplace interpolation method is selected for two reasons. On the one hand, because the temperature to be interpolated is governed by an equation similar to the Laplace equation (see Eq. 6-1), such an interpolation method may perform well in up-sampling the temperature field. On the other hand, the jump of thermal conductivity at base matrix-filler interfaces means that the Laplace interpolation necessarily introduces errors into the temperature field, and it is interesting to investigate whether these errors will compromise the predictions of the deep learning model. Figure 6-6d shows the temperature field up-sampled using the Laplace interpolation when the true temperature field (see Fig. 6-6a) is given at 12^2 pixels distributed uniformly in the composite (see Fig. 6-6c). The average relative error of the up-sampled temperature is 29%, indicating that considerable errors exist in this temperature field. Here the average relative error of the up-sampled temperature field for a sample l is defined as

$$\overline{AE}_l = \frac{1}{N_x \times N_y} \sum_{i=1}^{N_x} \sum_{j=1}^{N_y} \sqrt{\left(\tilde{T}_{ij}^l - T_{ij}^l\right)^2} / T_{ij}^l \tag{6-13}$$

where $\tilde{T}_{ij}^l$ and T_{ij}^l are the interpolated and true temperature at pixel ij, respectively. Besides, it is difficult to discern the contours of the fillers from the up-sampled temperature field.

Figure 6-6e shows the binary thermal conductivity field predicted by our U-Net model when the temperature field shown in Fig. 6-6d is used as the input. The predicted binary field closely resembles the true field shown in Fig. 6-6b. The average prediction accuracy of the binary thermal conductivity field based on the temperature fields up-sampled using the Laplace interpolation method is 0.94 (see Fig. 6-3) over the whole testing data, slightly lower compared with the case in which the temperature field is available at every pixel in the composite. Further inspection of the

prediction error (see Fig. 6-6f) reveals that over 95% of the tested cases have an average error of less than 10%. Given that the true temperature is available only at less than 1% of the pixels in the composite, the performance of the deep learning model is remarkable.

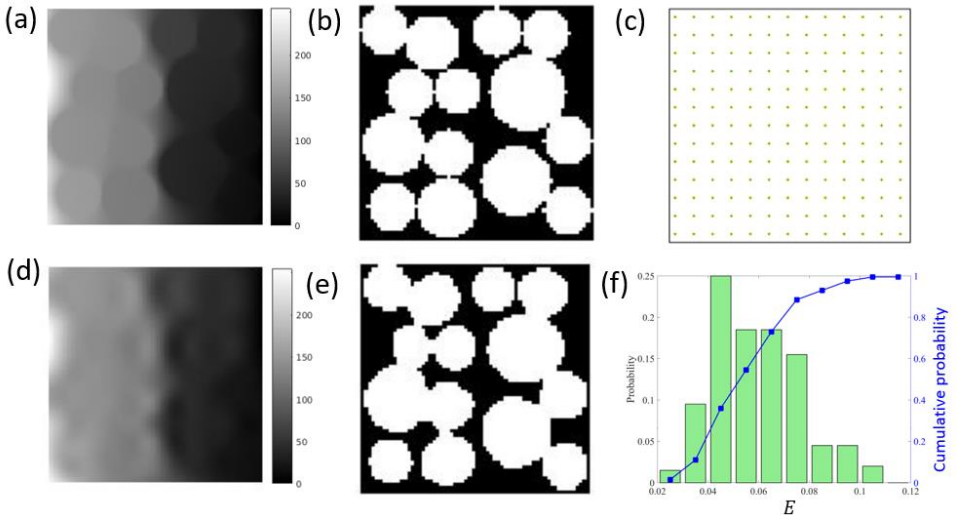

Figure 6-6. (**a-b**) The temperature field (a) and true binary thermal conductivity field (b) in a representative composite. (c) The distribution of the points at which the true temperature is available as input to the U-Net model. (**d-e**) The temperature field up-sampled using Laplace interpolation (d) and the binary thermal conductivity field (e) predicted using the up-sampled temperature field for the composite shown in (d). (**f**) The histogram of the prediction error of the U-Net model using temperature field up-sampled from coarse-grained temperature fields by Laplace interpolation.

The comparison of the predicted and true binary thermal conductivity field (see Fig. 6-6b and 6-6e) shows that the deep learning model can capture the curvature of fillers with a radius of ~10 pixels, despite the fact that the true temperature field is only known at coarsely distributed points with a spacing of 12 pixels. This success is likely related to the way the geometrical features are extracted and represented in deep learning models. In the deep learning model, the geometrical features of the fillers are implicitly encapsulated in the spatial correlations in the temperature fields. The several layers of filters in the encoder model can extract the spatial correlations in the temperature field at many length scales, which allows the geometrical features of the binary thermal conductivity field (and thus the curvature of the fillers) to be resolved at length scales comparable to the spacing between the points at which the true temperature is known. Therefore, the deep learning model has some potential advantages over methods based on finite difference

and finite element methods. In those methods, because the differential operator in Eq. 6-1 is discretized locally, the mesh size must be considerably smaller than the radius of curvature of the geometrical features in the computational domain to capture the temperature fields well. The ability of deep learning models to capture global (large scale) features without requiring fine-grained input should be explored more systematically in the future.

6.4.3. Deep learning model using boundary-only inputs

While the interpolation-based upsampling allows the binary thermal conductivity fields in a composite to be predicted from coarse-grained temperature data, the deep learning model requires data measured *inside* the composite. This kind of measurement is often more difficult to implement than measuring the temperature on boundaries, especially in three-dimensional composites. To study if this limitation can be alleviated, here we explore the situation when the temperature is only measured on the boundaries of the 2D composite. Specifically, the temperature is only measured at 96 points distributed evenly on the composite's four boundaries shown in Fig. 6-1.

With the true temperature measured on boundaries, we first obtain the temperature inside the composite using the Laplace interpolation. The interpolated temperature field for a representative case is shown in Fig. 6-7a and the corresponding true temperature field is shown Fig. 6-6a. The interpolated temperature fields deviate from the true temperature fields with an average relative error of $\overline{AE_l}$ = 43%. The interpolated field does not reproduce the true field well and contours of fillers are hardly discernible in the interpolated temperature field. Figure 6-7c shows the binary thermal conductivity field predicted by the U-Net model. We observe that the model can reveal in what regions the high-conductivity fillers are located. This suggests that the encoder model can capture large-scale spatial correlations in the imperfect temperature field, and the decoder model can use these correlations to reconstruct the location of the fillers to a large extent. Nevertheless, the deep learning model has difficulties delineating the filler-matrix interfaces, particularly in the space where several fillers come close to each other (highlighted using blue ovals in Fig. 6-7c) and in the composite's interior. This is consistent with the fact that the interpolated temperature field cannot capture the temperature variation at small scales and away from the boundaries. Over the

entire testing dataset, the average prediction accuracy of the binary conductivity field is $\overline{Acc} = 0.797$ (see Fig. 6-3), with over 95% of the cases having an average error of less than 25% (see Fig. 6-7d). Given that the true temperature is available only on the boundaries and at ~0.5% of all pixels in the composite, the accuracy of the deep learning model seems to be reasonable.

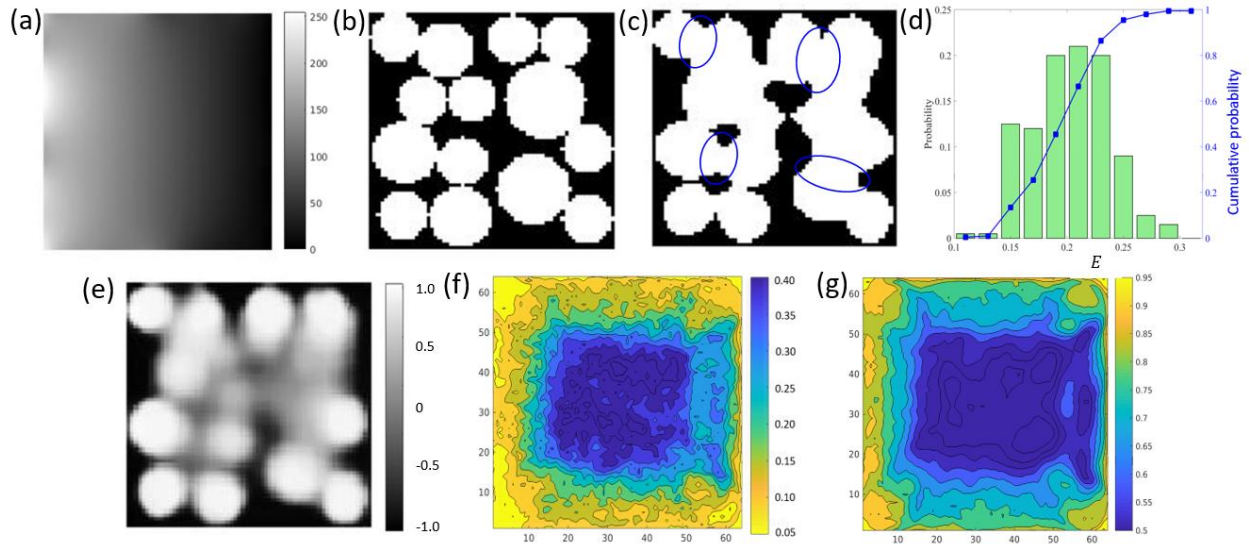

Figure 6-7. (**a**) The temperature field interpolated from the temperature given on 96 uniformly distributed points on the boundary of the composite (the true temperature field is shown in Fig. 6-6a). (b) The true binary thermal conductivity field corresponding to the true temperature field. (**c**) The binary thermal conductivity field predicted by the U-Net model using the interpolated temperature field shown in panel (a). (**d**) The histogram of the prediction error of the U-Net model over the entire testing dataset. (**e**) The prediction of the tanh layer of the deep learning model (see Fig. 6-2) when the true temperature and binary thermal conductivity fields are given by panels (a) and (b), respectively. (**f-g**) The distribution of the average error of the predicted binary thermal conductivity E_{ij} (f) and the average model confidence $\overline{\mathrm{CF}}_{ij}$ (g) in the composite over the entire testing data.

6.4.4. Improve deep learning prediction by model-informed temperature measurement

For the example composite in Fig. 6-7b, Fig. 6-7c shows that the model's prediction of the binary thermal conductivity field is relatively poor in the composite's interior. This poor performance can be inferred from the model itself. The last layer of our model is a tanh layer, which outputs a $k_{\tanh}$ at each pixel in the composite (see Fig. 6-7e for an example). Thresh-holding $k_{\tanh}$ using 0 as the decision threshold gives the predicted binary thermal conductivity field. Therefore, $k_{\tanh}$ can be used as a surrogate for the confidence of the predicted binary thermal

conductivity: a large (small) deviation of k_{tanh} from the decision threshold 0 corresponds to a prediction with high (low) confidence. In the grayscale representation of k_{tanh} in Fig. 6-7e, regions with color close to perfect black and white are places where the deep learning model is "certain" about the local thermal conductivity; while the regions with color more intermediate to black and white (mostly in the composite's interior) correspond to places where the deep learning model is "uncertain" about the local thermal conductivity. The latter regions, in which the deep learning model has less confidence (or more uncertainty), indeed correspond to the regions in which the predicted binary thermal conductivity has larger errors (cf. Fig. 6-7b and 7c).

The relatively poor performance of the deep learning model in the composite's interior when the true temperature is available on its boundary and the strong correlation between poor performance and the low model confidence revealed by the tanh layer's output are generally true for all composites studied here. Specifically, we compute the average prediction error for pixel *ij* inside all composites in the testing dataset by $\bar{E}_{ij} = \sum_{l=1}^{N} \left| \hat{k}_{ij}^{l} - k_{ij}^{l} \right| / N$. Figure 6-7f shows that $\bar{E}_{ij}$ in the composite's interior is indeed larger than that near its boundary. We also define model confidence for each pixel *ij* inside all composites in the testing dataset by $\overline{CF}_{ij} = \sum_{l=1}^{N} \left| k_{\text{tanh,ij}} \right| / N$, where $\overline{CF}_{ij} = 1$ and 0 correspond to a confidence level of 100% and 0%, respectively. Figure 6-7g shows that the regions with low model confidence roughly coincide with the regions with high prediction error (cf. Fig. 6-7f).

The strong correlation between the large prediction error and the low model confidence at a pixel can be used to guide the placement of temperature sensors for improving the model performance and reducing the number of temperature measurements. For example, because the model confidence in the composite's interior is low when the true temperature is only available at the boundary, we can introduce additional sensors in this region to potentially reduce the prediction error in this region. To explore this idea, in addition to the 96 boundary points used in Section 4.3, we introduce 56 measurement points into the composite's center region (see Fig. 6-8a). We then compute the temperature field in the composite using the Laplace interpolation method. Figure 6-

8b shows the interpolated temperature field, which deviates from the true temperature field (see Fig. 6-6a) with an average relative error $\overline{AE_l}$ = 30%. The binary thermal conductivity field predicted based on this temperature field is presented in Fig. 6-8c. When compared with the result in Fig. 6-7c, the prediction is markedly improved, especially in the composite's central part. For the whole testing dataset, we find that average prediction accuracy is $\overline{Acc} = 0.885$ (see Fig. 6-3), and over 90% of the predictions have an error of less than 15% (see Fig. 6-8d). Apart from this, the model confidence and the average prediction accuracy in the composite's central region are improved from ~55% to ~80% and from ~0.65 to ~0.85, respectively (see Fig. 6-8e and Fig. 6-8f). Therefore, measuring the temperature at additional points in the composite based on feedback from the deep learning model (i.e., the distribution of the model confidence across the composite) helps improve the model's performance. The accuracy of the model is slightly lower than the model in Case 2 shown in Fig. 6-3, where the true temperature is measured at 144 points inside the composite. However, the number of temperature measurements inside the composite is about half of that in case 2.

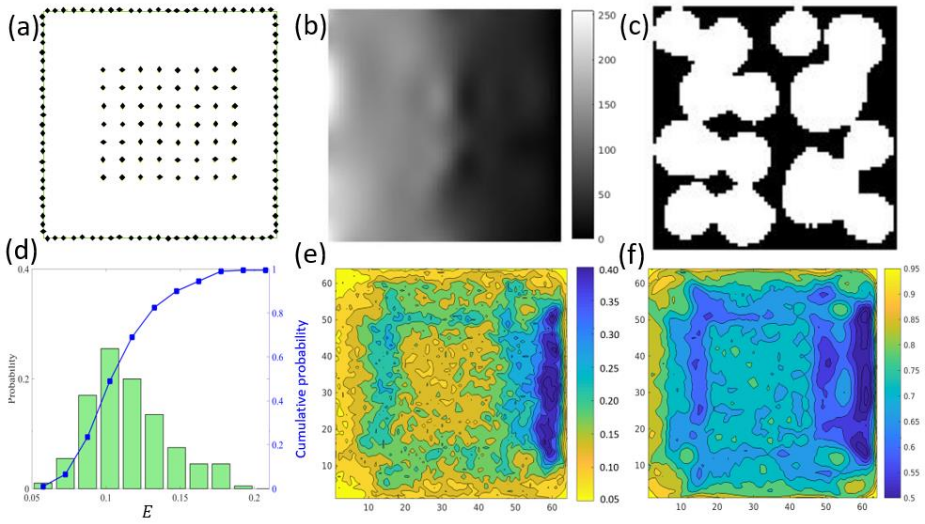

Figure 6-8. (**a**) The positions at which the true temperature is measured to provide input for the deep learning model. (**b**) The temperature field interpolated from the temperature at points marked in panel (a) (the true temperature field is shown in Fig. 6-6a). (**c**) The binary thermal conductivity field predicted by the U-Net model using the interpolated temperature field shown in panel (b). (**d-e**) The histogram of the average prediction error (d) and the distribution of the average model confidence $\overline{CF_{ij}}$ (e) for composites in the entire testing dataset (f).

6.5. Discussion

The results in Section 4 show that, for composites featuring circle-shaped fillers randomly distributed in a 2D matrix, deep learning models can predict a composite's structure from its temperature fields with reasonable accuracy. Therefore, although deep learning models for the quantitative solution of engineering problems are still in their infancy, they show considerable promise. The practical application of the deep learning models, however, must tackle several important problems no addressed here, e.g., they should be extended to three-dimensional (3D) systems with more realistic heterogeneity and sufficient training data must be generated to train these models. We are cautiously optimistic that these problems can be solved.

First, the deep learning model can likely be extended to 3D systems. Recently, exciting progresses have been reported in several papers on predicting the transport property of 3D porous media from their structure using CNN.[17, 206, 246] These works suggest that deep learning techniques are promising for solving 3D problems. Besides, U-Net models are good at mapping between high-dimensional data, and the feasibility of using it in 3D multi-class segmentation problems has been demonstrated[247]. Secondly, deep learning model should be able to handle more general heterogeneity, e.g., composites in which arbitrarily shaped fillers are dispersed in a base matrix. Indeed, we have tested a dataset in which circular fillers can overlap with each other, which produces partially irregular fillers (see Fig. SD1a). The model's average prediction accuracy for this dataset is $\overline{Acc} = 0.972$, which is similar to the situation where no overlap between fillers exists. The good prediction accuracy here suggests that deep learning models can potentially deal with heterogeneity in a relatively general sense. However, this must be checked more thoroughly (especially in 3D systems) in the future. Nevertheless, extensive tests must be performed to confirm the feasibility of the U-Net model in solving inverse problems involving realistic, 3D heterogeneous structures.

Finally, generating large dataset for training deep learning model should be feasible in many situations. Although building a large dataset experimentally can be challenging, this does not necessarily prevent the application of deep learning models. First, in many fields related to

transport phenomena (e.g., petroleum engineering), massive datasets are generated experimentally on a daily basis. Some of these datasets are available to the public, e.g., the digital rock database. Second, large datasets can be built computationally. Realistic composite structures can be generated not only experimentally not also computationally.[131] For many problems, a reliable mathematical model is available (heat conduction equation in our study). Because only forward problems (predicting temperature field from structure) must be solved when building a dataset, a massive dataset can be built by solving such problems using matured algorithms and high-performance clusters. Datasets thus built can be used to train the deep learning model. While care must be taken when using these datasets (e.g., ensuring the composite structure in the dataset is representative of the structure in real composites), they do greatly alleviate the difficulty associated with generating data by experiments.

6.6. Conclusions

In summary, we develop a deep learning-based model to predict the distribution of high-conductivity fillers in a low-conductivity 2D matrix from the temperature field within their composite. By adopting the encoder-decoder architecture, our U-net model handles the high dimensional input and output fields effectively. When the true temperature at every pixel in the composite is used as the input, the model accurately predicts the filler distribution in the composite. Even when coarse-grained temperature fields (<1% of the full data) are used as input, the model still performs reasonably well; the model's performance can be improved further if the temperature data in selected regions, in which the model has low prediction confidence, are introduced as an extra input.

While the present work deals with an inverse problem involving heat conduction, conceivably, similar models can be developed for other transport phenomena involving similar governing equations (e.g., fluid transport in heterogeneous media with non-uniform permeability). More generally, this work demonstrates the feasibility of solving inverse problems with high-dimensional input and output using deep learning models. Importantly, the geometrical features of fillers in the composite can be predicted with a spatial resolution slightly higher than the spatial

resolution of the true temperature field. This suggests that the encoder sub-model can effectively capture the large-scale features of the temperature field despite the uncertainty (noise) at fine scales, and the decoder sub-model can map these features to the binary thermal conductivity field effectively. Since only coarse-grained input fields are available for solving many practical inverse problems, the results shown here are encouraging for the future development of deep learning models for these problems.

Supporting Information

All supporting information cited in this chapter is located in Appendix D.

Chapter 7. Conclusions

In this dissertation, two important aspects of the multiphysics transport inside heterogeneous media are explored. In the first part, new physics of gas/liquid transport in porous media arising from nanoscale confinements are studied using physics-based simulations, with applications in shale gas recovery and drying of nanoporous filtration cakes. In the second part, the effective transport properties of porous media and the structure of heterogeneous thermal composites are solved using deep learning models.

In Chapter 2, the recovery of single-component shale gas from single nanopores is studied using molecular simulations. The van der Waals gas - pore wall interactions are modeled explicitly, and these interactions are found to lead to significant gas adsorption on pore walls and reduce the gas diffusivity below that predicted by kinetic theories. The simulations reveal that gas recovery follows a super-diffusive scaling law, similar to some field observations. By building a continuum gas recovery model in which gas adsorption and desorption are parameterized by the molecular dynamics results and by systematically studying the gas recovery scaling law using this model, it was ascertained that the super-diffusive gas recovery observed in molecular simulations originates from strong gas-wall interactions.

In Chapter 3, molecular dynamics simulations are used to understand the storage of methane-ethane mixtures in single nanopores and extraction of the gas mixtures from the nanopores. Surface adsorption is found to contribute over 60% of the total storage capacity of 2nm-wide pores for both gas species at reservoir pressures from 20 to 200 bar. Ethane is enriched inside the nanopores in equilibrium with bulk methane-ethane mixtures due to their stronger interactions with pore walls. Such enrichment becomes more significant as the pore size is reduced, but is weakened when the gas pressure increases. The trend of the computed multicomponent gas adsorption is captured by the ideal adsorbed solution (IAS) theory. Simulation of the recovery of the gas mixture shows the production rates of both gases roughly follows the diffusive scaling at the early stage of gas recovery. The simulation results for the recovery rate ratio between ethane and method is found to

be close to their initial mole ratio inside the pore. The Onsager coefficients, which are calculated from separate simulations for the transport of binary ethane-methane mixture inside the nanopores, are used into scale analysis to understand the observed gas recovery rate ratio.

Apart from the physical insights into the gas storage (recovery) in (from) nanopores, the work in Chapter 2 and 3 establishes molecular simulations as a valuable tool for studying the far-from equilibrium gas recovery process at pore scale. Because the length and time scales accessible by molecular dynamics simulations are orders of magnitude smaller than those in gas recovery from shale formations, essentially all previous molecular dynamics studies of shale gas were limited to the calculation of gas storage and gas transport properties inside nanopores, which are not limited by the length and time scale explorable by molecular simulations. Whether molecular simulations can provide useful insights into the real gas recovery process is far from clear. This is especially true because some undesired features intrinsic to such simulations, e.g., extremely large pressure gradient along pore length and large pressure jump from pore opening to the gas bath during gas recovery, may incur modeling artifacts. In this regard, the fact that molecular simulations capture the scaling law of gas recovery rate reported in field studies and continuum simulations suggests that those undesired features do not incur notable artifacts. The methods and protocols developed in this dissertation, combined with the intrinsic advantages of molecular dynamics simulations in resolving the thermodynamic and transport properties of shale gas (and more generally any fluids), will be powerful tools for studying other far-from-equilibrium processes in hydrocarbon extraction from unconventional sources, e.g., CO_2-based enhanced gas and oil recovery from shales.

In Chapter 4, a pore network model is established for predicting the drying of porous media with nanoscale pores. The drying process is driven by a purge gas flowing through the nanoporous media, which is initially saturated with a volatile liquid solvent. The model includes several unique features: the drainage and evaporation processes can occur concurrently; the multicomponent gas transport is included to describe the mass transfer through pore throats. Three stages are identified during the drying process. In the first stage, drying is dominated by drainage, where liquid solvents

are gradually displaced by purge gas. In the second stage, the drainage and evaporation effects are comparable with each other. In the last stage, evaporation effects dominate drying, although some drainage still exists due to the coupling between evaporation and drainage. The coupling between drainage and evaporation effects significantly affects the evolutions of the liquid clusters during the last stage of drying, including the size and distributions of clusters in the porous medium, hence affecting the drying kinetics.

In Chapter 5, convolutional neural network (CNN) models are developed and trained to predict the effective diffusivity of 2D porous media using their structure image as input. Simulation results demonstrate that the CNN model could predict the effective diffusivity of diverse porous media with complex topologies (i.e., dead-end pathways and trapped pore space) with reasonable accuracy at a computational cost more than six orders of magnitude lower than classical pore-scale simulations. The prediction accuracy generally decreases as the true effective diffusivity of the porous media decreases. To improve model accuracy, the porosity of porous media is incorporated directly into the CNN model, although the improvement is marginal. Improvement for porous media with an effective diffusivity $D_e \lesssim 0.1$ can be achieved via preprocessing the image of the porous media (e.g., removing the trapped space and dead-end transport pathways) or via training the CNN model using a truncated relative error as the loss functions.

In Chapter 6, the convolutional encoder and decoder model (U-net) is adopted to identify the distribution of high-thermal conductivity fillers in 2D thermal composites using the temperature field in the composites as an input. The U-net model is found to approximate the mapping between high-dimensional temperature field and conductivity field effectively. The model can accurately infer the distributions of fillers with an average prediction accuracy over 0.979 when full-scale true temperature fields are used as input. The model performs well when the contrast between the thermal conductivity of the filler and the matrix materials is reduced to about 5. The model can still perform reasonably well with an average prediction accuracy over 0.94 when coarse-grained temperature fields with <1% of the full-scale data are adopted as input. The predictive performance of the U-net model can be improved by incorporating more true temperature measurements in the

regions where the model has low prediction confidence.

The work in Chapter 5 and Chapter 6 demonstrates the feasibility of applying deep learning models to efficiently and accurately solve forward and inverse transport phenomena problems in heterogenous media. Therefore, although deep learning models are still in their infancy in terms of solving transport phenomena problems, they have considerable promise in addressing some long-standing challenges in the numerical solution of these problems. Nevertheless, more practical applications of deep learning models require several important issues to be tackled. For instance, extending the current models to 3D systems, generating sufficient training data efficiently, and reducing the size of dataset required in the training step. These issues most likely can be addressed. This cautious optimism is based on the recent progress in machine learning. For example, deep learning models have been extended to 3D problems (e.g., U-net models have been demonstrated in 3D multi-class medical image segmentation),[247] massive datasets can be built using high-fidelity numerical simulations, new deep learning models are being developed to reduce the required data size in the training step,[248] and governing equations of physical problems can be incorporated into deep learning models to constrain their convergence and reduce the size of the required training dataset.[152, 249]

Appendix

Appendix A

A1. Isotherms for gas storage inside slit nanopores

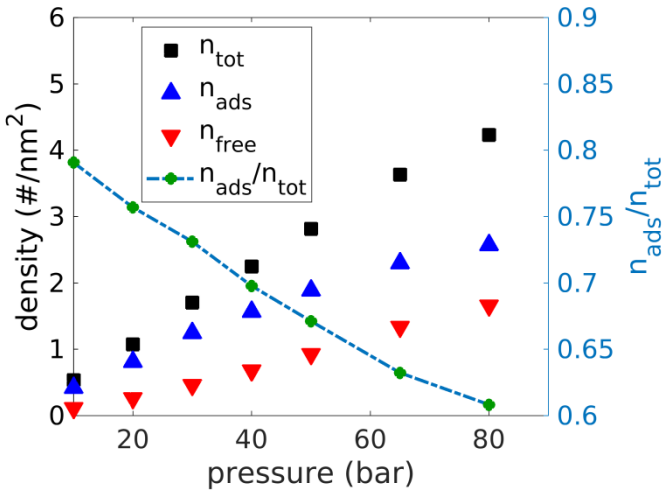

Figure SA1. Isotherm of the storage of ethane in 2nm-wide nanopores in equilibrium with a pure ethane bath and the contribution by the adsorbed and free gas to the total gas storage.

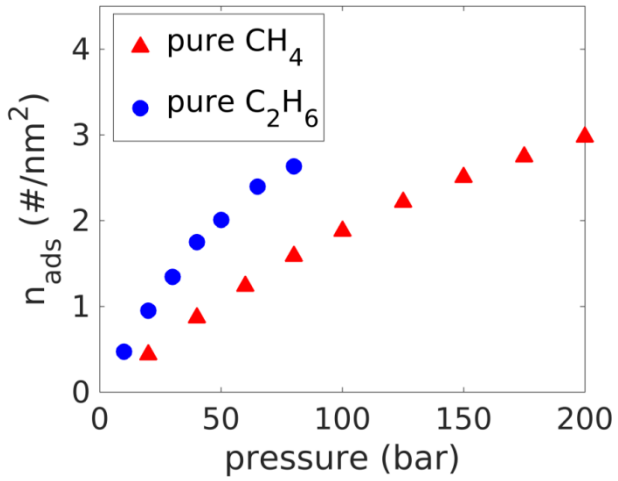

Figure SA2. Isotherms of methane and ethane adsorbed on the walls of a 4nm-wide nanopore when the pore is in equilibrium with pure methane and pure ethane gas bath, respectively.

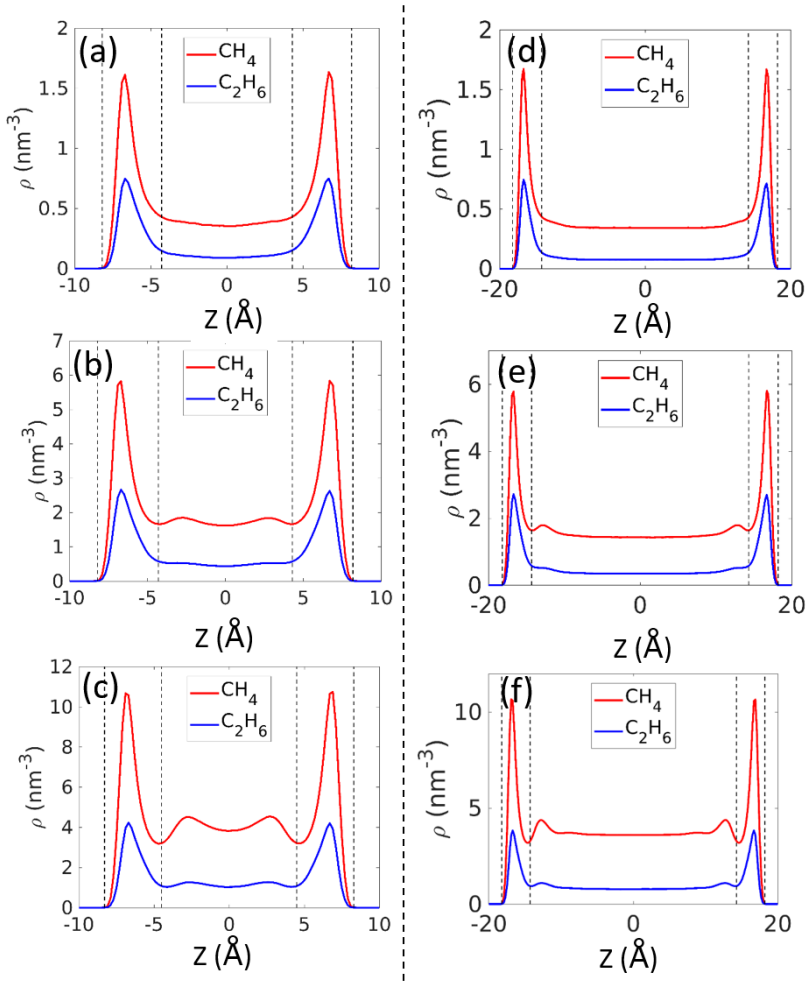

Figure SA3. Density profiles of ethane and methane molecules across 2.0nm-wide (a-c) and 4.0nm-wide (d-f) pores. The pores are in equilibrium with baths of methane-ethane mixture, in which the ethane mole fraction is 0.2 and the pressure is 20 (a,d), 80 (b,e), and 200bar (c,f). The dashed lines delineate the adsorption layers we defined in the main text, which have a thickness of 4 Å.

A2. Transport properties of methane and ethane inside slit nanopores

To gain insight into the mobility of methane and ethane confined inside slit nanopores, we computed their total diffusion coefficient using non-equilibrium molecular dynamics (NEMD) simulations.

Simulation system. Each system consists of a nanopore that is periodical along its length direction (*x*-direction) and pure methane (or ethane) molecules inside it. The pore width and the structure of pore walls are identical to those in the main text. The number of gas molecules inside the nanopores are varied to produce different pressure.

Calculation of total diffusion coefficient using force-driven simulations. A constant force of $F_x = 0.143$ pN is applied to each gas molecule in the *x*-direction, and the average velocity of the gas molecules is measured. Since the total diffusion coefficient is defined using $j_x = -D_t(\rho)\partial\rho/\partial \mathrm{x}$, it cannot be computed directly from our force-driven simulations. Instead, it is determined using the Darken equation[1]

$$D_t = \frac{k_B T}{F_x}\langle \mathrm{v}_x \rangle \cdot \left(\frac{\partial \ln f}{\partial \ln \rho}\right)_T = \frac{m}{F_x}\langle \mathrm{v}_x \rangle \cdot \frac{\rho}{\rho_b}\left(\frac{\partial P}{\partial \rho}\right)_T \tag{A1}$$

where m is the molecular mass of each gas molecule. $\langle \mathrm{v}_x \rangle$ is the mean velocity of each gas molecule under a driving force of F_x, ρ_b is the density in gas bath, and f is the fugacity. $\left(\frac{\partial P}{\partial \rho}\right)_T$ is computed from the relation between the density and pressure of the gas inside the pore. ρ/ρ_b is determined from the relation between gas density in gas bath and pores.

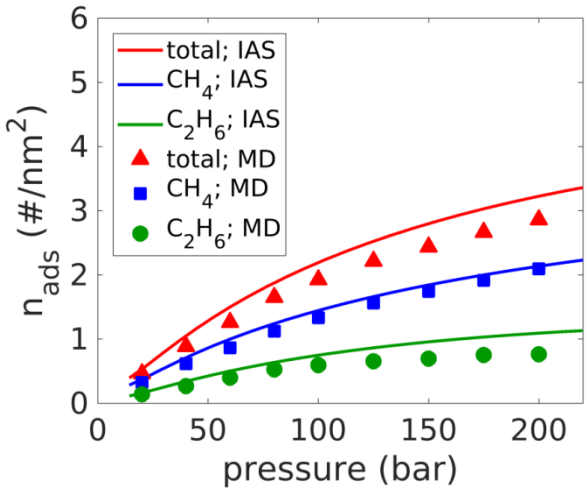

Figure SA4. Isotherm of methane and ethane adsorption on walls of a 4.0nm-wide pore predicted by MD simulations and the IAS theory. The nanopore is in equilibrium with a bath of methane-ethane mixture, in which the mole fraction of ethane is 0.2±0.01.

A3. Prediction of Q_e/Q_m when concentration polarization at pore mouth is considered

In the scale analysis described in the main text, the concentration polarization near the pore mouth is neglected when estimating the flux ratio of ethane and methane (i.e., $P_{1,m}$ is set to the pressure in gas bath (P_{bath}) and $P_{2,m}$ is set to zero when evaluating G_{21} in Equ. 3-13b). To

account for the concentration polarization, we first use the ethane and methane gas densities at pore mouth measured in MD simulations at a representative time instant $t/t_c = 0.01$ (see Fig. 3-6c) to compute the partial pressure of each gas at pore mouth by assuming that each as follows the idea gas law. Using obtained values ($P_{1,m} = 40$ bar and $P_{2,m} = 15$ bar), Equ. 3-11, and the transport properties shown in Table 2 in the main text, a $Q_e/Q_m = 0.213$ is obtained. This Q_e/Q_m is only ~1% smaller than the one obtained when the concentration polarization effect is neglected.

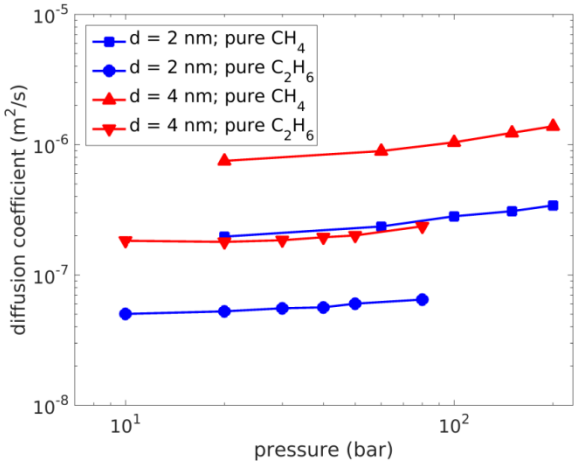

Figure SA5. Average total diffusion coefficients of pure methane and pure ethane confined inside 2nm- and 4nm-wide nanopores computed using NEMD simulations.

Appendix B

In Chapter 4, the coupling of drainage and evaporation effects is conceptualized as three looped steps occurring in a space initially occupied by a liquid cluster: evaporation-induced pore throat emptying, drainage through the emptied throats and alteration of liquid saturation distribution, and alteration of the evaporation in that space. Here we perform simulations to illustrate these steps in a pore network where a well-defined liquid cluster exists. The statistics of the pore bodies and throats of this pore network are the same as those in the main text except that the radius of the pore throats connecting the pore bodies in a 10×20 region (termed trapped region hereafter and is delimited using a red box in Fig. B1) to the pore bodies outside of this region are selected so that their threshold pressure is larger than 1.4 bar. Simulation is then performed with an applied pressure difference of 1.4 bar across the entire pore network. The solvent liquids in the trapped region would be permanently confined in this region without evaporation effects.

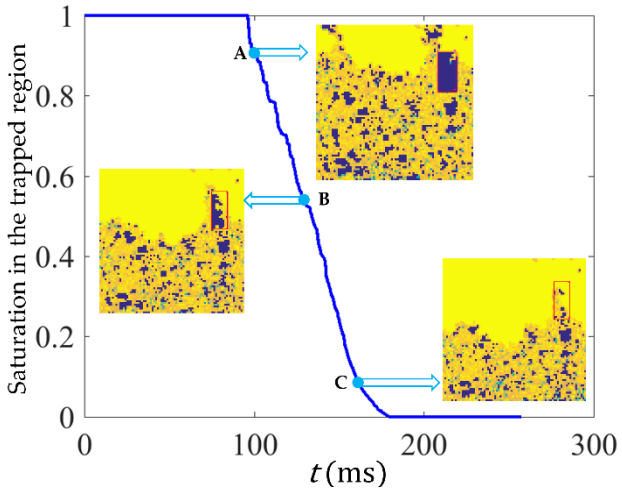

Figure B1. The evolution of the liquid saturation distribution inside the "trapped" region (marked using a red box), where a liquid cluster would be permanently trapped in absence of the evaporation effects.

The evolution of the liquid saturation distribution inside the trapped region is shown in Fig. B1. Due to evaporation-induced emptying of pore throats surrounding the trapped region, purge gas breaks into the liquid cluster in this region at $t \sim 95.0$ ms and displaces the liquid solvent downstream (see the snapshot at point A in Fig. B1). The gas flow then fingers through the liquid cluster in the trapped region, which in turn generates new gas pathways (see the snapshot at point

B). During this process, liquids are drained out of the trapped region. Meanwhile, the liquid drainage and gas flow fingering change the distribution of the remaining liquids in and around the trapped region (see the snapshot at point C), which greatly affects the evaporation of liquids in the partially-saturated pore bodies in the trapped region. Because of the coupled drainage and evaporation effects, the liquids in the trapped region are dried out eventually.

Table B1. Statistics of the drainage-only simulations

	$\Delta P_{ud} =$ 1.4 bar	$\Delta P_{ud} =$ 1.5 bar	$\Delta P_{ud} =$ 2.0 bar
Breakthrough time	8.9 ms	9.0 ms	5.6ms
Mean liquid saturation at the time of breakthrough	0.78	0.76	0.8
Time after which liquid saturation no longer changes	160.0 ms	158.3 ms	106.5 ms
Residual liquid saturation at long time	0.25	0.24	0.22

Appendix C

C1. Basic concept of neural network and convolutional neural network

A classical neural network consists of N layers with the k^{th} layer containing n_k neurons (see Fig. SC1-a for an example), A neuron i in a layer k processes the output of layer $k-1$ neurons ($x_j^{k-1},\ j = 1 \cdots n_{k-1}$) by first assigning weights and biases to this output and then passing the result to a nonlinear activation function f to generate its output

$$x_i^k = f(\sum_{j=1}^{n_{k-1}} W_{i,j}^k x_j^{k-1} + B_i^k) \tag{SC1}$$

where $W_{i,j}^k$ and B_i^k are the weight and bias of neuron i for the output of the neuron j in the layer $k-1$. Equation (S1) can be written compactly as

$$\mathrm{X}^k = f(W^k \mathrm{X}^{k-1} + B^k) \tag{SC2}$$

where $\mathrm{X}^{\mathrm{k-1}}$ is a $n_{k-1} \times 1$ vector, W^k is a $n_k \times n_{k-1}$ matrix, and B^k is a $n_k \times 1$ vector. A neuron network is defined once the number of neuron layers (N), the number of neurons in each layer (n_k), the weight and bias of all neurons (W^k and B^k, $k = 1, 2, \cdots, N$), and the activation function (f) are determined. Of these parameters, N, $n_{1,2,\cdots,N}$, and f are termed *hyperparameters* and are specified when developing a neural network. W^k and B^k are termed *learnable parameters* to be determined during the training of the neural network. Neural networks can be used for tasks such as classifying images. Because each neuron in an arbitrary layer k is fully connected with all neurons in layer $k-1$ and $k+1$ and the learnable parameters W^k and B^k are by default different for each neuron layer, the number of learnable parameters is enormous when the input of a neural network features massive data (e.g., when an input image has a large number of pixels and multiple color channels). Hence, classical neural networks can involve prohibitive computational cost and is prone for overfitting.

The convolutional neural network (CNN) is a variant of the classical neural network. As shown in Fig. SC1-b, a CNN typically consists of three types of layers: the convolutional layer, the pooling layer, and the fully-connected layer. Each type of layers can be included in any number

and sequence. The fully-connected layers in CNN are identical to those in the classical neural network and we only outline the first two types of layers.

A convolutional layer contains a 3D volume of neurons arranged in the width, height, and depth directions (see Fig. SC1-b). Both the neurons of layer k and their output are often termed volume k. Even though the neurons in a convolutional layer process information in a similar way as depicted in Equation (SC2), they differ from those in the classical neural networks in that (1) each neuron in a volume k only processes the output from a small number of neurons in volume $k-1$ and (2) within each depth slice of a volume k, all neurons have the same weights and biases. Due to these differences, the number of learnable parameters in CNN is greatly reduced compared to that in classical neural networks.[209, 250]

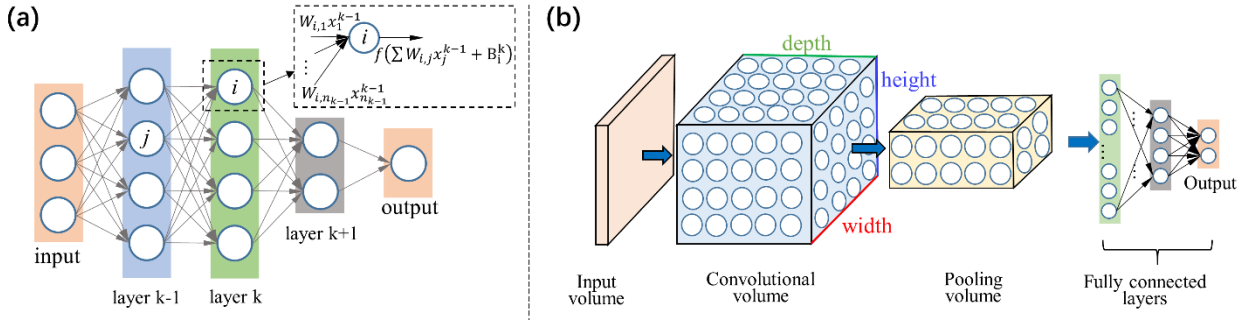

Figure SC1. The schematics of a simple classical neural network (a) and a simple convolutional neural network (b).

To further reduce the number of learnable parameters and overfitting, pooling layers are usually inserted periodically between convolutional layers. A pooling layer essentially downsamples the output of the convolutional layer preceding it and progressively reduces the neuron volume.[251] A typical pooling layer operates independently on each slice of the output volume of its preceding convolutional layer volume using algorithms such as the max pooling, average pooling, or L_2 norm pooling.[252]

C2. Computational framework for predicting diffusivity of porous media

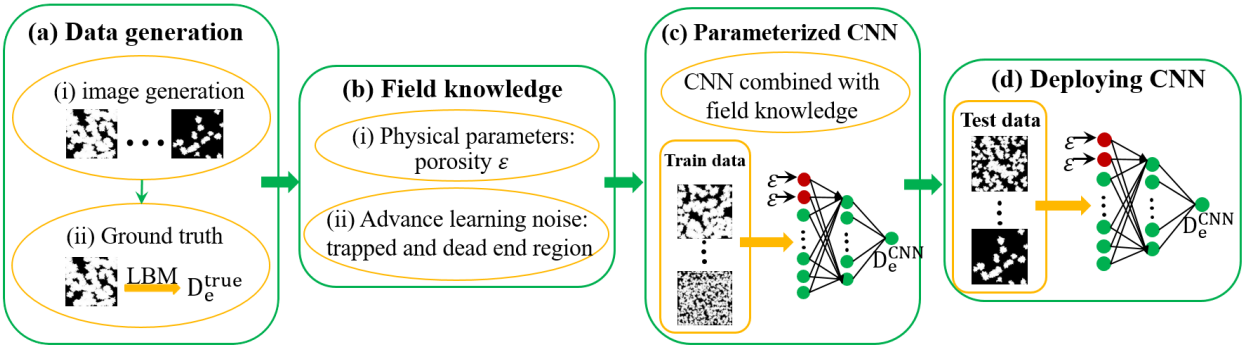

Figure SC2. Overview of the computational framework of using CNN to predict the effective diffusivity of porous media from their images.

C3. ResNet model for predicting the diffusivity of porous media

In addition to CNN model described in Fig. 5-2 of the main text, we also tested the deep residual network, which often gives better accuracy than the CNN in the main text. Deep residual networks are stacked with many residual learning blocks, which contain several convolutional layers and a short cut connection between the input and the output before the activation layer. Deep residual networks are substantially deeper than the regular CNN model, are easier to optimize, and can gain considerable accuracy from the increased layers. Training very deep residual networks, however, involves much higher computation cost than the CNN described in the main text.

Here, we implemented the Resnet50 model[136] to predict the effective diffusivity of porous media using the datasets in our original manuscript, both with and without removing the trapped regions in the preprocessing step. The architecture of the Resnet50 model is same as that in Ref. [136]. The training model is converged through minimizing the loss function Eq. 5-7 by the Adam Optimizer[223] (learning rate $\gamma = 10^{-4}$). The learning rate is reduced by 50% every 300 epochs to ensure stable convergence and the training model stops at 1600 epochs. The average mean-square-error (MSE), mean truncated relative error (MTRE) and the Pearson R^2 scores are summarized in the Table below.

The results of the Resnet50 model are summarized in Table SC1 and Fig. SC3. We observe that, compared to the model in the main text, the Resnet50 model perform slightly better: the MSE is reduced by ~20% for dataset with and without the preprocessing step. The improvement of the MTRE is smaller: ~8% and ~3% for dataset without and with preprocessing, respectively. Although the prediction accuracy for Resnet50 is slightly higher than the CNN model in the main text, the Resnet50 requires more computational resources to train. For example, compared to the CNN model in the main text, the Resnet50 model involves 10 times more parameters and requires 5 times longer training time.

Table SC1. comparison between the results by CNN models and resnet50 model

	Trained using the loss function Equ. 5-7 with original data			Trained using the loss function Equ. 5-7 with preprocessed image as input		
	MSE	MTRE	R^2	MSE	MTRE	R^2
CNN model	8.64×10^{-4}	68.8%	0.9903	6.92×10^{-4}	29.7%	0.9912
Resnet50	7.26×10^{-4}	60.50%	0.9918	5.34×10^{-4}	26.56%	0.9932

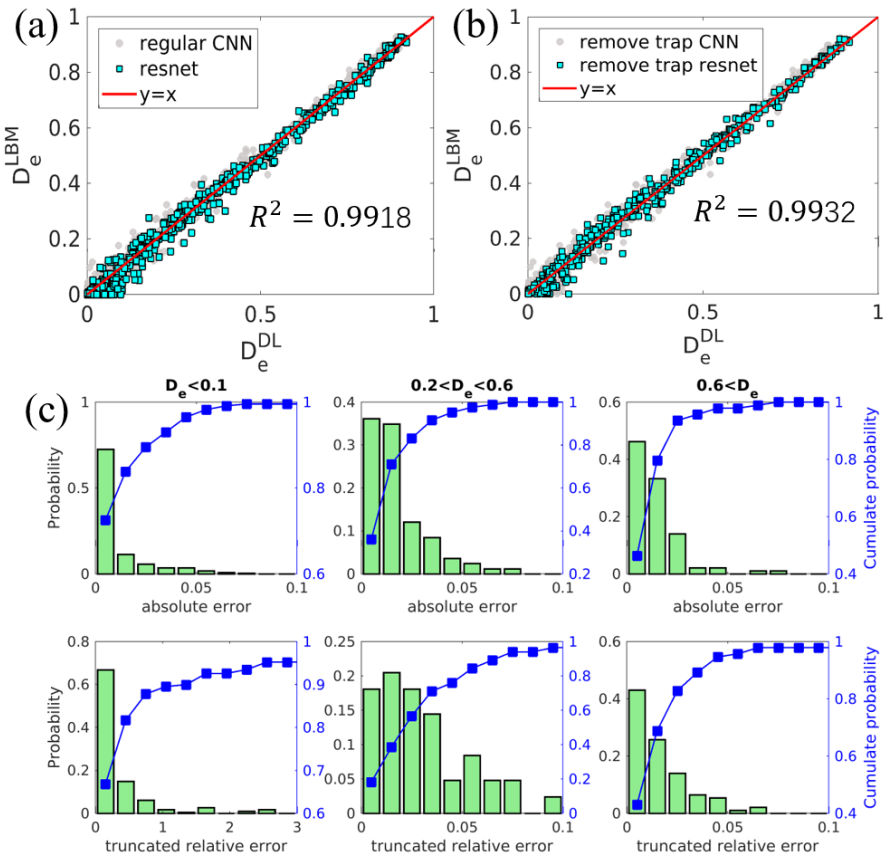

Figure SC3. (**a**) The effective diffusivity predicted by the Resnet50 model trained using a loss function based on the mean square error (Equation 5-7) with the dataset without preprocessing. (**b**) The effective diffusivity predicted by the Resnet50 model trained using a loss function based on the mean square error (Equation 5-7) with the dataset preprocessed by removing the trapped regions. (**c**) Distribution of the absolute error (top panels) and truncated relative error (lower panels) of the predictions of the Resnet50 model (trained with dataset that removed the trapped regions) for the porous structures in the testing dataset with different D_e.

Appendix D

SD1. Deep learning model for more complex heterogeneous media

The performance of the deep learning based inverse model which is trained with the full true temperature fields as input, and evaluated by using the testing dataset. The heterogeneous media in this case is more complex, the circle shapes can overlap with each other. As we can see in Fig. SD1(a), when circles are overlap with each other, it is more difficult to distinguish the circle shapes from temperature profiles. The exact binary conductivity fields and the prediction by the deep learning model are compared in Fig. SD1(b) and S1(c). As we can observe that the deep learning model can provide well prediction even complex structures are involved. The average evaluation accuracy of the binary conductivity fields for whole testing dataset is found to be $\overline{Acc} = 97.2\%$. The histogram of the prediction error for testing dataset are presented in Fig. SD1(d), over 60% of test data have prediction error less than 2.5%.

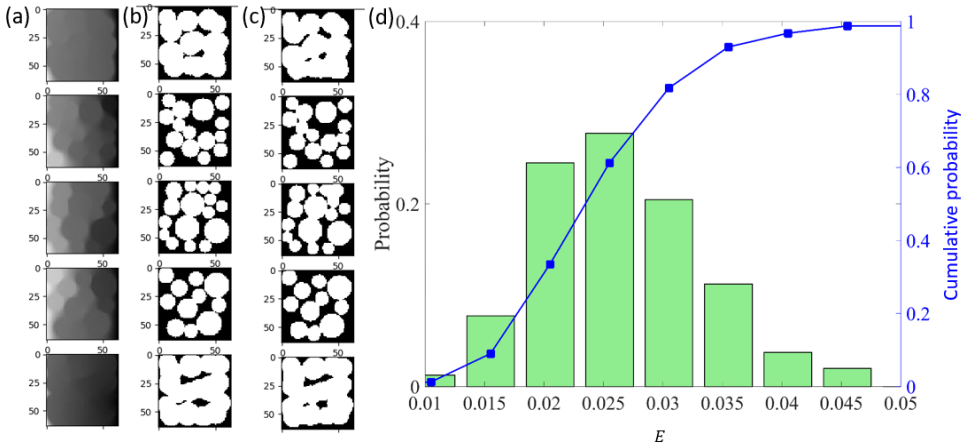

Figure SD1. (**a**) input temperature fields for U-Net model. (**b**) ground truth binary conductivity fields. (**c**) binary conductivity fields predicted by U-Net model with full input measurements. (**d**) histogram of the prediction error for U-Net model.

SD2. Histograms of the prediction error *E* for thermal contrast γ= k_f / k_m = 1.1 and 5.0

Figure SD2 shows the histograms of the prediction error E for datasets with thermal contrast γ= k_f / k_m = 1.1 and 5.0. We observe that $\overline{Acc}$ is better than 0.97 for $\gamma = 5$, and the model has a prediction error E <0.02 for more than 70% of the structures in the dataset. When γ decreases to 1.1, the model's predictive power decreases sharply: its $\overline{Acc}$ decreases to 0.87; its prediction error

is larger than 0.08 for virtually all structures in the dataset, and is between 0.12 and 0.24 for more than 50% of the structures.

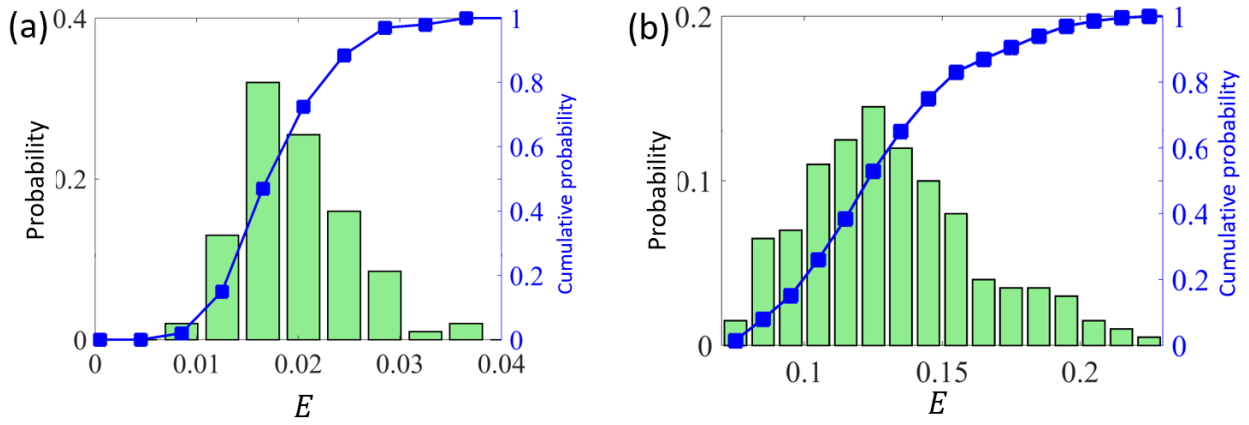

Figure SD2. Histogram of the prediction error E for the U-Net model with full input measurements as input. The thermal conductivity contrast γ is 5.0 (**a**) and 1.1 (**b**).

References

1. Peishi, C.; Pei, D. C., A Mathematical Model of Drying Processes. *Int. J. Heat Mass Tran.* **1989**, *32*, 297-310.
2. Le Gallo, Y.; Le Romancer, J.; Bourbiaux, B.; Fernandes, G. In *Mass Transfer in Fractured Reservoirs During Gas Injection: Experimental and Numerical Modeling*, SPE Annual Technical Conference and Exhibition, Society of Petroleum Engineers: 1997.
3. Loucks, R. G.; Reed, R. M.; Ruppel, S. C.; Jarvie, D. M., Morphology, Genesis, and Distribution of Nanometer-Scale Pores in Siliceous Mudstones of the Mississippian Barnett Shale. *J. Sediment. Res.* **2009**, *79*, 848-861.
4. Amann-Hildenbrand, A.; Ghanizadeh, A.; Krooss, B. M., Transport Properties of Unconventional Gas Systems. *Mar. Petrol. Geol.* **2012**, *31*, 90-99.
5. Bocquet, L.; Charlaix, E., Nanofluidics, from Bulk to Interfaces. *Chem. Soc. Rev.* **2010**, *39*, 1073-1095.
6. Liu, H.-H.; Lai, B.; Chen, J., Unconventional Spontaneous Imbibition into Shale Matrix: Theory and a Methodology to Determine Relevant Parameters. *Transport. Porous. Med.* **2016**, *111*, 41-57.
7. Wu, H.; He, Y.; Qiao, R., Superdiffusive Gas Recovery from Nanopores. *Phys. Rev. F* **2016**, *1*, 074101.
8. Wu, H.; He, Y.; Qiao, R., Recovery of Multicomponent Shale Gas from Single Nanopores. *Energy & Fuels* **2017**, *31*, 7932-7940.
9. Waananen, K.; Litchfield, J.; Okos, M., Classification of Drying Models for Porous Solids. *Drying technology* **1993**, *11*, 1-40.
10. Plourde, F.; Prat, M., Pore Network Simulations of Drying of Capillary Porous Media. Influence of Thermal Gradients. *International Journal of Heat and Mass Transfer* **2003**, *46*, 1293-1307.
11. Defraeye, T., Advanced Computational Modelling for Drying Processes–a Review. *Applied Energy* **2014**, *131*, 323-344.
12. Mujumdar, A. S., *Handbook of Industrial Drying*; CRC press, 2014.
13. Bruin, S.; Luyben, K. C. A. In *Drying of Food Materials: A Review of Recent Developments*, 1st. Int. Symp. Drying, Montreal, 1978, 1978.
14. Clerici, A.; Alimonti, G. In *Oil Shale, Shale Oil, Shale Gas and Non-Conventional Hydrocarbons*, EPJ Web of Conferences, EDP Sciences: 2015; p 03001.
15. Chabanon, M.; Valdés-Parada, F. J.; Ochoa-Tapia, J. A.; Goyeau, B., Large-Scale Model of Flow in Heterogeneous and Hierarchical Porous Media. *Advances in Water Resources* **2017**, *109*, 41-57.
16. Chen, L.; Fang, W.; Kang, Q.; Hyman, J. D. H.; Viswanathan, H. S.; Tao, W.-Q., Generalized Lattice Boltzmann Model for Flow through Tight Porous Media with Klinkenberg's Effect. *Physical Review E* **2015**, *91*, 033004.
17. Chen, L.; Kang, Q.; Dai, Z.; Viswanathan, H. S.; Tao, W., Permeability Prediction of Shale Matrix Reconstructed Using the Elementary Building Block Model. *Fuel* **2015**, *160*, 346-356.
18. Chen, L.; Zhang, L.; Kang, Q.; Viswanathan, H. S.; Yao, J.; Tao, W., Nanoscale Simulation of Shale Transport Properties Using the Lattice Boltzmann Method: Permeability and Diffusivity. *Sci. Rep.* **2015**, *5*, 8089.
19. Vignes, A., Diffusion in Binary Solutions. Variation of Diffusion Coefficient with Composition. *Industrial & Engineering Chemistry Fundamentals* **1966**, *5*, 189-199.

20. Mason, E. A.; Malinauskas, A., *Gas Transport in Porous Media: The Dusty-Gas Model*; Elsevier Science Ltd, 1983; Vol. 17.
21. Krishna, R.; Wesselingh, J., The Maxwell-Stefan Approach to Mass Transfer. *Chemical Engineering Science* **1997**, *52*, 861-911.
22. Jepps, O. G.; Bhatia, S. K.; Searles, D. J., Modeling Molecular Transport in Slit Pores. *J. Chem. Phys.* **2004**, *120*, 5396-5406.
23. Firouzi, M.; Rupp, E. C.; Liu, C. W.; Wilcox, J., Molecular Simulation and Experimental Characterization of the Nanoporous Structures of Coal and Gas Shale. *Int. J. Coal. Geol.* **2014**, *121*, 123-128.
24. Freeman, C.; Moridis, G.; Blasingame, T., A Numerical Study of Microscale Flow Behavior in Tight Gas and Shale Gas Reservoir Systems. *Transport. Porous. Med.* **2011**, *90*, 253-268.
25. Dudley, B., Bp Statistical Review of World Energy. *BP Statistical Review, London, UK, accessed Aug* **2018**, *6*, 2018.
26. EIA, U., Annual Energy Outlook 2013. U.S. Department of Energy, Ed. Washington, DC, 2013; pp 60-62.
27. Soeder, D. J., The Successful Development of Gas and Oil Resources from Shales in North America. *Journal of Petroleum Science and Engineering* **2018**, *163*, 399-420.
28. Zhang, Q.; Wang, W.-D.; Kade, Y.; Wang, B.-T.; Xiong, L., Analysis of Gas Transport Behavior in Organic and Inorganic Nanopores Based on a Unified Apparent Gas Permeability Model. *Petroleum Science* **2020**, *17*, 168-181.
29. Zou, C., *Unconventional Petroleum Geology*; Elsevier, 2017.
30. Al-Saleh, M.; Duffuaa, S.; Al-Marhoun, M.; Al-Zayer, J., Impact of Crude Oil Production on the Petrochemical Industry in Saudi Arabia. *Energy* **1991**, *16*, 1089-1099.
31. Willis, S. G.; Neal, C., M4shalegas-Measuring, Monitoring, Mitigating and Managing the Environmental Impact of Shale Gas.
32. Gu, X.; Cole, D. R.; Rother, G.; Mildner, D. F.; Brantley, S. L., Pores in Marcellus Shale: A Neutron Scattering and Fib-Sem Study. *Energy & Fuels* **2015**, *29*, 1295-1308.
33. Darabi, H.; Ettehad, A.; Javadpour, F.; Sepehrnoori, K., Gas Flow in Ultra-Tight Shale Strata. *J. Fluid Mech.* **2012**, *710*, 641-658.
34. Fisher, K., Data Confirm Safety of Well Fracturing. *The American Oil & Gas Reporter* **2010**, 1-4.
35. Curtis, M. E.; Ambrose, R. J.; Sondergeld, C. H. In *Structural Characterization of Gas Shales on the Micro-and Nano-Scales*, Canadian unconventional resources and international petroleum conference, Society of Petroleum Engineers: 2010.
36. Etminan, S. R.; Javadpour, F.; Maini, B. B.; Chen, Z., Measurement of Gas Storage Processes in Shale and of the Molecular Diffusion Coefficient in Kerogen. *Int. J. Coal. Geol.* **2014**, *123*, 10-19.
37. Wang, L.; Cao, H., Probable Mechanism of Organic Pores Evolution in Shale: Case Study in Dalong Formation, Lower Yangtze Area, China. *Journal of Natural Gas Geoscience* **2016**, *1*, 295-298.
38. Bohacs, K. M.; Grabowski Jr, G. J.; Carroll, A. R.; Mankiewicz, P. J.; Miskell-Gerhardt, K. J.; Schwalbach, J. R.; Wegner, M. B.; Simo, J. T., Production, Destruction, and Dilution—the Many Paths to Source-Rock Development. **2005**.
39. Zhang, Z.; Yang, S., On the Adsorption and Desorption Trend of Shale Gas. *Journal of experimental*

mechanics **2012**, *27*, 492-497.
40. Javadpour, F., Nanopores and Apparent Permeability of Gas Flow in Mudrocks (Shales and Siltstone). *J. Can. Petrol. Technol.* **2009**, *48*, 16-21.
41. Wang, H.; Qu, Z.; Yin, Y.; Bai, J.; Yu, B., Review of Molecular Simulation Method for Gas Adsorption/Desorption and Diffusion in Shale Matrix. *Journal of Thermal Science* **2019**, *28*, 1-16.
42. Liu, Y.; Wang, C., Determination of the Absolute Adsorption Isotherms of Ch4 on Shale with Low-Field Nuclear Magnetic Resonance. *Energy & fuels* **2018**, *32*, 1406-1415.
43. Ye, Z.; Chen, D.; Pan, Z.; Zhang, G.; Xia, Y.; Ding, X., An Improved Langmuir Model for Evaluating Methane Adsorption Capacity in Shale under Various Pressures and Temperatures. *J. Nat. Gas Sci. Eng.* **2016**, *31*, 658-680.
44. Bae, J.-S.; Bhatia, S. K., High-Pressure Adsorption of Methane and Carbon Dioxide on Coal. *Energy & Fuels* **2006**, *20*, 2599-2607.
45. Brunauer, S.; Emmett, P. H.; Teller, E., Adsorption of Gases in Multimolecular Layers. *Journal of the American chemical society* **1938**, *60*, 309-319.
46. Langmuir, I., The Adsorption of Gases on Plane Surfaces of Glass, Mica and Platinum. *Journal of the American Chemical society* **1918**, *40*, 1361-1403.
47. Li, D.; Zhang, L.; Wang, J. Y.; Lu, D., Composition-Transient Analysis in Shale-Gas Reservoirs with Consideration of Multicomponent Adsorption. *SPE J.* **2016**, *21*, 648-664.
48. Zhang, L.; Li, D.; Li, L.; Lu, D., Development of a New Compositional Model with Multi-Component Sorption Isotherm and Slip Flow in Tight Gas Reservoirs. *J. Nat. Gas Sci. Eng.* **2014**, *21*, 1061-1072.
49. Fathi, E.; Akkutlu, I. Y., Multi-Component Gas Transport and Adsorption Effects During Co 2 Injection and Enhanced Shale Gas Recovery. *Int. J. Coal. Geol.* **2014**, *123*, 52-61.
50. Chareonsuppanimit, P.; Mohammad, S. A.; Robinson, R. L.; Gasem, K. A., High-Pressure Adsorption of Gases on Shales: Measurements and Modeling. *Int. J. Coal. Geol.* **2012**, *95*, 34-46.
51. Weniger, P.; Kalkreuth, W.; Busch, A.; Krooss, B. M., High-Pressure Methane and Carbon Dioxide Sorption on Coal and Shale Samples from the Paraná Basin, Brazil. *Int. J. Coal. Geol.* **2010**, *84*, 190-205.
52. Tan, Z.; Gubbins, K. E., Selective Adsorption of Simple Mixtures in Slit Pores: A Model of Methane-Ethane Mixtures in Carbon. *J. Phys. Chem.* **1992**, *96*, 845-854.
53. Qajar, A.; Daigle, H.; Prodanovic, M., Methane Dual-Site Adsorption in Organic-Rich Shale-Gas and Coalbed Systems. *Int. J. Coal. Geol.* **2015**, *149*, 1-8.
54. Siperstein, F. R.; Myers, A. L., Mixed-Gas Adsorption. *Aiche. J.* **2001**, *47*, 1141-1159.
55. Clarkson, C.; Bustin, R., Binary Gas Adsorption/Desorption Isotherms: Effect of Moisture and Coal Composition Upon Carbon Dioxide Selectivity over Methane. *Int. J. Coal. Geol.* **2000**, *42*, 241-271.
56. Wang, Y.; Tsotsis, T. T.; Jessen, K., Competitive Sorption of Methane/Ethane Mixtures on Shale: Measurements and Modeling. *Ind. Eng. Chem. Res.* **2015**, *54*, 12187-12195.
57. Sharma, A.; Namsani, S.; Singh, J. K., Molecular Simulation of Shale Gas Adsorption and Diffusion in Inorganic Nanopores. *Mol. Simulat.* **2015**, *41*, 414-422.
58. Collell, J.; Galliero, G.; Gouth, F.; Montel, F.; Pujol, M.; Ungerer, P.; Yiannourakou, M., Molecular Simulation and Modelisation of Methane/Ethane Mixtures Adsorption onto a Microporous Molecular Model of Kerogen under Typical Reservoir Conditions. *Micropor. Mesopor. Mat.* **2014**, *197*, 194-203.

59. Myers, A.; Prausnitz, J. M., Thermodynamics of Mixed-Gas Adsorption. *Aiche. J.* **1965**, *11*, 121-127.
60. Wang, Z.; Guo, Y.; Wang, M., Permeability of High-Kn Real Gas Flow in Shale and Production Prediction by Pore-Scale Modeling. *J. Nat. Gas Sci. Eng.* **2016**, *28*, 328-337.
61. Vo, T. Q.; Kim, B., Transport Phenomena of Water in Molecular Fluidic Channels. *Sci. Rep.* **2016**, *6*, 33881.
62. Zhang, P.; Hu, L.; Meegoda, J. N.; Gao, S., Micro/Nano-Pore Network Analysis of Gas Flow in Shale Matrix. *Sci. Rep.* **2015**, *5*, 1-11.
63. Ziarani, A. S.; Aguilera, R., Knudsen's Permeability Correction for Tight Porous Media. *Transport. Porous. Med.* **2012**, *91*, 239-260.
64. Kang, S. M.; Fathi, E.; Ambrose, R. J.; Akkutlu, I. Y.; Sigal, R. F., Carbon Dioxide Storage Capacity of Organic-Rich Shales. *SPE J.* **2011**, *16*, 842-855.
65. Kapoor, A.; Yang, R.; Wong, C., Surface Diffusion. *Catalysis Reviews—Science and Engineering* **1989**, *31*, 129-214.
66. Oura, K.; Lifshits, V.; Saranin, A.; Zotov, A.; Katayama, M., *Surface Science: An Introduction*; Springer Science & Business Media, 2013.
67. Clifford, S. M.; Hillel, D., Knudsen Diffusion: The Effect of Small Pore Size and Low Gas Pressure on Gaseous Transport in Soil. *Soil science* **1986**, *141*, 289-297.
68. Sladek, K. J.; Gilliland, E. R.; Baddour, R. F., Diffusion on Surfaces. Ii. Correlation of Diffusivities of Physically and Chemically Adsorbed Species. *Industrial & Engineering Chemistry Fundamentals* **1974**, *13*, 100-105.
69. Antczak, G.; Ehrlich, G., Jump Processes in Surface Diffusion. *Surface science reports* **2007**, *62*, 39-61.
70. Wu, K.; Li, X.; Wang, C.; Yu, W.; Chen, Z., Model for Surface Diffusion of Adsorbed Gas in Nanopores of Shale Gas Reservoirs. *Ind. Eng. Chem. Res.* **2015**, *54*, 3225-3236.
71. Wang, G.; Ren, T.; Wang, K.; Zhou, A., Improved Apparent Permeability Models of Gas Flow in Coal with Klinkenberg Effect. *Fuel* **2014**, *128*, 53-61.
72. Swami, V.; Settari, A. In *A Pore Scale Gas Flow Model for Shale Gas Reservoir*, SPE Americas Unconventional Resources Conference, Pittsburgh, Pennsylvania USA, 5-7 June; Society of Petroleum Engineers: Pittsburgh, Pennsylvania USA, 2012; pp SPE-155756.
73. Fathi, E.; Tinni, A.; Akkutlu, I. Y., Correction to Klinkenberg Slip Theory for Gas Flow in Nano-Capillaries. *Int. J. Coal. Geol.* **2012**, *103*, 51-59.
74. Florence, F. A.; Rushing, J.; Newsham, K. E.; Blasingame, T. A. In *Improved Permeability Prediction Relations for Low Permeability Sands*, Rocky mountain oil & gas technology symposium, Society of Petroleum Engineers: 2007.
75. Sampath, K.; Keighin, C. W., Factors Affecting Gas Slippage in Tight Sandstones of Cretaceous Age in the Uinta Basin. *Journal of Petroleum Technology* **1982**, *34*, 2,715-2,720.
76. Jones, F. O.; Owens, W., A Laboratory Study of Low-Permeability Gas Sands. *Journal of petroleum Technology* **1980**, *32*, 1,631-1,640.
77. Heid, J.; McMahon, J.; Nielsen, R.; Yuster, S. In *Study of the Permeability of Rocks to Homogeneous Fluids*, Drilling and production practice, American Petroleum Institute: 1950.
78. Akkutlu, I. Y.; Efendiev, Y.; Vasilyeva, M., Multiscale Model Reduction for Shale Gas Transport in

Fractured Media. *Computational Geosciences* **2016**, *20*, 953-973.
79. Akkutlu, I. Y.; Efendiev, Y.; Vasilyeva, M.; Wang, Y., Multiscale Model Reduction for Shale Gas Transport in a Coupled Discrete Fracture and Dual-Continuum Porous Media. *J. Nat. Gas Sci. Eng.* **2017**, *48*, 65-76.
80. Akkutlu, I. Y.; Fathi, E., Multiscale Gas Transport in Shales with Local Kerogen Heterogeneities. *SPE J.* **2012**, *17*, 1,002-1,011.
81. Barisik, M.; Beskok, A., Scale Effects in Gas Nano Flows. *Phys. Fluids.* **2014**, *26*, 052003.
82. Pratikno, H.; Reese, D.; Maguire, M. In *Production Analysis in the Barnett Shale-Field Example for Reservoir Characterization Using Public Data*, SPE Annual Technical Conference and Exhibition, New Orleans, Louisiana, USA, 30 September-2 October; Society of Petroleum Engineers: New Orleans, Louisiana, USA, 2013.
83. Patzek, T. W.; Male, F.; Marder, M., Gas Production in the Barnett Shale Obeys a Simple Scaling Theory. *Proc. Natl. Acad. Sci.* **2013**, *110*, 19731-19736.
84. Civan, F.; Rai, C. S.; Sondergeld, C. H., Shale-Gas Permeability and Diffusivity Inferred by Improved Formulation of Relevant Retention and Transport Mechanisms. *Transport. Porous. Med.* **2011**, *86*, 925-944.
85. King, G. E. In *Thirty Years of Gas Shale Fracturing: What Have We Learned?*, SPE Annual Technical Conference and Exhibition, Florence, Italy, 19-22 September; Society of Petroleum Engineers: Florence, Italy, 2010.
86. Montgomery, S. L.; Jarvie, D. M.; Bowker, K. A.; Pollastro, R. M., Mississippian Barnett Shale, Fort Worth Basin, North-Central Texas: Gas-Shale Play with Multi–Trillion Cubic Foot Potential. *Am. Assoc. Pet. Geol. Bull.* **2005**, *89*, 155-175.
87. Lunati, I.; Lee, S., A Dual-Tube Model for Gas Dynamics in Fractured Nanoporous Shale Formations. *J. Fluid Mech.* **2014**, *757*, 943-971.
88. Chen, K. P.; Shen, D., Mechanism of Fluid Production from the Nanopores of Shale. *Mechanics Research Communications* **2018**, *88*, 34-39.
89. Lee, T.; Bocquet, L.; Coasne, B., Activated Desorption at Heterogeneous Interfaces and Long-Time Kinetics of Hydrocarbon Recovery from Nanoporous Media. *Nature communications* **2016**, *7*, 1-10.
90. Baihly, J. D.; Altman, R. M.; Malpani, R.; Luo, F. In *Shale Gas Production Decline Trend Comparison over Time and Basins*, SPE annual technical conference and exhibition, Florence, Italy, 19-22 September; Society of Petroleum Engineers: Florence, Italy, 2010.
91. Shabro, V.; Torres-Verdin, C.; Javadpour, F. In *Numerical Simulation of Shale-Gas Production: From Pore-Scale Modeling of Slip-Flow, Knudsen Diffusion, and Langmuir Desorption to Reservoir Modeling of Compressible Fluid*, North American Unconventional Gas Conference and Exhibition, Woodlands,Texas, USA,, 14-16 June; Society of Petroleum Engineers: Woodlands,Texas, USA,, 2011.
92. Panagiotou, N.; Stubos, A.; Bamopoulos, G.; Maroulis, Z., Drying Kinetics of a Multicomponent Mixture of Organic Solvents. *Drying technology* **1999**, *17*, 2107-2122.
93. Luikov, A. V., Heat and Mass Transfer in Capillary-Porous Bodies. In *Advances in Heat Transfer*, Elsevier: 1964; Vol. 1, pp 123-184.
94. Yiotis, A. G.; Stubos, A.; Boudouvis, A.; Yortsos, Y. C., A 2-D Pore-Network Model of the Drying of Single-Component Liquids in Porous Media. *Advances in Water Resources* **2001**, *24*, 439-460.

95. Hirt, C. W.; Nichols, B. D., Volume of Fluid (Vof) Method for the Dynamics of Free Boundaries. *J. Comput. Phys.* **1981**, *39*, 201-225.
96. Prodanović, M.; Bryant, S. L., A Level Set Method for Determining Critical Curvatures for Drainage and Imbibition. *Journal of colloid and interface science* **2006**, *304*, 442-458.
97. El Abrach, H.; Dhahri, H.; Mhimid, A., Numerical Simulation of Drying of a Deformable Anisotropic Porous Medium Using the Lattice Boltzmann Method. *Drying technology* **2013**, *31*, 1400-1414.
98. El Abrach, H.; Dhahri, H.; Mhimid, A., Lattice Boltzmann Method for Modelling Heat and Mass Transfers During Drying of Deformable Porous Medium. *Journal of porous media* **2013**, *16*.
99. Shokouhmand, H.; Hosseini, S.; Abdollahi, V., Numerical Simulation of Drying a Porous Material Using the Lattice Boltzmann Method. *Journal of Porous Media* **2012**, *15*.
100. Prat, M., Pore Network Models of Drying, Contact Angle, and Film Flows. *Chemical Engineering & Technology* **2011**, *34*, 1029-1038.
101. Yiotis, A. G.; Stubos, A. K.; Boudouvis, A. G.; Tsimpanogiannis, I. N.; Yortsos, Y. C., Pore-Network Modeling of Isothermal Drying in Porous Media. *Transport in Porous Media* **2005**, *58*, 63-86.
102. Freitas, D.; Prat, M., Pore Network Simulation of Evaporation of a Binary Liquid from a Capillary Porous Medium. *Transport. Porous. Med.* **2000**, *40*, 1-25.
103. Dong, H.; Blunt, M. J., Pore-Network Extraction from Micro-Computerized-Tomography Images. *Physical review E* **2009**, *80*, 036307.
104. Dong, H.; Fjeldstad, S.; Alberts, L.; Roth, S.; Bakke, S.; Øren, P.-E. In *Pore Network Modelling on Carbonate: A Comparative Study of Different Micro-Ct Network Extraction Methods*, International symposium of the society of core analysts, Society of Core Analysts, 2008.
105. Silin, D.; Patzek, T., Pore Space Morphology Analysis Using Maximal Inscribed Spheres. *Physica A: Statistical mechanics and its applications* **2006**, *371*, 336-360.
106. Philip, J.; De Vries, D., Moisture Movement in Porous Materials under Temperature Gradients. *Eos, Transactions American Geophysical Union* **1957**, *38*, 222-232.
107. Yiotis, A. G.; Boudouvis, A. G.; Stubos, A. K.; Tsimpanogiannis, I. N.; Yortsos, Y. C., Effect of Liquid Films on the Drying of Porous Media. *Aiche Journal* **2004**, *50*, 2721-2737.
108. Prat, M., On the Influence of Pore Shape, Contact Angle and Film Flows on Drying of Capillary Porous Media. *International Journal of Heat and Mass Transfer* **2007**, *50*, 1455-1468.
109. Wu, R.; Zhao, C.; Tsotsas, E.; Kharaghani, A., Convective Drying in Thin Hydrophobic Porous Media. *Int. J. Heat Mass Tran.* **2017**, *112*, 630-642.
110. Wu, R.; Kharaghani, A.; Tsotsas, E., Two-Phase Flow with Capillary Valve Effect in Porous Media. *Chemical Engineering Science* **2016**, *139*, 241-248.
111. Prat, M., Isothermal Drying on Non-Hygroscopic Capillary-Porous Materials as an Invasion Percolation Process. *International journal of multiphase flow* **1995**, *21*, 875-892.
112. Surasani, V.; Metzger, T.; Tsotsas, E., Influence of Heating Mode on Drying Behavior of Capillary Porous Media: Pore Scale Modeling. *Chemical Engineering Science* **2008**, *63*, 5218-5228.
113. Shokri, N.; Or, D., Drying Patterns of Porous Media Containing Wettability Contrasts. *Journal of colloid and interface science* **2013**, *391*, 135-141.
114. Prat, M., Percolation Model of Drying under Isothermal Conditions in Porous Media. *International Journal of Multiphase Flow* **1993**, *19*, 691-704.

115. Yiotis, A. G.; Tsimpanogiannis, I. N.; Stubos, A. K.; Yortsos, Y. C., Pore-Network Study of the Characteristic Periods in the Drying of Porous Materials. *Journal of colloid and interface science* **2006**, *297*, 738-748.
116. Council, N. R., *Coal Waste Impoundments: Risks, Responses, and Alternatives*; National Academies Press, 2002.
117. Yoon, R.-H.; Gupta, N.; Li, B.; Luttrell, G. H.; Bratton, R. C.; Reyher, J.; Suboleski, S., Hhs Process: A New Approach for Recovering Fine Illinois Basin Coals. In *Proceedings of the International Coal Preparation Conference*, Louisville, KY, USA, 2016; pp 25-27.
118. Gupta, N.; Li, B.; Luttrell, G.; Yoon, R.-H.; Bratton, R., Hydrophobic-Hydrophilic Separation (Hhs) Process for the Recovery and Dewatering of Ultrafine Coal. In *SME Annual Meeting*, Phoenix, AZ, 2016.
119. Wu, H.; Fang, C.; Wu, R.; Qiao, R., Drying of Porous Media by Concurrent Drainage and Evaporation: A Pore Network Modeling Study. *Int. J. Heat Mass Tran.* **2020**, *152*, 118718.
120. Kohout, M.; Collier, A. P.; Štěpánek, F., Mathematical Modelling of Solvent Drying from a Static Particle Bed. *Chemical engineering science* **2006**, *61*, 3674-3685.
121. Lekhal, A.; Girard, K.; Brown, M.; Kiang, S.; Glasser, B. J.; Khinast, J., Impact of Agitated Drying on Crystal Morphology: Kcl–Water System. *Powder technology* **2003**, *132*, 119-130.
122. Huang, K.; Pan, L.; Yoon, R.-H., A Capillary Flow Model for Filtration. *Minerals Engineering* **2018**, *115*, 88-96.
123. Jiang, X.; Zheng, C.; Yan, C.; Liu, D.; Qiu, J.; Li, J., Physical Structure and Combustion Properties of Super Fine Pulverized Coal Particle. *Fuel* **2002**, *81*, 793-797.
124. Sanchez-Lengeling, B.; Aspuru-Guzik, A., Inverse Molecular Design Using Machine Learning: Generative Models for Matter Engineering. *Science* **2018**, *361*, 360-365.
125. Shokri, N.; Sahimi, M.; Or, D., Morphology, Propagation Dynamics and Scaling Characteristics of Drying Fronts in Porous Media. *Geophysical Research Letters* **2012**, *39*.
126. Jackson, G. W.; James, D. F., The Permeability of Fibrous Porous Media. *The Canadian Journal of Chemical Engineering* **1986**, *64*, 364-374.
127. Millington, R., Gas Diffusion in Porous Media. *Science* **1959**, *130*, 100-102.
128. Goncharenko, A. V., Generalizations of the Bruggeman Equation and a Concept of Shape-Distributed Particle Composites. *Physical review E* **2003**, *68*, 041108.
129. Brunton, S. L.; Noack, B. R.; Koumoutsakos, P., Machine Learning for Fluid Mechanics. *Annual Review of Fluid Mechanics* **2020**, *52*, 477-508.
130. Chang, H.; Zhang, D., Machine Learning Subsurface Flow Equations from Data. *Computational Geosciences* **2019**, *23*, 895-910.
131. Wei, H.; Zhao, S.; Rong, Q.; Bao, H., Predicting the Effective Thermal Conductivities of Composite Materials and Porous Media by Machine Learning Methods. *Int. J. Heat Mass Tran.* **2018**, *127*, 908-916.
132. Zhu, Y.; Zabaras, N., Bayesian Deep Convolutional Encoder–Decoder Networks for Surrogate Modeling and Uncertainty Quantification. *J. Comput. Phys.* **2018**, *366*, 415-447.
133. Tripathy, R. K.; Bilionis, I., Deep Uq: Learning Deep Neural Network Surrogate Models for High Dimensional Uncertainty Quantification. *J. Comput. Phys.* **2018**, *375*, 565-588.

134. LeCun, Y.; Bottou, L.; Bengio, Y.; Haffner, P., Gradient-Based Learning Applied to Document Recognition. *Proceedings of the IEEE* **1998**, *86*, 2278-2324.
135. Wu, J.; Yin, X.; Xiao, H., Seeing Permeability from Images: Fast Prediction with Convolutional Neural Networks. *Science Bulletin* **2018**, *63*, 1215-1222.
136. He, K.; Zhang, X.; Ren, S.; Sun, J. In *Identity Mappings in Deep Residual Networks*, European conference on computer vision, Springer: 2016; pp 630-645.
137. Wu, H.; Fang, W.-Z.; Kang, Q.; Tao, W.-Q.; Qiao, R., Predicting Effective Diffusivity of Porous Media from Images by Deep Learning. *arXiv preprint arXiv:1912.05532* **2019**.
138. Iscan, A.; Kok, M., Porosity and Permeability Determinations in Sandstone and Limestone Rocks Using Thin Section Analysis Approach. *Energy Sources, Part A: Recovery, Utilization, and Environmental Effects* **2009**, *31*, 568-575.
139. Aster, R. C.; Borchers, B.; Thurber, C. H., *Parameter Estimation and Inverse Problems*; Elsevier, 2018.
140. Beskos, A.; Jasra, A.; Muzaffer, E. A.; Stuart, A. M., Sequential Monte Carlo Methods for Bayesian Elliptic Inverse Problems. *Statistics and Computing* **2015**, *25*, 727-737.
141. Ballio, F.; Guadagnini, A., Convergence Assessment of Numerical Monte Carlo Simulations in Groundwater Hydrology. *Water Resources Research* **2004**, *40*, 1-5.
142. Reddy, K.; Somasundharam, S. In *An Inverse Method for Simultaneous Estimation of Thermal Properties of Orthotropic Materials Using Gaussian Process Regression*, Journal of Physics: Conference Series, IOP Publishing: 2016; p 032090.
143. Peurifoy, J.; Shen, Y.; Jing, L.; Yang, Y.; Cano-Renteria, F.; DeLacy, B. G.; Joannopoulos, J. D.; Tegmark, M.; Soljačić, M., Nanophotonic Particle Simulation and Inverse Design Using Artificial Neural Networks. *Science advances* **2018**, *4*, eaar4206.
144. Mo, S.; Zhu, Y.; Zabaras, N.; Shi, X.; Wu, J., Deep Convolutional Encoder-Decoder Networks for Uncertainty Quantification of Dynamic Multiphase Flow in Heterogeneous Media. *Water Resources Research* **2019**, *55*, 703-728.
145. Kamrava, S.; Tahmasebi, P.; Sahimi, M., Linking Morphology of Porous Media to Their Macroscopic Permeability by Deep Learning. *Transport. Porous. Med.* **2019**, 1-22.
146. Wu, H.; Fang, W.-Z.; Kang, Q.; Tao, W.-Q.; Qiao, R., Predicting Effective Diffusivity of Porous Media from Images by Deep Learning. *Sci. Rep.* **2019**, *9*, 1-12.
147. Kang, H. H.; Kaya, M.; Hajimirza, S., A Data Driven Artificial Neural Network Model for Predicting Radiative Properties of Metallic Packed Beds. *Journal of Quantitative Spectroscopy and Radiative Transfer* **2019**, *226*, 66-72.
148. Wu, Z.; Kan, S. J.; Lewis, R. D.; Wittmann, B. J.; Arnold, F. H., Machine Learning-Assisted Directed Protein Evolution with Combinatorial Libraries. *Proc. Natl. Acad. Sci.* **2019**, *116*, 8852-8858.
149. Manohar, K.; Brunton, B. W.; Kutz, J. N.; Brunton, S. L., Data-Driven Sparse Sensor Placement for Reconstruction: Demonstrating the Benefits of Exploiting Known Patterns. *IEEE Control Systems Magazine* **2018**, *38*, 63-86.
150. Erichson, N. B.; Mathelin, L.; Yao, Z.; Brunton, S. L.; Mahoney, M. W.; Kutz, J. N., Shallow Learning for Fluid Flow Reconstruction with Limited Sensors and Limited Data. *arXiv preprint arXiv:1902.07358* **2019**.
151. He, Q.; Brajas-Solano, D.; Tartakovsky, G.; Tartakovsky, A. M., Physics-Informed Neural Networks

for Multiphysics Data Assimilation with Application to Subsurface Transport. *arXiv preprint arXiv:1912.02968* **2019**.

152. Raissi, M.; Perdikaris, P.; Karniadakis, G. E., Physics-Informed Neural Networks: A Deep Learning Framework for Solving Forward and Inverse Problems Involving Nonlinear Partial Differential Equations. *J. Comput. Phys.* **2019**, *378*, 686-707.
153. Zhang, X.; Xiao, L.; Shan, X.; Guo, L., Lattice Boltzmann Simulation of Shale Gas Transport in Organic Nano-Pores. *Sci. Rep.* **2014**, *4*, 4843.
154. Curtis, M. E.; Sondergeld, C. H.; Ambrose, R. J.; Rai, C. S., Microstructural Investigation of Gas Shales in Two and Three Dimensions Using Nanometer-Scale Resolution Imaging. *Am. Assoc. Pet. Geol. Bull.* **2012**, *96*, 665-677.
155. Chalmers, G. R.; Bustin, R. M.; Power, I. M., Characterization of Gas Shale Pore Systems by Porosimetry, Pycnometry, Surface Area, and Field Emission Scanning Electron Microscopy/Transmission Electron Microscopy Image Analyses: Examples from the Barnett, Woodford, Haynesville, Marcellus, and Doig Units. *Am. Assoc. Pet. Geol. Bull.* **2012**, *96*, 1099-1119.
156. Soeder, D. J., Porosity and Permeability of Eastern Devonian Gas Shale. *Spe. Formation. Eval.* **1988**, *3*, 116-124.
157. Javadpour, F.; Fisher, D.; Unsworth, M., Nanoscale Gas Flow in Shale Gas Sediments. *J. Can. Petrol. Technol.* **2007**, *46*, 55-61.
158. Chong, K. K.; Grieser, W. V.; Passman, A.; Tamayo, H. C.; Modeland, N.; Burke, B. E. In *A Completions Guide Book to Shale-Play Development: A Review of Successful Approaches toward Shale-Play Stimulation in the Last Two Decades*, Canadian Unconventional Resources and International Petroleum Conference, Calgary, Alberta, Canada, 19-21 October; Society of Petroleum Engineers: Calgary, Alberta, Canada, 2010.
159. Civan, F., Effective Correlation of Apparent Gas Permeability in Tight Porous Media. *Transport. Porous. Med.* **2010**, *82*, 375-384.
160. Zhang, P.; Hu, L.; Meegoda, J. N.; Gao, S., Micro/Nano-Pore Network Analysis of Gas Flow in Shale Matrix. *Sci. Rep.* **2015**, *5*.
161. Vanson, J.-M.; Coudert, F.-X.; Rotenberg, B.; Levesque, M.; Tardivat, C.; Klotz, M.; Boutin, A., Unexpected Coupling between Flow and Adsorption in Porous Media. *Soft matter* **2015**, *11*, 6125-6133.
162. Zhang, J.; Scherer, G. W., Permeability of Shale by the Beam-Bending Method. *Int. J. Rock Mech. Min. Sci.* **2012**, *53*, 179-191.
163. Fathi, E.; Akkutlu, I. Y., Mass Transport of Adsorbed-Phase in Stochastic Porous Medium with Fluctuating Porosity Field and Nonlinear Gas Adsorption Kinetics. *Transport. Porous. Med.* **2012**, *91*, 5-33.
164. Bhatia, S. K.; Jepps, O.; Nicholson, D., Tractable Molecular Theory of Transport of Lennard-Jones Fluids in Nanopores. *J. Chem. Phys.* **2004**, *120*, 4472-4485.
165. Plimpton, S., Fast Parallel Algorithms for Short-Range Molecular Dynamics. *J. Comput. Phys.* **1995**, *117*, 1-19.
166. Whitaker, S., *Fundamental Principles of Heat Transfer*; Elsevier, 2013.
167. Darken, L. S., Diffusion, Mobility and Their Interrelation through Free Energy in Binary Metallic

Systems. *Trans. Aime* **1948**, *175*, 184-201.
168. Maginn, E. J.; Bell, A. T.; Theodorou, D. N., Transport Diffusivity of Methane in Silicalite from Equilibrium and Nonequilibrium Simulations. *J. Phys. Chem.* **1993**, *97*, 4173-4181.
169. Kleinhammes, A.; Mao, S.-H.; Yang, X.-J.; Tang, X.-P.; Shimoda, H.; Lu, J.; Zhou, O.; Wu, Y., Gas Adsorption in Single-Walled Carbon Nanotubes Studied by Nmr. *Phys. Rev. B.* **2003**, *68*, 075418.
170. Bulba, K. A.; Krouskop, P. E., Compositional Variety Complicates Processing Plans for Us Shale Gas. *Oil Gas J.* **2009**, *107*, 50-55.
171. Wang, J.; Chen, L.; Kang, Q.; Rahman, S. S., The Lattice Boltzmann Method for Isothermal Micro-Gaseous Flow and Its Application in Shale Gas Flow: A Review. *Int. J. Heat Mass Tran.* **2016**, *95*, 94-108.
172. Eijkel, J. C.; Van Den Berg, A., Nanofluidics: What Is It and What Can We Expect from It? *Microfluid. Nanofluid.* **2005**, *1*, 249-267.
173. Vo, T. Q.; Barisik, M.; Kim, B., Atomic Density Effects on Temperature Characteristics and Thermal Transport at Grain Boundaries through a Proper Bin Size Selection. *J. Chem. Phys.* **2016**, *144*, 194707.
174. Vo, T. Q.; Park, B.; Park, C.; Kim, B., Nano-Scale Liquid Film Sheared between Strong Wetting Surfaces: Effects of Interface Region on the Flow. *J Mech. Sci. Technol.* **2015**, *29*, 1681.
175. Bakli, C.; Chakraborty, S., Effect of Presence of Salt on the Dynamics of Water in Uncharged Nanochannels. *J. Chem. Phys.* **2013**, *138*, 054504.
176. Chen, L.; Zhang, L.; Kang, Q.; Viswanathan, H. S.; Yao, J.; Tao, W., Nanoscale Simulation of Shale Transport Properties Using the Lattice Boltzmann Method: Permeability and Diffusivity. *Sci. Rep.* **2015**, *5*, 8089
177. Lee, S.; Padmanabhan, L.; Al-Sunaidi, H., Simulation of Linear Displacement Experiments on Massively Parallel Computers. *SPE J.* **1996**, *1*, 327-340.
178. Chempath, S.; Krishna, R.; Snurr, R. Q., Nonequilibrium Molecular Dynamics Simulations of Diffusion of Binary Mixtures Containing Short N-Alkanes in Faujasite. *The Journal of Physical Chemistry B* **2004**, *108*, 13481-13491.
179. Martin, M. G.; Siepmann, J. I., Transferable Potentials for Phase Equilibria. 1. United-Atom Description of N-Alkanes. *The Journal of Physical Chemistry B* **1998**, *102*, 2569-2577.
180. Ambrose, R. J.; Hartman, R. C.; Diaz-Campos, M.; Akkutlu, I. Y.; Sondergeld, C. H., Shale Gas-in-Place Calculations Part I: New Pore-Scale Considerations. *SPE J.* **2012**, *17*, 219-229.
181. Talbot, J., Analysis of Adsorption Selectivity in a One-Dimensional Model System. *Aiche. J.* **1997**, *43*, 2471-2478.
182. Bakaev, V.; Steele, W., Hard Rods on a Line as a Model for Adsorption of Gas Mixtures on Homogeneous and Heterogeneous Surfaces. *Langmuir* **1997**, *13*, 1054-1063.
183. Du, Z.; Manos, G.; Vlugt, T. J.; Smit, B., Molecular Simulation of Adsorption of Short Linear Alkanes and Their Mixtures in Silicalite. *Aiche. J.* **1998**, *44*, 1756-1764.
184. Skoulidas, A. I.; Sholl, D. S.; Krishna, R., Correlation Effects in Diffusion of Ch4/Cf4 Mixtures in Mfi Zeolite. A Study Linking Md Simulations with the Maxwell− Stefan Formulation. *Langmuir* **2003**, *19*, 7977-7988.
185. Collell, J.; Galliero, G.; Vermorel, R.; Ungerer, P.; Yiannourakou, M.; Montel, F.; Pujol, M., Transport of Multicomponent Hydrocarbon Mixtures in Shale Organic Matter by Molecular Simulations. *The*

Journal of Physical Chemistry C **2015**, *119*, 22587-22595.
186. Sharma, G.; Verma, R.; Pathare, P., Thin-Layer Infrared Radiation Drying of Onion Slices. *Journal of Food Engineering* **2005**, *67*, 361-366.
187. Aidun, C. K.; Clausen, J. R., Lattice-Boltzmann Method for Complex Flows. *Annual review of fluid mechanics* **2010**, *42*, 439-472.
188. Wilkinson, D.; Willemsen, J. F., Invasion Percolation: A New Form of Percolation Theory. *Journal of Physics A: Mathematical and General* **1983**, *16*, 3365.
189. Lenormand, R.; Zarcone, C.; Sarr, A., Mechanisms of the Displacement of One Fluid by Another in a Network of Capillary Ducts. *J. Fluid Mech.* **1983**, *135*, 337-353.
190. Yoon, R.-H. Methods of Enhancing Fine Particle Dewatering. Patent No. 6,855,260, 2005.
191. Xiumin, J.; Chuguang, Z.; Che, Y.; Dechang, L.; Jianrong, Q.; Jubin, L., Physical Structure and Combustion Properties of Super Fine Pulverized Coal Particle. *Fuel* **2002**, *81*, 793-797.
192. Joekar-Niasar, V.; Hassanizadeh, S. M.; Dahle, H., Non-Equilibrium Effects in Capillarity and Interfacial Area in Two-Phase Flow: Dynamic Pore-Network Modelling. *J. Fluid Mech.* **2010**, *655*, 38-71.
193. Joekar-Niasar, V.; Hassanizadeh, S., Analysis of Fundamentals of Two-Phase Flow in Porous Media Using Dynamic Pore-Network Models: A Review. *Critical reviews in environmental science and technology* **2012**, *42*, 1895-1976.
194. Gielen, T.; Hassanizadeh, S.; Leijnse, A.; Nordhaug, H., Dynamic Effects in Multiphase Flow: A Pore-Scale Network Approach. In *Upscaling Multiphase Flow in Porous Media*, Springer: 2005; pp 217-236.
195. Thompson, K. E., Pore‐Scale Modeling of Fluid Transport in Disordered Fibrous Materials. *Aiche. J.* **2002**, *48*, 1369-1389.
196. Khayrat, K.; Jenny, P., A Multi-Scale Network Method for Two-Phase Flow in Porous Media. *J. Comput. Phys.* **2017**, *342*, 194-210.
197. Metzger, T.; Tsotsas, E., Viscous Stabilization of Drying Front: Three-Dimensional Pore Network Simulations. *Chemical Engineering Research and Design* **2008**, *86*, 739-744.
198. Hussain, A.; Seidel-Morgenstern, A.; Tsotsas, E., Heat and Mass Transfer in Tubular Ceramic Membranes for Membrane Reactors. *Int. J. Heat Mass Tran.* **2006**, *49*, 2239-2253.
199. Brown, G. P.; DiNardo, A.; Cheng, G. K.; Sherwood, T. K., The Flow of Gases in Pipes at Low Pressures. *Journal of Applied Physics* **1946**, *17*, 802-813.
200. Buddenberg, J.; Wilke, C., Calculation of Gas Mixture Viscosities. *Industrial & Engineering Chemistry* **1949**, *41*, 1345-1347.
201. Young, L. C.; Finlayson, B. A., Mathematical Models of the Monolith Catalytic Converter: Part Ii. Application to Automobile Exhaust. *Aiche. J.* **1976**, *22*, 343-353.
202. Davis, T. A., *Direct Methods for Sparse Linear Systems*; Siam, 2006; Vol. 2.
203. Rothe, E. W.; Bernstein, R. B., Total Collision Cross Sections for the Interaction of Atomic Beams of Alkali Metals with Gases. *J. Chem. Phys.* **1959**, *31*, 1619-1627.
204. Liu, H.; Valocchi, A. J.; Kang, Q.; Werth, C., Pore-Scale Simulations of Gas Displacing Liquid in a Homogeneous Pore Network Using the Lattice Boltzmann Method. *Transport. Porous. Med.* **2013**, *99*, 555-580.

205. Homsy, G. M., Viscous Fingering in Porous Media. *Annual review of fluid mechanics* **1987**, *19*, 271-311.
206. Yang, Z.; Yabansu, Y. C.; Al-Bahrani, R.; Liao, W.-k.; Choudhary, A. N.; Kalidindi, S. R.; Agrawal, A., Deep Learning Approaches for Mining Structure-Property Linkages in High Contrast Composites from Simulation Datasets. *Computational Materials Science* **2018**, *151*, 278-287.
207. Cecen, A.; Dai, H.; Yabansu, Y. C.; Kalidindi, S. R.; Song, L., Material Structure-Property Linkages Using Three-Dimensional Convolutional Neural Networks. *Acta Materialia* **2018**, *146*, 76-84.
208. He, K.; Zhang, X.; Ren, S.; Sun, J. In *Deep Residual Learning for Image Recognition*, Proceedings of the IEEE conference on computer vision and pattern recognition, 2016; pp 770-778.
209. Krizhevsky, A.; Sutskever, I.; Hinton, G. E. In *Imagenet Classification with Deep Convolutional Neural Networks*, Advances in neural information processing systems, 2012; pp 1097-1105.
210. Cireşan, D.; Meier, U.; Schmidhuber, J., Multi-Column Deep Neural Networks for Image Classification. *arXiv preprint arXiv:1202.2745* **2012**.
211. Cang, R.; Li, H.; Yao, H.; Jiao, Y.; Ren, Y., Improving Direct Physical Properties Prediction of Heterogeneous Materials from Imaging Data Via Convolutional Neural Network and a Morphology-Aware Generative Model. *Computational Materials Science* **2018**, *150*, 212-221.
212. Srisutthiyakorn, N., Deep-Learning Methods for Predicting Permeability from 2d/3d Binary-Segmented Images. *SEG technical program expanded abstracts 2016* **2016**, 3042-3046.
213. Wang, M.; Wang, J.; Pan, N.; Chen, S., Mesoscopic Predictions of the Effective Thermal Conductivity for Microscale Random Porous Media. *Physical Review E* **2007**, *75*, 036702.
214. Fang, W.-Z.; Gou, J.-J.; Chen, L.; Tao, W.-Q., A Multi-Block Lattice Boltzmann Method for the Thermal Contact Resistance at the Interface of Two Solids. *Applied Thermal Engineering* **2018**, *138*, 122-132.
215. LeCun, Y.; Bengio, Y.; Hinton, G., Deep Learning. *nature* **2015**, *521*, 436.
216. LeCun, Y.; Bengio, Y., Convolutional Networks for Images, Speech, and Time Series. *The handbook of brain theory and neural networks* **1995**, *3361*, 1995.
217. Dollár, P.; Appel, R.; Belongie, S.; Perona, P., Fast Feature Pyramids for Object Detection. *IEEE Transactions on Pattern Analysis and Machine Intelligence* **2014**, *36*, 1532-1545.
218. Ramachandran, P.; Zoph, B.; Le, Q. V., Searching for Activation Functions. *arXiv preprint arXiv:1710.05941* **2017**.
219. The Scientist and Engineer's Guide to Digital Signal Processing. New Scientist Ltd: 2001; Vol. 171, p 47.
220. He, L.; Chao, Y.; Suzuki, K.; Wu, K., Fast Connected-Component Labeling. *Pattern Recognition* **2009**, *42*, 1977-1987.
221. Fisher, R.; Perkins, S.; Walker, A.; Wolfart, E. In *Connected Component Labeling*, IEE International Conference on Intelligent Systems, 2003; pp 300-350.
222. Abadi, M.; Barham, P.; Chen, J.; Chen, Z.; Davis, A.; Dean, J.; Devin, M.; Ghemawat, S.; Irving, G.; Isard, M. In *Tensorflow: A System for Large-Scale Machine Learning*, 12th Symposium on Operating Systems Design and Implementation (16), 2016; pp 265-283.
223. Kingma, D. P.; Ba, J., Adam: A Method for Stochastic Optimization. *arXiv preprint arXiv:1412.6980* **2014**.

224. Lange, K. J.; Sui, P.-C.; Djilali, N., Pore Scale Simulation of Transport and Electrochemical Reactions in Reconstructed Pemfc Catalyst Layers. *Journal of The Electrochemical Society* **2010**, *157*, B1434-B1442.
225. Molchanov, P.; Gupta, S.; Kim, K.; Kautz, J. In *Hand Gesture Recognition with 3d Convolutional Neural Networks*, Proceedings of the IEEE conference on computer vision and pattern recognition workshops, 2015; pp 1-7.
226. Ji, S.; Xu, W.; Yang, M.; Yu, K., 3d Convolutional Neural Networks for Human Action Recognition. *IEEE transactions on pattern analysis and machine intelligence* **2012**, *35*, 221-231.
227. Dou, Q.; Chen, H.; Yu, L.; Zhao, L.; Qin, J.; Wang, D.; Mok, V. C.; Shi, L.; Heng, P.-A., Automatic Detection of Cerebral Microbleeds from Mr Images Via 3d Convolutional Neural Networks. *IEEE transactions on medical imaging* **2016**, *35*, 1182-1195.
228. King Jr, H. E.; Eberle, A. P.; Walters, C. C.; Kliewer, C. E.; Ertas, D.; Huynh, C., Pore Architecture and Connectivity in Gas Shale. *Energy & Fuels* **2015**, *29*, 1375-1390.
229. Wildenschild, D.; Sheppard, A. P., X-Ray Imaging and Analysis Techniques for Quantifying Pore-Scale Structure and Processes in Subsurface Porous Medium Systems. *Advances in Water Resources* **2013**, *51*, 217-246.
230. Sok, R. M.; Knackstedt, M. A.; Varslot, T.; Ghous, A.; Latham, S.; Sheppard, A. P., Pore Scale Characterization of Carbonates at Multiple Scales: Integration of Micro-Ct, Bsem, and Fibsem. *Petrophysics* **2010**, *51*.
231. Wu, X.; Kozlowski, T., Inverse Uncertainty Quantification of Reactor Simulation with Polynomial Chaos Surrogate Model. *Transactions of American Nuclear Society. American Nuclear Society, New Orleans, LA, USA* **2016**.
232. Szegedy, C.; Vanhoucke, V.; Ioffe, S.; Shlens, J.; Wojna, Z. In *Rethinking the Inception Architecture for Computer Vision*, Proceedings of the IEEE Conference on Computer Vision and Pattern Recognition, 2016; pp 2818-2826.
233. Young, T.; Hazarika, D.; Poria, S.; Cambria, E., Recent Trends in Deep Learning Based Natural Language Processing. *IEEE Computational Intelligence Magazine* **2018**, *13*, 55-75.
234. Collobert, R.; Weston, J. In *A Unified Architecture for Natural Language Processing: Deep Neural Networks with Multitask Learning*, Proceedings of the 25th International Conference on Machine Learning, ACM: 2008; pp 160-167.
235. Jin, L.; Lu, H.; Wen, G., Fast Uncertainty Quantification of Reservoir Simulation with Variational U-Net. *arXiv preprint arXiv:1907.00718* **2019**.
236. Gu, J.; Wang, Z.; Kuen, J.; Ma, L.; Shahroudy, A.; Shuai, B.; Liu, T.; Wang, X.; Wang, G.; Cai, J., Recent Advances in Convolutional Neural Networks. *Pattern Recognition* **2018**, *77*, 354-377.
237. Goodfellow, I.; Bengio, Y.; Courville, A., *Deep Learning*; MIT Press, 2016.
238. Badrinarayanan, V.; Kendall, A.; Cipolla, R., Segnet: A Deep Convolutional Encoder-Decoder Architecture for Image Segmentation. *IEEE Transactions on Pattern Analysis and Machine Intelligence* **2017**, *39*, 2481-2495.
239. Doersch, C., Tutorial on Variational Autoencoders. *arXiv preprint arXiv:1606.05908* **2016**.
240. Kendall, A.; Badrinarayanan, V.; Cipolla, R., Bayesian Segnet: Model Uncertainty in Deep Convolutional Encoder-Decoder Architectures for Scene Understanding. *arXiv preprint*

arXiv:1511.02680 **2015**.
241. Long, J.; Shelhamer, E.; Darrell, T. In *Fully Convolutional Networks for Semantic Segmentation*, Proceedings of the IEEE Conference on Computer Vision and Pattern Recognition, 2015; pp 3431-3440.
242. Dumoulin, V.; Visin, F., A Guide to Convolution Arithmetic for Deep Learning. *arXiv preprint arXiv:1603.07285* **2016**.
243. Ronneberger, O.; Fischer, P.; Brox, T. In *U-Net: Convolutional Networks for Biomedical Image Segmentation*, International Conference on Medical image computing and computer-assisted intervention, Springer: 2015; pp 234-241.
244. Esser, P.; Sutter, E.; Ommer, B. In *A Variational U-Net for Conditional Appearance and Shape Generation*, Proceedings of the IEEE Conference on Computer Vision and Pattern Recognition, 2018; pp 8857-8866.
245. Hoeltgen, L.; Setzer, S.; Weickert, J. In *An Optimal Control Approach to Find Sparse Data for Laplace Interpolation*, International Workshop on Energy Minimization Methods in Computer Vision and Pattern Recognition, Springer: 2013; pp 151-164.
246. Rong, Q.; Wei, H.; Huang, X.; Bao, H., Predicting the Effective Thermal Conductivity of Composites from Cross Sections Images Using Deep Learning Methods. *Composites Science and Technology* **2019**, *184*, 107861.
247. Wang, C.; MacGillivray, T.; Macnaught, G.; Yang, G.; Newby, D., A Two-Stage 3d Unet Framework for Multi-Class Segmentation on Full Resolution Image. *arXiv preprint arXiv:1804.04341* **2018**.
248. Bertinetto, L.; Henriques, J. F.; Torr, P. H.; Vedaldi, A., Meta-Learning with Differentiable Closed-Form Solvers. *arXiv preprint arXiv:1805.08136* **2018**.
249. Raissi, M.; Perdikaris, P.; Karniadakis, G. E., Physics Informed Deep Learning (Part I): Data-Driven Solutions of Nonlinear Partial Differential Equations. *arXiv preprint arXiv:1711.10561* **2017**.
250. Kalchbrenner, N.; Grefenstette, E.; Blunsom, P., A Convolutional Neural Network for Modelling Sentences. *arXiv preprint arXiv:1404.2188* **2014**.
251. Tolias, G.; Sicre, R.; Jégou, H., Particular Object Retrieval with Integral Max-Pooling of Cnn Activations. *arXiv preprint arXiv:1511.05879* **2015**.
252. Zeiler, M. D.; Fergus, R., Stochastic Pooling for Regularization of Deep Convolutional Neural Networks. *arXiv preprint arXiv:1301.3557* **2013**.